1-1-2020

Resonant Ultrasound Spectroscopy Studies Of Poroelasticity In Porous Ceramics And Elasticity Of Thermoelectric Snse

Ashoka Karunarathne

RESONANT ULTRASOUND SPECTROSCOPY STUDIES OF POROELASTICITY IN POROUS CERAMICS AND ELASTICITY OF THERMOELECTRIC SnSe

A Dissertation Submitted in Partial Fulfilment of the Requirements
for the Degree of Doctor of Philosophy
in the Department of Physics and Astronomy
The University of Mississippi
University, MS 38677

by
Ashoka Karunarathne
May 2020

ABSTRACT

This dissertation primarily focuses on use of resonant ultrasound spectroscopic (RUS) measurements to investigate temperature- and pressure-dependent elastic properties of select materials: porous ceramics, which are used in a wide range of material applications, and thermoelectric tin selenide (SnSe), which is widely studied as an efficient thermoelectric material. RUS experiments were conducted on: ceramics used in LG fuel cells, alumina, zircona and titania, to explore their elastic behavior under the variation of hydrostatic pressure over the low- and high-pressure regimes (0.02 – 800 psi). All the porous ceramics exhibited a reversible material softening mechanism with increasing hydrostatic pressure. The comparison of material stiffening with increasing pressure observed from fully dense ceramics validates the poroelastic behavior of porous ceramics described by Biot's theory of poroelasticity. The influence of saturated gas type and their physical properties on the above elasticity variation with hydrostatic pressure was analyzed qualitatively as well as quantitatively by using the helium, nitrogen, and argon gas saturation. The observed porous material stiffness with increasing temperature was explained by the partial sintering and microcrack healing mechanisms. Single crystalline SnSe has an orthorhombic *Pnma* phase that undergoes a displacive phase transition transforming into a *Cmcm* phase at ~810 K. Temperature dependence of elastic constants (C_{ij}) of SnSe were measured at elevated temperatures in the range of 295 – 773 K. The measured elastic constants were then used to explain the elastic anisotropic behavior, structural change, and the thermal transportation mechanisms of SnSe at higher temperatures. The occurrence of the phase transition at 803 ± 10 K

was analyzed by the temperature-dependent normal mode frequency trends. The validation of the measured elastic constants and derived elastic properties are discussed using the previously reported theoretical and experimental studies.

ACKNOWLEDGEMENTS

I would like to express my heartiest gratitude to all the people who were behind the success of this dissertation work. The first appreciation goes to my supervisor, Dr. J. R. Gladden, for all of his guidance and support throughout the completion of this dissertation, and for being an excellent mentor, being very supportive, sharing his knowledge, and for guiding me to move forward as a professional researcher. I thank my fellow lab mates Dr. Sumudu Tennakoon and Dr. Gautam Priydarshan for their guidance, support, and encouragement at the initial stage of my research with the material science group at NCPA. I would also thank the members of my dissertation committee: Dr. Joel Mobley, Dr. Kevin Beach, Dr. Likun Zhang, and Dr. Nathan Murray for their generous advice and time commitment in the dissertation procedure. I gratefully mention the support and advice given by the collaborators: Dr. Sriparna Bhattacharya, Dr. Jason Griggs, and Dr. Amit Pandey, who closely worked with me to achieve the success of collaborative research projects. I thank all the faculty and staff members of both the Department of Physics & Astronomy and the National Center for Physical Acoustic for their all supports.

I am very grateful to my beloved parents, T. G. Karunarathne and Malani Abeywardhana for their effort in raising me as a good human being to the society, and for their enormous care and support in my education. A special appreciation goes to my beloved wife Prabha Yapa for being supportive and motivational throughout last five years of my graduate life. Lastly, I thank all of my relatives, friends, high school teachers, and university lecturers who played important roles for the success of this dissertation work and my doctoral degree. Thank you all!!

TABLE OF CONTENTS

List of Tables

List of Figures

CHAPTER 1

INTRODUCTION

Innovation of new materials is one of the most important roles in the development of science and technology. In early stages, engineering inventions had been limited by access to only naturally occurring materials, which could not be used for wide variety of engineering applications due to their inflexible material properties. Therefore, researchers put their energies into developing technologies to synthesize new substances with controlled material properties in order to enhance the utility of the material. Currently, nanotechnology and 3D printing techniques are the leading technologies in the material fabrication field [1–3]. Along with the discovery of new materials, the development of material characterization techniques is essential to understand and study material properties and their behavior in various chemical, thermal, and mechanical environments.

Elasticity is considered as a fundamental mechanical property of solid materials. It measures the material deformation to applied stress. Strain (ε_{ij}) and stress (σ_{ij}) are the main physical measurements that determine the elasticity of a material. In a three-dimensional framework, those parameters are expressed as tensors and Hooke's law is used to link them with the parameter called elastic stiffness tensor (c_{ijkl}) as $\sigma_{ij} = c_{ijkl}\varepsilon_{kl}$ [4–6]. The elements of the elastic stiffness tensor are known as elastic constants, and they are a measure of the second derivative of the interatomic potential energy with respect to strain [7]. Elastic constants are a sensitive probe of the interatomic bonds and their dynamics in response to the variation of physical conditions such as temperature and pressure. Therefore, measurements of elastic constants can be

used to study the lattice dynamics and phase transformations within the crystal symmetry [8]. Elastic constants of a given material can be used to calculate its elastic moduli: Young's modulus, bulk modulus, shear modulus, Poisson ratio, and wave velocities [9,10]. Since lattice vibrations (phonons) are the main source of heat propagation through the solid materials, elasticity measurements can be used to determine many thermodynamic properties such as Debye temperature, heat capacity, lattice thermal conductivity, and phonon mean free path [11,12].

Acoustical nondestructive techniques are widely used for measuring elastic constants because of their key advantages over the conventional measuring techniques such as static loading, inelastic neutron scattering, and X-ray scattering under constants stress. The pulse-echo technique, which measures the flight time of an ultrasound pulse through the material to calculate the wave velocities, is one of the simplest methods of measuring elastic constants of solids [13,14]. This technique is commonly used to make room temperature elasticity measurements of highly symmetric crystal structures for which fewer elastic constants are required. However, use of the pulse-echo technique with low symmetric crystals is challenging as it requires multiple velocity measurements in each crystallographic direction. Also, this technique is difficult at elevated temperatures because of the working temperature limitations of the transducer elements and coupling agents.

A resonance method called Resonant Ultrasound Spectroscopy (RUS) was introduced in the 1990s as the most precise and efficient experimental technique for measuring elastic constants [15–18]. In RUS, a resonance spectrum of the test specimen is measured to compute the elastic tensor. An acoustic transducer is used to excite the specimen in a swept-frequency continuous wave (CW) mode over a selected frequency range. At the resonance, where the drive frequency matches the natural vibrational frequency of the sample, the sample surface shows a

maximum displacement which is read by a second transducer to obtain the resonance spectrum. Natural vibrational frequencies of a solid continuum are mainly determined by its geometry, mass density, and the elastic constants. The measured frequencies are compared to frequencies computed using the Rayleigh Ritz method, and elastic moduli are optimized using non-linear regression methods [19]. The enhancement of the computational power of modern computers facilitates this technique to compute the elastic tensors of low symmetric crystals with different continuum shapes such as spheres, rectangular parallelepiped, and cylinders, from a single measurement of the resonance spectrum [20]. Use of millimeter sized test specimens and requiring point contact coupling with transducers without any coupling medium provide much flexibility in constructing the RUS setup. Compared to other mechanical testing methods, RUS has gained interest among the experimental material science fields due to its precision, ability to resolve all elastic constants in a single measurement, and ability to take measurements over a range of temperatures and hydrostatic pressures [21].

This dissertation primarily focuses on use of resonant ultrasound spectroscopic measurements to investigate the temperature and pressure effects on the elastic properties of select materials: porous ceramics, which are used in wide range of material applications, and thermoelectric tin selenide (SnSe), which is widely studied as an efficient thermoelectric material.

1.1 Elasticity of Porous Materials

In recent years, use of porous materials in engineering applications has significantly increased due to enhanced mechanical, structural and thermal properties over typical fully dense materials. Both naturally occurring and engineered porous materials consist of two phases: solid skeleton and pores saturated with fluid (Figure 1.1). The porosity, skeleton-pore structure

arrangement, and the properties of both solid and fluid are the key factors that characterize the overall mechanical, thermal, and chemical properties of porous solids. Geological rocks and biological tissues are some examples of naturally occurring porous materials. Use of natural porous substances for material applications is limited due to their unreliable material properties and instability at different physical conditions such as temperature and pressure. Therefore, engineering and material science communities have shown their interest in the investigation and use of suitable engineered porous materials with tunable material characteristics [22–24]. As a result, porous ceramics have been introduced as an ideal candidate in a wide range of material applications in the fields of aerospace, automotive, biomedical, energy storage devices, filters, and many others.

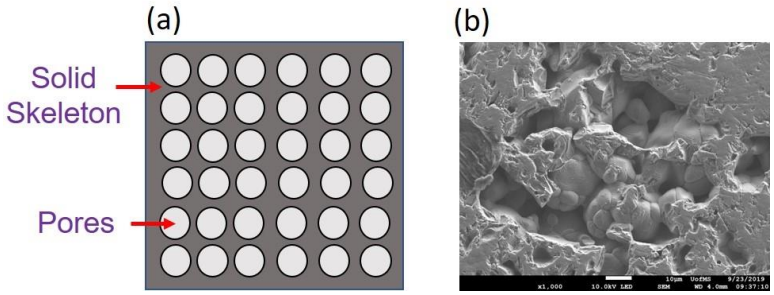

Figure 1.1. (a) Schematic diagram of a porous structure and (b) SEM image of a porous ceramic material.

The use of porous materials is most common in aerospace applications, because of their thermal insulation, acoustic damping, and lightweight structural properties. Porous ceramics exhibit good thermal insulation quality with low thermal conductivity and high stability at extreme temperature conditions [25,26]. The porosity-dependent thermal conductivity provides the freedom to control the insulation quality. This thermal insulation property and the improved oxidation resistance of porous ceramics are used to design combustion engines and many other structural components of aircrafts, which are operated at high temperatures [27,28]. Acoustic

damping, the dissipation of acoustic energy, is another material property of porous solids [29]. In porous materials, the propagation of acoustic waves is influenced by both solid and fluid phases. As the vibrations propagate through the porous materials, the vibrational energy transfers from the solid medium to fluid medium, which is known as the acoustic radiation. When the vibrations in the fluid medium meet the solid medium, only a fraction of the energy is transmitted to the solid, leaving most of the energy trapped in the fluid. The trapped energy in the fluid medium vibrates the fluid phases creating local resonators inside the porous material; eventually the vibrational energy dies due to the viscothermal energy dissipation. This damping property is widely used in noise and vibration reduction applications. Aircraft designers conduct research on use of porous ceramics in building their structures to suppress the unwanted noise and vibrations [30]. Currently, researchers have shown their attention to fabricate porous materials which can be used as acoustic metamaterials for the noise reduction applications [31,32].

The fluid dynamic properties through the porous materials are used in filtration applications, gas sensors and gas storage devices [33–35]. These applications are widely studied and used in the fields of hydrogeology and petroleum engineering. Apart from that, in most of solid oxide fuel cells, porous ceramics are used as anode/cathode and interconnecting materials [36,37]. These solid oxide fuel cells operate at high temperatures and different chemical reaction environments. Therefore, the materials used in fuel cells should fulfill the thermal, mechanical, and chemical stability at extreme physical conditions.

Since the material applications highlighted above are operated in various chemical, temperature, and pressure environments, study of the mechanical behavior of porous materials to the applied external physical conditions is important in selection of the most suitable material to gain the maximum use of the materials. Elasticity provides a broad description about the

mechanical behavior of the solid materials. Unlike fully dense solids, elasticity of porous materials is mainly determined by the solid structure as well as the pore structure and their saturation. In early 1950s, M. A. Biot, introduced the basis and formulations of the theory of poroelasticity, which describes the effects of pore saturated fluid and skeleton arrangement on the elasticity of porous materials [38–41]. According to Biot's poroelasticity theory, the structure of the generalized Hooke's law has been changed in the presence of the fluid phase. This theory suggests a modification of stress and strain tensors with additional parameters that depend on the porosity and the hydrostatic pressure. This modification extends the form of the usual elastic stiffness tensor, C_{ij}, from 6×6 to 7×7. The new tensor elements, poroelastic constants, are used to determine the effective elastic moduli and hence to describe the elasticity of porous materials [42,43]. Biot's theory implies that the elasticity of the porous material primarily depends on the porosity and the pressure of the pore-saturated fluid.

Based on the poroelastic theory, both theoretical and experimental researches have been carried out to study the elasticity of porous materials under different material, physical, and structural conditions. Most of the theoretical work has focused on the effects of porosity, the shape of pores, and pore arrangement on the elasticity of model porous materials [44,45]. Several theoretical studies have proposed theoretical models to understand the temperature, pressure, and porosity-dependent elasticity [46–49]. To date, a number of experimental studies have validated the proposed models [50–55].

However, there is a limited literature on experimental studies which characterize the influence of the pore-saturated fluid and its pressure on the elasticity of porous specimens. This study seeks to use resonant ultrasound spectroscopy (RUS) to experimentally illustrate the effects of saturated fluid properties on the elasticity of the porous material. A study of hydrostatic pressure

and temperature-dependent elasticity of selected porous ceramics will be addressed in this dissertation.

1.2 Elasticity of Thermoelectric Single Crystalline Tin Selenide (SnSe)

Thermoelectricity is the phenomenon of direct conversion of a temperature gradient across a material into an electrical potential difference, created by electron flow and vice versa. In 1821, Thomas Seebeck discovered thermoelectricity by demonstrating the growth of potential difference across two metal junctions maintained at different temperatures. When one end of the material is kept at a higher temperature than the other, the electrons in the hot region gain thermodynamic energy and diffuse toward the cold region by creating a potential difference between two ends. The measured potential difference ΔV is propotional to the temperature gradiant ΔT and the proportionality constant is known as the Seebeck coefficient *S*, which directly relates to the efficiency of the thermoelectric action [56–58].

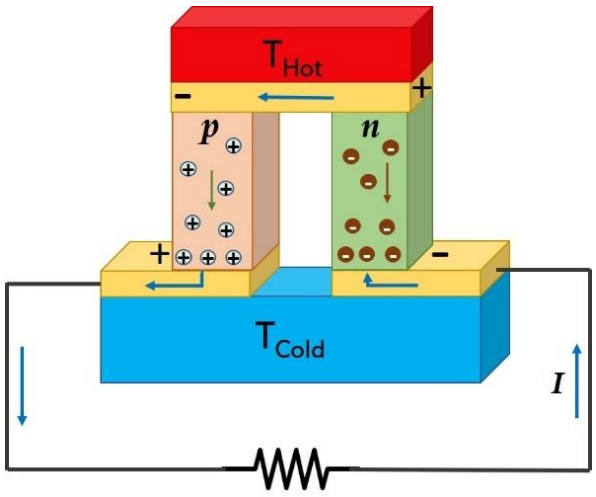

Figure 1.2. Schematic of the thermoelectric device made with *n*- and *p*-type semiconductors.

The efficiency of converting thermal energy into electricity by thermoelectric materials is determined by the dimensionless figure of merit zT, which is defined as $zT = S^2\sigma T/\kappa_T$, where S, σ, T and κ_T are Seebeck coefficient, electrical conductivity, operating temperature, and total thermal conductivity respectively [59]. The efficiency of the thermoelectric action is proportional the electrical conductivity but inversely proportional to the total thermal conductivity. The total thermal conductivity is a combination of the electronic thermal conductivity and the lattice thermal conductivity. However, most electrical conductors are also good thermal conductors. Therefore, over the past two decades, researchers have carried out both experimental and theoretical studies to develop thermoelectric materials which show high electrical conductivity and low thermal conductivity to maximize the efficiency, zT [60–62].

Single crystalline SnSe is a widely studied thermoelectric material due its reported high thermoelectric efficiency of zT ~ 2.6 at T > 900K, arising from its significantly low thermal conductivity compared to other thermoelectric materials such as PbTe, PbSe, and etc [63]. The ultralow thermal conductivity of SnSe has been attributed to its strong lattice anharmonicity and elastic anisotropy explained by the week bond arrangement in its crystal structure [64,65]. Single crystalline SnSe has a layered orthorhombic (*Pnma*) crystal structure at room temperature and it undergoes a structural phase transition from *Pnma* phase to *Cmcm* phase at T ~ 810 K [66–68]. These findings motivate the current research fields on SnSe to explore its thermal transport and structural properties at higher temperatures in order to get better understanding of their contributions on the enhancement of the thermoelectric performance [69,70]. Since elasticity measurements are often used to determine the properties of lattice vibrations, thermal transportation, and structural arrangements within crystal structures, numerous studies have been carried out to measure the elasticity of SnSe. However, these studies have been limited to

theoretical findings as the experimental measurements are yet challenging due to the low symmetry of the crystal structure, elastic anisotropy and lattice anharmonicity [71–73]. Orthorhombic SnSe has nine independent elastic constants in its elastic stiffness tensor. To date, no work has reported the experimental determination of these nine elastic constants and their temperature dependency. The lack of information of the elasticity motivated us to make the RUS measurements to evaluate the elastic tensor of single crystalline SnSe and its temperature dependency. Experimental determination of the elastic tensor of SnSe at elevated temperatures and the derivation of its elastic, structural, and thermal properties will be discussed in this study.

1.3 Outline of Dissertation

Chapter 2 discusses the theoretical background of the dissertation. This discussion starts with the derivation of linear elasticity and the elastic stiffness tensor of the crystal classes. After that, an introduction of Biot's theory of poroelasticity and its formulation will be presented. Since this dissertation covers the materials with isotropic polycrystal and anisotropic orthorhombic crystal classes, the use of elastic constants to derive the other elastic properties of those crystal classes will be addressed lastly.

Since resonant ultrasound spectroscopy is the main measurement technique employed in this dissertation, Chapter 3 provides the basics of the RUS technique, theoretical background, and RUS experimental setup used for the measurements at different temperature and hydrostatic pressure conditions. A short description of the material preparation procedure is also discussed within this section.

Chapter 4 focuses on the porous ceramic structures used in solid oxide fuel cells. The reader will be given a basic idea of the use of porous ceramics as interconnecting materials in fuel cells

to separate anode and cathode. This chapter discusses the experimental findings of the variation of elasticity of porous ceramics with the applied temperature and hydrostatic pressure conditions. The observed porous material stiffness with increasing temperature and decreasing hydrostatic pressure has been identified using the time evolution of the resonance frequencies. This preliminary study has provided a motivation to extend the experiment using different porous materials, which is discussed in chapters 5 and 6.

Chapter 5 discusses the study of hydrostatic pressure dependent elasticity of selected porous ceramics: Alumina, Zirconia, and Titania, and a comparison with that of fully dense ceramics. The main goal of this section is to investigate the change of elasticity with the hydrostatic pressures in both low and high regime. The observed material softness and increase of acoustic attenuation with increasing hydrostatic pressure will be discussed in depth in this chapter. The influence of the saturated gas type on the material softening rate will be analyzed based on the experimental observations made by using He, N, and Ar gas media.

Chapter 6 presents information about the mechanical stability of porous alumina ceramics which are placed at moderately high (~ 420 K) temperatures. The mechanical stability is discussed in terms of the time evolution of the elastic properties of the material. The porous alumina sample is placed at 423 K for about 210 hours and the resonance spectra are measured at 15minute intervals. The observed material stiffness with the time will be explained by the porosity reduction mechanisms due to the high temperature and high exposing time. Theoretical models of porosity dependent Young's modulus and shear modulus have been used for a quantitative analysis of the porosity reduction with the time. These experimental results will convey the reader about the ability of RUS technique to make most precise measurements in extreme conditions.

Chapter 7 provides the details on the experimental study of the temperature dependent elasticity of thermoelectric SnSe. First, the reader will be given an idea of the importance of measuring elastic properties of single crystalline SnSe and the limitations of the existing literature. The experimental result section has divided in to two sections: (1) Room temperature elastic properties and (2) Temperature reliant elasticity. This chapter will discuss the experimental determination of the elastic tensor of low symmetric orthorhombic crystalline material and the use of elastic constants to derive the other elastic and some thermal properties. The elastic anisotropy will be discussed using a graphical representation of directional elastic moduli and calculated anisotropic factors. The temperature-dependent elastic constants have been used to study the mechanisms of phonon decay and phonon anharmonicity observed in SnSe at high temperatures and their contribution to the enhancement of the thermoelectric efficiency. Lastly, the detection of the phase transition from *Pnma* phase to *Cmcm* phase at ~810 K will be illustrated by analyzing the temperature-dependent frequency trends.

Appendix A provides a detailed description of the modification of the python code which was used to fit the resonance frequencies with the Lorentzian line shape function.

CHAPTER 2

THEORETICAL FRAMEWORK

This chapter contains the theoretical background of the dissertation. It starts with the basic formulation of the theory of linear elasticity. And then it discusses Biot's theory of poroelasticity as an extension to the linear elasticity. Elastic constants and the derivation of other elastic properties of isotropic polycrystal and anisotropic orthorhombic crystal symmetries will be discussed in the final section.

2.1 Theory of Linear Elasticity

The theory of elasticity is the study of the mechanics of the deformation of solid materials due to applied forces. Strain and stress are the main physical measurements which characterize the elasticity of a material. In the three-dimension framework, those parameters are expressed as tensors, and Hooke's law is used to link them with the parameter called elastic stiffness tensor. All the elastic properties of the material can be described in terms of those elastic constants. This section will discuss the formulation of Hooke's law.

Let us consider a point in the solid body whose position is defined by a vector $\vec{r}(x_1, x_2, x_3)$ in 3D space. An applied force causes a displacement of that point to a new position $\overrightarrow{r'}(x_1', x_2', x_3')$ and the deformation which is known as the displacement vector $\vec{u}$ can be written as

$$\vec{u} = \overrightarrow{r'} - \vec{r}. \tag{2.1}$$

According to tensor notation the displacement vector can be expressed as

$$u_i = x_i' - x_i, \tag{2.2}$$

where the index $i = 1, 2, 3$ represents the *x*, *y* and *z* body axes. Since the vector x_i' is itself a function of the vector x_i, the small deformation of the elastic body, du_i can be written as

$$du_i = \frac{\partial u_i}{\partial x_1} dx_1 + \frac{\partial u_i}{\partial x_2} dx_2 + \frac{\partial u_i}{\partial x_3} dx_3. \tag{2.3}$$

Using Einstein summation notation,

$$\frac{du_i}{dx_j} = \frac{\partial u_i}{\partial x_j} \tag{2.4}$$

The deformation $\frac{du_i}{dx_j}$ is a rank-two tensor, which can be expressed as a combination of symmetric (ε_{ij}) and antisymmetric (θ_{ij}) tensor components:

$$\frac{du_i}{dx_j} = \frac{1}{2}\left(\frac{\partial u_i}{\partial x_j} + \frac{\partial u_j}{\partial x_i}\right) + \frac{1}{2}\left(\frac{\partial u_i}{\partial x_j} - \frac{\partial u_j}{\partial x_i}\right) = \varepsilon_{ij} + \theta_{ij}. \tag{2.5}$$

The antisymmetric tensor, θ_{ij} represents the local rigid body rotation, and it is independent of any internal elastic deformation. The symmetric tensor, ε_{ij} is the tensor component that represents the internal deformation of the body. Therefore, the elastic strain tensor is defined as

$$\varepsilon_{ij} = \frac{1}{2}\left(\frac{\partial u_i}{\partial x_j} + \frac{\partial u_j}{\partial x_i}\right). \tag{2.6}$$

Since the strain tensor is symmetric and $i, j = 1, 2, 3$, there are three diagonal and three non-diagonal terms. The diagonal terms represent compression or expansion along one of the three

axes. The non-diagonal terms correspond to the shear strain due to the deformation of a plane perpendicular to one of the three axes.

In its simplest form, stress is defined as the force acting on a unit area of a body surface. When considering a hypothetical cube inside solid material, there are two types of internal forces acting on it. Those forces are described as follows,

(1) Body force: acting on the volume of the cube (e.g. gravity).

(2) Surface force: acting on the surface of the cube (e.g. surface tension).

In theory of linear elasticity, body forces are ignored, and surface forces will produce the deformation of the cube, which is characterized by the strain tensor. When a force acts on the surface, the force component normal to the surface produces compressive or tensile stresses while the tangential component produces shear stress. When describing the stress in three dimensions, the direction of the surface normal and the direction of the force are considered. Therefore, the stress can be defined by a tensor of rank two. In general, the stress tensor component, σ_{ij} is the stress on the plane normal to j^{th} direction, arise due to the force acting in the i^{th} direction. All tensor components acting on the cubic faces are visualized in Figure 2.1.

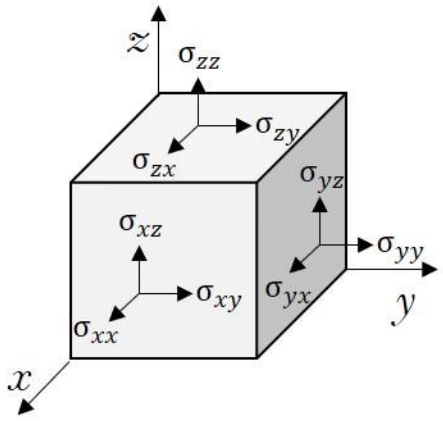

Figure 2.1. Stress tensor components acting on a cubic body.

Since we are not considering the body rotation as mentioned above, the net torque acting on the body must be zero. To satisfy this condition, the stress components must be symmetric such that $\sigma_{ij} = \sigma_{ji}$. Now we can expand σ_{ij} as a Taylor's series in ε_{kl} as follows

$$\sigma_{ij} = \sigma_{ij}(0) + \left(\frac{\partial \sigma_{ij}}{\partial \varepsilon_{kl}}\right)_{\varepsilon_{kl}=0} \varepsilon_{kl} + \frac{1}{2}\left(\frac{\partial^2 \sigma_{ij}}{\partial \varepsilon_{kl} \partial \varepsilon_{mn}}\right)_{\varepsilon_{kl}=0, \varepsilon_{mn}=0} \varepsilon_{kl}\varepsilon_{mn} + \cdots. \quad (2.7)$$

Since the stress vanishes at the zero strain for elastic bodies, the first term is $\sigma_{ij}(0) = 0$. The third term represents the third order elastic constants and nonlinear acoustics. In linear elasticity, the higher order terms after the second term are neglected and the Hooke's law is given as

$$\sigma_{ij} = c_{ijkl}\varepsilon_{kl}, \quad (2.8)$$

where the c_{ijkl} entries are elements of the elastic stiffness tensor, and they are called elastic constants. Elastic constants are the second derivatives of the free energy with respect to strain, which are simply a measure of the curvature of the interatomic potential energy (U) at the equilibrium atomic spacing (r_0) (Figure 2.2).

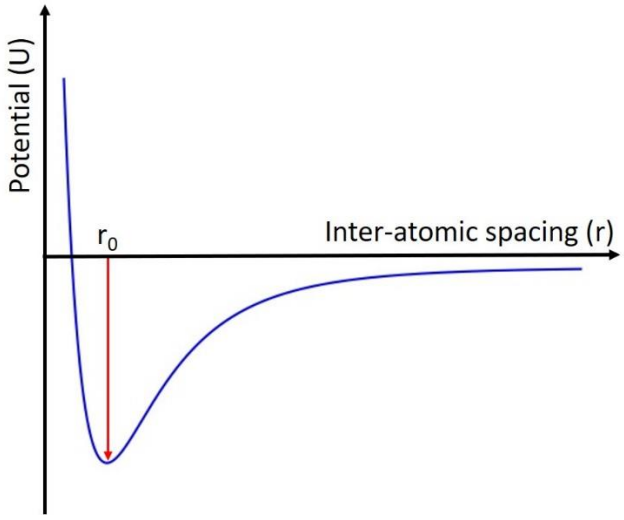

Figure 2.2. Inter-atomic potential energy curve. The gradient of potential at r is proportional to the restoring force toward the equilibrium spacing.

In general, c_{ijkl} is a 4th rank elastic stiffness tensor with 81 elements. The symmetry of the stress and strain tensors reduces the indices i, j, k, l to a two-index form i, j using the Voight convention, such that c_{ijkl} simplifies to C_{ij}, a 2nd rank 6 x 6 matrix with 36 elements. The number of independent elements is reduced to 21 (for triclinic symmetry) because of the transposition symmetry $C_{ij} = C_{ji}$. The number of non-zero independent elastic constants is further reduced by the crystallographic symmetries of crystalline materials. The simplified version of the elastic tensor C_{ij} is shown below, and the numbers of independent nonzero elastic constants for each crystallographic symmetry are tabulated in Table 2.1.

$$C_{ij} = \begin{pmatrix} C_{11} & C_{12} & C_{13} & C_{14} & C_{15} & C_{16} \\ C_{12} & C_{22} & C_{23} & C_{24} & C_{25} & C_{26} \\ C_{13} & C_{23} & C_{33} & C_{34} & C_{35} & C_{36} \\ C_{14} & C_{24} & C_{34} & C_{44} & C_{45} & C_{46} \\ C_{15} & C_{25} & C_{35} & C_{45} & C_{55} & C_{56} \\ C_{16} & C_{26} & C_{36} & C_{46} & C_{56} & C_{66} \end{pmatrix} \tag{2.9}$$

Table 2.1. Independent elastic constants for given crystal symmetries.

Crystal Symmetry	# of $\boldsymbol{C_{ij}}$	List of elastic constants
Triclinic	21	All possible combinations
Monoclinic	13	$C_{11}, C_{12}, C_{13}, C_{16}, C_{22}, C_{23}, C_{26}, C_{33}, C_{36}, C_{44}, C_{45}, C_{55}, C_{66}$
Orthorhombic	9	$C_{11}, C_{12}, C_{13}, C_{22}, C_{23}, C_{33}, C_{44}, C_{55}, C_{66}$
Trigonal	6 or 7	$C_{11}, C_{12}, C_{13}, C_{14}, C_{25}, C_{33}, C_{44}$
Tetragonal	6	$C_{11}, C_{12}, C_{13}, C_{33}, C_{44}, C_{66}$
Hexagonal	5	$C_{11}, C_{12}, C_{14}, C_{33}, C_{44}$
Cubic	3	C_{11}, C_{12}, C_{44}
Isotropic	2	C_{11}, C_{44}

The measured elastic constants of a given crystal symmetry can be used to compute the other elastic parameters such as Young's modulus (E), bulk modulus (B), shear modulus (G), Poisson's ratio (ν), transverse (v_t), and longitudinal (v_l) wave velocities and elastic anisotropic

factors. The derivation of elastic properties of isotropic and orthorhombic crystal symmetries, which have been used in this dissertation, will be discussed in detail in sections 2.3 and 2.4.

2.2 Theory of Poroelasticity

Unlike the case of fully dense solid materials, the elasticity of porous materials depends on the elastic deformation of both solid and fluid phases. Poroelasticity is a study of the mechanics of the elastic deformation of fluid-saturated porous materials. There are two basic coupling phenomena underlining the poroelastic behavior:

1. Solid-to-fluid coupling:
   Change in applied stress produces a change in fluid pressure or fluid mass.
2. Fluid-to-solid coupling:
   Change in fluid pressure or fluid mass produces a change in volume of the bulk material.

The solid-to-fluid coupling depends on the porosity and the compressibility of the solid skeleton, pores, solid grains and pore saturated fluid. For a highly compressible fluid, the magnitude of the solid-to-fluid coupling will be negligible. The theory of poroelasticity is based on the physical assumptions that the solid skeleton of the porous material is purely elastic, and the pore saturated fluid is compressible and viscous. The volume fraction porosity, ϕ is defined as the ratio of the volume of the pores, V_p to the bulk volume, V_b

$$\phi = V_p/V_b. \tag{2.10}$$

The stress tensor of the porous material can be written as

$$\sigma = \begin{pmatrix} \sigma_{xx} + \sigma_f & \sigma_{xy} & \sigma_{xz} \\ \sigma_{yx} & \sigma_{yy} + \sigma_f & \sigma_{yz} \\ \sigma_{zx} & \sigma_{zy} & \sigma_{zz} + \sigma_f \end{pmatrix}. \tag{2.11}$$

Here, the usual stress components, σ_{ij} represent the stress components that arise on the faces of a hypothetical cube of solid skeleton as described in Section 2.1. The fluid-to-solid coupling effect is represented by the total normal stress, σ_f applied to the fluid component of the faces of the cube. This coupling effect σ_f is quantified by the hydrostatic pressure, p and the porosity, ϕ,

$$\sigma_f = -\phi p. \tag{2.12}$$

According to the initial assumptions stated above, the solid skeleton has both compressibility and shearing rigidity, which validate the strain tensor given by Eq. 2.6. Since the fluid is considered compressible, it exhibits only the compressibility and the corresponding fluid strain is given by ε_f, so that the total strain becomes $\varepsilon_{ij} + \varepsilon_f$ with

$$\varepsilon_f = \frac{\partial U_x}{\partial x} + \frac{\partial U_y}{\partial y} + \frac{\partial U_z}{\partial z}. \tag{2.13}$$

Here, the U_i are the average displacements of fluid phases along the $i = x, y, z$ axes. By considering the stress and strain tensors, the generalized Hooke's law for a fluid-saturated porous material can be written as

$$\begin{pmatrix}\sigma_{xx}\\ \sigma_{yy}\\ \sigma_{zz}\\ \sigma_{yz}\\ \sigma_{zx}\\ \sigma_{xy}\\ \sigma_{f}\end{pmatrix}=\begin{pmatrix}C_{11} & C_{12} & C_{13} & C_{14} & C_{15} & C_{16} & C_{17}\\ C_{12} & C_{22} & C_{23} & C_{24} & C_{25} & C_{26} & C_{27}\\ C_{13} & C_{23} & C_{33} & C_{34} & C_{35} & C_{36} & C_{37}\\ C_{14} & C_{24} & C_{34} & C_{44} & C_{45} & C_{46} & C_{47}\\ C_{15} & C_{25} & C_{35} & C_{45} & C_{55} & C_{56} & C_{57}\\ C_{16} & C_{26} & C_{36} & C_{46} & C_{56} & C_{66} & C_{67}\\ C_{17} & C_{27} & C_{37} & C_{47} & C_{57} & C_{67} & C_{77}\end{pmatrix}\begin{pmatrix}\varepsilon_{xx}\\ \varepsilon_{yy}\\ \varepsilon_{zz}\\ \varepsilon_{yz}\\ \varepsilon_{zx}\\ \varepsilon_{xy}\\ \varepsilon_{f}\end{pmatrix}. \tag{2.14}$$

The elastic stiffness tensor of a porous material becomes a 7×7 matrix and the tensor components hold the symmetric property, $C_{ij} = C_{ji}$. In general, for i,j=1,…,6, the C_{ij} entries are the elastic constants of the elastic solid skeleton. The coefficients C_{i7} and C_{7i} represent the solid-to-fluid and fluid-to-solid coupling effects. The number of independent elastic constants are determined by the isotropic factor of the porous material. Biot has proposed the generalized elastic stiffness tensors for isotropic symmetry as follows

$$C_{ij(isotropic)}=\begin{pmatrix}P & A & A & 0 & 0 & 0 & Q\\ A & P & A & 0 & 0 & 0 & Q\\ A & A & P & 0 & 0 & 0 & Q\\ 0 & 0 & 0 & N & 0 & 0 & 0\\ 0 & 0 & 0 & 0 & N & 0 & 0\\ 0 & 0 & 0 & 0 & 0 & N & 0\\ Q & Q & Q & 0 & 0 & 0 & R\end{pmatrix}. \tag{2.15}$$

The independent constants P, A and N relate to the poroelastic moduli: Young's modulus E, shear modulus G, and Poisson's ratio ν, whereas Q and R represent the poroelastic coefficients that are due to the presence of the fluid phase. The relation between the independent constants and the poroelastic moduli and coefficients can be determined using seven linear constitutive equations.

2.2.1 Constitutive Relations in Poroelasticity

In poroelasticity, there are four basic variables, which are grouped into two conjugate pairs: i). stress (σ_{ij}) and strain (ε_{ij}) and ii). fluid pressure (p) and increment of fluid content (ξ). The increment of fluid content quantifies the removal or inclusion of fluid into the pores. Therefore, it can be expressed in terms of fluid and solid strain components as follows,

$$\xi = -\phi\left(\varepsilon_f - \varepsilon\right). \tag{2.16}$$

Negative value of ξ corresponds to the removal of fluid from the pores. Here, the volumetric solid strain is given by $\varepsilon = \varepsilon_{xx} + \varepsilon_{yy} + \varepsilon_{zz}$. The constitutive relations provide a mathematical formulation to the relationships between the four basic variables stated above. These relations are linked through the poroelastic moduli and the poroelastic constants.

For an isotropic porous material, the change of volumetric strain and increment of fluid content due to the applied stress and pressure can be written as

$$\varepsilon = \frac{1}{K}\sigma_{kk} + \frac{1}{H}p, \tag{2.17}$$

$$\xi = \frac{1}{H}\sigma_{kk} + \frac{1}{R}p, \tag{2.18}$$

where $\sigma_{kk} = \sigma_{xx} + \sigma_{yy} + \sigma_{zz}$.

The constant $\frac{1}{K} = \left(\frac{\delta\varepsilon}{\delta\sigma}\right)_{p=0}$ is known as the compressibility of the material under a constant pressure condition, and hence K is the drained bulk modulus. For the undrained condition, where the change in fluid increment is zero, the bulk modulus is renamed the undrained bulk modulus, K_u. The

change of bulk volume due to the applied pressure at constant stress is quantified by the poroelastic expansion coefficient, $\frac{1}{H} = \left(\frac{\delta\varepsilon}{\delta p}\right)_{\sigma_{kk}=0}$. The specific storage coefficient at constant stress is defined as $\frac{1}{R} = \left(\frac{\delta\xi}{\delta p}\right)_{\sigma_{kk}=0}$. This coefficient is also known as the unconstrained specific storage coefficient. These three poroelastic constants, *K*, *H* and *R*, characterize the poroelastic deformation of the material and the other elastic coefficients can be derived from them. Skempton's coefficient, $B = \left(\frac{\delta p}{\delta\sigma}\right)_{\xi=0} = \frac{R}{H}$, is defined as the ratio of induced pressure to the applied stress at undrained condition. The specific storage at constant strain is given by $\frac{1}{M} = \left(\frac{\delta\xi}{\delta p}\right)_{\varepsilon=0}$. The ratio of $\frac{K}{H}$ is known as the Biot-Willis coefficient, α. Using the above poroelastic constants and the pororelastic moduli, the linear constitutive relations for an isotropic material are given by

$$\sigma'_{ij} = 2G\varepsilon_{ij} + \left(\frac{2G\,\nu}{1-2\nu} + \alpha B K_u\right)\varepsilon\delta_{ij} - BK_u\xi\delta_{ij}, \tag{2.19}$$

$$p = -BK_u\varepsilon + \frac{BK_u}{\alpha}\xi, \tag{2.20}$$

where $\sigma'_{ij} = \sigma_{ij} + \sigma_f\delta_{ij}$ is defined as the effective stress tensor. Based on the above relations, the Hooke's law can be rearranged as

$$\begin{pmatrix} \sigma_{xx}+\sigma_f \\ \sigma_{yy}+\sigma_f \\ \sigma_{zz}+\sigma_f \\ \sigma_{yz} \\ \sigma_{zx} \\ \sigma_{xy} \\ p \end{pmatrix} = \begin{pmatrix} P & A & A & 0 & 0 & 0 & Q \\ A & P & A & 0 & 0 & 0 & Q \\ A & A & P & 0 & 0 & 0 & Q \\ 0 & 0 & 0 & N & 0 & 0 & 0 \\ 0 & 0 & 0 & 0 & N & 0 & 0 \\ 0 & 0 & 0 & 0 & 0 & N & 0 \\ Q & Q & Q & 0 & 0 & 0 & R \end{pmatrix} \begin{pmatrix} \varepsilon_{xx} \\ \varepsilon_{yy} \\ \varepsilon_{zz} \\ \varepsilon_{yz} \\ \varepsilon_{zx} \\ \varepsilon_{xy} \\ \xi \end{pmatrix}. \tag{2.21}$$

The elastic constants are given by

$$P = 2G + \left(\frac{2G\nu}{1-2\nu} + \alpha B K_u\right), \tag{2.22}$$

$$A = \frac{2G\nu}{1-2\nu} + \alpha B K_u, \tag{2.23}$$

$$N = 2G, \tag{2.24}$$

$$Q = -B K_u, \tag{2.25}$$

$$R = \frac{B K_u}{\alpha}. \tag{2.26}$$

It is important to note that the above constitutive relations are written in terms of ξ and p, instead of ε_f and σ_f, which is quite different from the Biot's notation as expressed in Eq. 2.14. Therefore, Eqs. 2.19 and 2.20 can be rearranged using Eqs. 2.12 and 2.16, so that they obey Biot's notations of stress and strain tensor components:

$$\sigma_{ij} = 2G\varepsilon_{ij} + \left(\frac{2G\,\nu}{1-2\nu} + BK_u\frac{(\alpha-\phi)^2}{\alpha}\right)\varepsilon\delta_{ij} + BK_u\phi\left(\frac{\alpha-\phi}{\alpha}\right)\varepsilon_f\delta_{ij}, \tag{2.27}$$

$$\sigma_f = BK_u\phi\left(\frac{\alpha-\phi}{\alpha}\right)\varepsilon + \frac{BK_u\phi^2}{\alpha}\varepsilon_f, \tag{2.28}$$

$$\begin{pmatrix}\sigma_{xx}\\ \sigma_{yy}\\ \sigma_{zz}\\ \sigma_{yz}\\ \sigma_{zx}\\ \sigma_{xy}\\ \sigma_{f}\end{pmatrix} = \begin{pmatrix}P & A & A & 0 & 0 & 0 & Q\\ A & P & A & 0 & 0 & 0 & Q\\ A & A & P & 0 & 0 & 0 & Q\\ 0 & 0 & 0 & N & 0 & 0 & 0\\ 0 & 0 & 0 & 0 & N & 0 & 0\\ 0 & 0 & 0 & 0 & 0 & N & 0\\ Q & Q & Q & 0 & 0 & 0 & R\end{pmatrix}\begin{pmatrix}\varepsilon_{xx}\\ \varepsilon_{yy}\\ \varepsilon_{zz}\\ \varepsilon_{yz}\\ \varepsilon_{zx}\\ \varepsilon_{xy}\\ \varepsilon_{f}\end{pmatrix}. \quad (2.29)$$

Then, the elastic constants are given by

$$P = 2G + 2G\left(\frac{\nu}{1-2\nu}\right) + BK_u\frac{(\alpha-\phi)^2}{\alpha}, \quad (2.30)$$

$$A = 2G\left(\frac{\nu}{1-2\nu}\right) + BK_u\frac{(\alpha-\phi)^2}{\alpha}, \quad (2.31)$$

$$N = 2G, \quad (2.32)$$

$$Q = BK_u\phi\left(\frac{\alpha-\phi}{\alpha}\right), \quad (2.33)$$

$$R = \frac{BK_u\phi^2}{\alpha}. \quad (2.34)$$

This theoretical treatment has explored the physical interpretations to the independent constants of elastic stiffness tensor. These independent elastic constants mainly depend on the physical parameters, such as solid material, porosity, hydrostatic pressure, and saturated fluid, which can be controlled under the experimental conditions. A modified experimental technique is required to determine the elastic constants of 7×7 tensor and then to investigate the poroelasticity of porous materials.

However, as a preliminary study to the poroelasticity, in this dissertation we are using conventional 6×6 elastic tensor assuming the porous ceramics behave as isotropic polycrystals. The measured elastic constants and elastic moduli are then recalled as effective elastic constants and moduli which are influenced by the dynamics both solid and fluid phases. Also, the variation of resonance frequencies can be examined to understand the elasticity change of the porous materials to the applied physical conditions. In this way a qualitative analysis of the variation of the elasticity with hydrostatic pressure, temperature, and saturated fluid environment will be presented in this dissertation.

2.3 Elasticity of Isotropic Polycrystals

As described in Table 2.1, there are three independent elastic constants, C_{11}, C_{12} and C_{44} for the cubic symmetry. In the isotropic scenario the elastic constant C_{12} equals to $C_{11} - 2C_{44}$, so that the elastic tensor contains two independent elastic constants. How to use of measured elastic constants to derive other elastic properties is summarized in Table 2.2.

$$C_{ij\ (isotropic)} = \begin{pmatrix} C_{11} & C_{12} & C_{12} & 0 & 0 & 0 \\ C_{12} & C_{11} & C_{12} & 0 & 0 & 0 \\ C_{12} & C_{12} & C_{11} & 0 & 0 & 0 \\ 0 & 0 & 0 & C_{44} & 0 & 0 \\ 0 & 0 & 0 & 0 & C_{44} & 0 \\ 0 & 0 & 0 & 0 & 0 & C_{44} \end{pmatrix} \tag{2.35}$$

Table 2.2. Elastic parameters of isotropic polycrystalline materials.

Elastic Parameter	**Equation**	**Equation #**
Shear Modulus (G)	$G = C_{44}$	(2.36)
Young's Modulus (E)	$E = \frac{C_{44}(3C_{11} - 4C_{44})}{(C_{11} - C_{44})}$	(2.37)
Bulk Modulus (B)	$B = \frac{EG}{(9G - 3E)}$	(2.38)
Poisson Ratio (ν)	$\nu = \frac{C_{11} - 2C_{44}}{2(C_{11} - C_{44})}$	(2.39)
Transverse Velocity (v_t)	$v_t = \sqrt{C_{44}/\rho}$	(2.40)
Longitudinal Velocity (v_l)	$v_l = \sqrt{C_{11}/\rho}$	(2.41)

*ρ = Density of the material

2.4 Elasticity of Anisotropic Orthorhombic Crystals

Orthorhombic crystal symmetry owns nine independent elastic constants in its elastic tensor, showing a highly elastic anisotropic behavior. The nine elastic constants can be grouped into three major categories as:

1. Extensional modes - C_{11}, C_{22}, C_{33}
2. Shear modes - C_{44}, C_{55}, C_{66}
3. Weekly coupled off diagonal - C_{12}, C_{13}, C_{23}

$$C_{ij(Orthorhombic)} = \begin{pmatrix} C_{11} & C_{12} & C_{13} & 0 & 0 & 0 \\ C_{12} & C_{22} & C_{23} & 0 & 0 & 0 \\ C_{13} & C_{23} & C_{33} & 0 & 0 & 0 \\ 0 & 0 & 0 & C_{44} & 0 & 0 \\ 0 & 0 & 0 & 0 & C_{55} & 0 \\ 0 & 0 & 0 & 0 & 0 & C_{66} \end{pmatrix} \quad (2.42)$$

The elastic anisotropy of orthorhombic symmetry can be analyzed by the orientation dependence of Young's modulus, *E* and the bulk modulus, *B* as described in the following equations. These relations can be used to visualize the elastic anisotropy graphically:

$$\frac{1}{E} = S_{11}l_1^4 + S_{22}l_2^4 + S_{33}l_3^4 + (2S_{12} + S_{66})l_1^2l_2^2 + (2S_{23} + S_{44})l_3^2l_2^2 + (2S_{13} + S_{55})l_1^2l_3^2, \tag{2.43}$$

$$\frac{1}{B} = (S_{11} + S_{12} + S_{13})l_1^2 + (S_{22} + S_{12} + S_{23})l_2^2 + (S_{33} + S_{23} + S_{13})l_3^2. \tag{2.44}$$

Here, the S_{ij} are elements of the elastic compliance tensor, $S_{ij} = C_{ij}^{-1}$, and l_i are the direction cosines along the *x*, *y* and *z* crystallographic axes. In addition, the axial bulk moduli, B_x, B_y, B_z, along the *x*, *y* and *z* axes can be expressed as

$$B_x = \frac{\chi}{1+\alpha+\beta},\ B_y = \frac{B_x}{\alpha},\ B_z = \frac{B_x}{\beta}, \tag{2.45}$$

where

$$\chi = C_{11} + 2C_{12}\alpha + C_{22}\alpha^2 + 2C_{13}\beta + C_{33}\beta^2 + 2C_{23}\alpha\beta,$$

$$\alpha = \frac{(C_{11}-C_{12})(C_{33}-C_{13})-(C_{23}-C_{13})(C_{11}-C_{13})}{(C_{33}-C_{13})(C_{22}-C_{12})-(C_{13}-C_{23})(C_{12}-C_{23})}, \tag{2.46}$$

$$\beta = \frac{(C_{22}-C_{12})(C_{11}-C_{13})-(C_{11}-C_{12})(C_{23}-C_{12})}{(C_{22}-C_{12})(C_{33}-C_{13})-(C_{12}-C_{23})(C_{13}-C_{23})}.$$

The anisotropic factors are the parameters which measure the degree of elastic anisotropy of a given crystal symmetry. The given crystal is elastically isotropic when an anisotropy factor equals one, and any departure from one corresponds to a degree of elastic anisotropy. The anisotropy factors of bulk moduli along *x* and *z* axes with respect to *y* axis are defined by $A_x = B_x/B_y$ and $A_z = B_z/B_y$. The shear anisotropy factors (A_i) provide a measure of the degree of anisotropy in the bonding between atoms in different planes and they can be described as follows:

The shear anisotropic factor for the

1. $\{100\}$ plane between $\langle 011\rangle$ and $\langle 010\rangle$ directions,

$$A_1 = 4C_{44}/(C_{11} + C_{33} - 2C_{13}); \tag{2.47}$$

2. $\{010\}$ plane between $\langle 101\rangle$ and $\langle 001\rangle$ directions,

$$A_2 = 4C_{55}/(C_{22} + C_{33} - 2C_{23}); \tag{2.48}$$

3. $\{001\}$ plane between $\langle 110\rangle$ and $\langle 010\rangle$ directions,

$$A_3 = 4C_{66}/(C_{11} + C_{22} - 2C_{12}). \tag{2.49}$$

For an anisotropic low-symmetric crystal, the Voight-Ruess-Hill (VRH) approximation is used to convert the anisotropic elastic constants to the macroscopic elastic moduli which represent the average (effective) elasticity of the crystalline material. According to the Voigt assumption, the bulk (B_V) and the shear moduli (G_V) are expressed as

$$B_V = \frac{1}{9}(C_{11} + C_{22} + C_{33} + 2C_{12} + 2C_{13} + 2C_{23}), \tag{2.50}$$

$$G_V = \frac{1}{15}(C_{11} + C_{22} + C_{33} - C_{12} - C_{13} - C_{23} + 3C_{44} + 3C_{55} + 3C_{66}). \tag{2.51}$$

From the Reuss approximation, these moduli are expressed as

$$B_R = \frac{1}{(S_{11}+S_{22}+S_{33})+2(S_{12}+S_{13}+S_{23})}, \tag{2.52}$$

$$G_R = \frac{15}{4(S_{11}+S_{22}+S_{33})-4(S_{12}+S_{13}+S_{23})+3(S_{44}+S_{55}+S_{66})}. \tag{2.53}$$

The Voigt equations represent the upper limit of the polycrystalline constants, while the Reuss equations represent the lower limit. Therefore, the elastic moduli can be approximated by Hill's average and hence the bulk and shear moduli can be expressed as

$$B = \frac{(B_V + B_R)}{2}, \qquad G = \frac{(G_V + G_R)}{2}. \tag{2.54}$$

The above calculated shear and bulk modulus is used to calculate the other polycrystalline elastic properties, as described in Table 2.2. The calculations of the elastic properties of orthorhombic single crystalline SnSe will be presented in Chapter 7.

CHAPTER 3

RESONANT ULTRASOUND SPECTROSCOPY

3.1 Introduction

Resonant Ultrasound Spectroscopy (RUS) is a widely used, efficient, and precise experimental technique to determine the elastic tensor of materials with different crystal structures. Compared to other conventional mechanical testing methods, RUS has gained interest among the experimental material science fields due to its precision, ability to resolve all elastic constants in a single measurement and its ability to take measurements over a range of temperatures and hydrostatic pressures. In RUS, a polished rectangular parallelepiped shaped crystal specimen is placed in between two acoustic transducers, one of which drives the sample in a swept-frequency continuous wave (CW) mode over a selected frequency range, while the other detects the sample response to the excitation (Figure 3.1). The resonance spectrum is obtained by plotting the sample response over the driving frequency. At the resonance, where the drive frequency matches the natural vibration frequency of the sample, the sample surface shows a maximum displacement which produces a peak in the resonance spectrum. The center frequency and quality factor of each peak are extracted by fitting the displacement data to a Lorentzian function. Next, an iterative procedure that entails the crystal geometry and density is used to "match" the experimental frequencies with the calculated spectrum. This then allows determination of all elastic constants of the crystal from a single frequency scan. The instrumentations and computations associated with RUS technique will be discussed in the following sections.

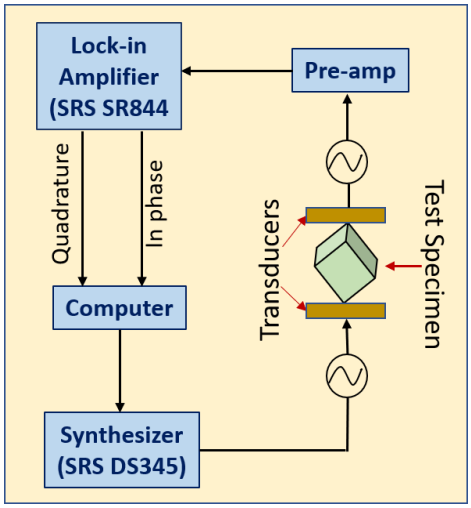

Figure 3.1. Schematic of the RUS setup.

3.2 RUS Computation

3.2.1 Analyzing the Resonance Spectrum

As described in the introduction, the receiver transducer detects the sample's surface vibration and converts the motion into an alternative current (AC) which is driven into a lock-in amplifier. The lock-in amplifier converts that input AC signal into two DC signal components called 'in-phase' and 'quadrature'. To illustrate this process, let us consider the input signal to the lock-in is $V_{sig} = V_s \sin(\omega_s t + \theta_s)$ where V_s is the signal amplitude, ω_s is the signal frequency, and θ_s is the signal's phase. A lock-in amplifier generates an internal reference signal, $V_L = V_r \sin(\omega_r t + \theta_r)$ and then multiplies it by the input signal using a phase sensitive detector (PSD) or multiplier. The multiplied signal,V_{PSD1} can be written as

$$V_{PSD1} = V_s V_L \sin(\omega_s t + \theta_s) \sin(\omega_r t + \theta_r)$$
$$V_{PSD1} = \frac{1}{2} V_s V_r \cos([\omega_s - \omega_r]t + \theta_s - \theta_r) + \frac{1}{2} V_s V_r \cos([\omega_s + \omega_r]t + \theta_s + \theta_r). \quad (3.1)$$

The multiplied signal is a combination of two AC signals, one with the difference frequency $(\omega_s - \omega_r)$ and the other with the sum frequency $(\omega_s + \omega_r)$. When $(\omega_s = \omega_r)$, the difference frequency component becomes a DC signal, and hence V_{PSD1} now contains both AC and DC signal components. The AC component can be easily removed using a low pass filter, and the resultant will give a pure DC signal whose amplitude is proportional to the signal amplitude measured by the transducer.

$$V_{PSD1} = V\cos(\theta_s - \theta_r) \tag{3.2}$$

Where $V = \frac{1}{2}V_s V_r$. Similarly another PSD is used to multiply the input signal by the lock-in reference signal shifted by 90° such that $V_L = V_r \sin(\omega_r t + \theta_r + \pi/2)$. Then the output DC signal can be written as

$$V_{PSD2} = V\sin(\theta_s - \theta_r) \tag{3.3}$$

Here, V_{PSD1} is called the 'in-phase' component and the V_{PSD2} is called the 'quadrature' component of the input signal.

RUS instrumentation has been programmed to record both in-phase and quadrature signal amplitudes with corresponding driving frequencies. Figure 3.2 shows a resonance spectrum in which both signal components are plotted against the driving frequencies. Each signal peak represents a normal mode vibration associated with the center frequency f_0.

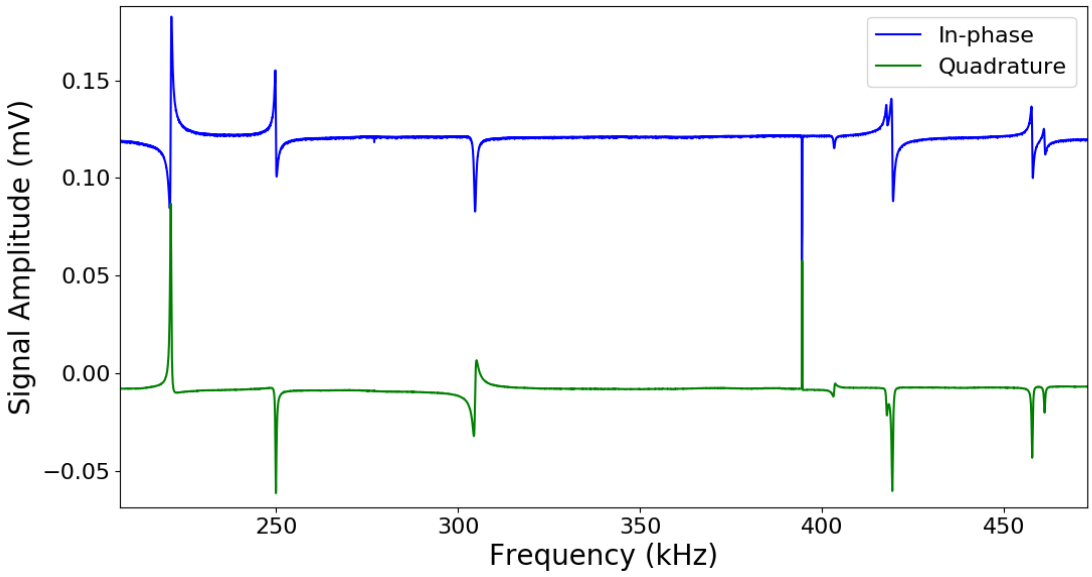

Figure 3.2. Resonance spectrum as a function of in-phase and quadrature signal.

The quadrature signal, which contains the phase information, is used to analyze the resonance peaks as they can be fitted into the Lorentzian line shape function (Eq. 3.4). The Lorentzian curve fit provides the center frequency, the quality factor (Q) and phase information of each resonance peak. Figure 3.3 illustrate the curve fit and its outputs. The fitting routine is applied for each resonance peaks to obtain the list of normal mode frequencies:

$$y(f) = \frac{A\left(\frac{f}{f_0 \cos(\phi)} + \left(1 - \left(\frac{f}{f_0}\right)^2\right) Q \sin(\phi)\right)}{\left(\frac{f}{f_0}\right)^2 + \left(1 - \left(\frac{f}{f_0}\right)^2\right)^2 Q^2} + y_0(f), \tag{3.4}$$

Where the background function $y_0(f)$ is defined as

$$y_0(f) = a_0 + a_1(f - f_0) + a_2(f - f_0)^2 + a_3(f - f_0)^3. \tag{3.5}$$

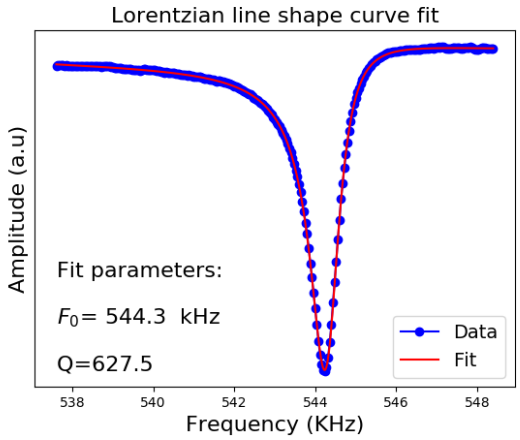

Figure 3.3. Lorentzian line shape curve fit applied to a resonance peak.

3.2.2 Resonance Frequency Determination

The Rayleigh-Ritz method is a widely used, classical method for calculating the approximate vibrational frequencies of an elastic body. This method is based on the Hamilton's principle of least action that the Lagrangian of a system is stationary with respect to small perturbations in the eigenfunctions. The derivation starts with the definition of kinetic and potential energies and the Lagrangian of the system. The kinetic energy density for a normal mode of the elastic system can be written as

$$T = \frac{1}{2}\rho\omega^2 u_i u_i \,, \tag{3.6}$$

where ω is the angular frequency of the normal mode vibration and u_i is the displacement vector. The potential energy density is given by

$$U = \frac{1}{2}c_{ijkl}\varepsilon_{ij}\varepsilon_{kl} = \frac{1}{2}c_{ijkl}\frac{1}{2}\left(\frac{\partial u_i}{\partial x_j} + \frac{\partial u_j}{\partial x_i}\right)\frac{1}{2}\left(\frac{\partial u_k}{\partial x_l} + \frac{\partial u_l}{\partial x_k}\right). \tag{3.7}$$

The symmetry $c_{ijkl} = c_{jilk}$ allows us to simplify Eq. 3.7 as

$$U = \frac{1}{2} c_{ijkl} \left(\frac{\partial u_i}{\partial x_j} \frac{\partial u_k}{\partial x_l} \right). \tag{3.8}$$

By combining kinetic and potential energy densities, the Lagrangian (L) of the system can be expressed as a volume integral of $T - U$,

$$L = \int_V (T - U)\ dV$$
$$L = \frac{1}{2} \int_V \left(\rho \omega^2 u_i u_i - c_{ijkl} \left(\frac{\partial u_i}{\partial x_j} \frac{\partial u_k}{\partial x_l} \right) \right) dV. \tag{3.9}$$

According to the Hamilton's variational principle, the time integral of the Lagrangian, which is known as the action, is a constant of the motion (Eq. 3.10). This principle leads us to derive an expression for the normal mode frequencies as a function of the elastic stiffness tensor and the geometrical information of the solid body (Eq. 3.11):

$$\delta \int_{t_1}^{t_2} \frac{1}{2} \int_V \left(\rho \omega^2 u_i u_i - c_{ijkl} \left(\frac{\partial u_i}{\partial x_j} \frac{\partial u_k}{\partial x_l} \right) \right) dV dt = 0\,, \tag{3.10}$$

$$\omega^2 = \frac{\int_V c_{ijkl} \left(\frac{\partial u_i \partial u_k}{\partial x_j \partial x_l} \right) dV}{\int_V \rho u_i u_i\, dV}. \tag{3.11}$$

The above equation provides an abstract approach to compute the normal mode frequencies using the displacement vectors u_i, elastic tensor c_{ijkl} and the density ρ, known as the "forward" problem of solving resonance frequencies. The Rayleigh-Ritz method is used to solve the "forward" problem using free boundary conditions and minimized Lagrangian mentioned in Eq. 3.10. The boundary value problem provides eigenvalues, $\omega_n = 2\pi f_n$ yielding resonance frequencies of a solid body. To apply the Rayleigh- Ritz method, the displacement field is defined as an expansion of some of suitable set of basis functions.

$$u_i = \sum_{i=1}^{N} a_{in}\varphi_n \tag{3.12}$$

Finding a suitable basis function which can apply for any shape of the object was a challenging task for the theorist as well as experimentalists. Finally, they ended up with a solution which suggested that polynomial functions are good choice for basis functions as there are standard solutions for their integrals and derivatives. Also, high order polynomials can be used to represent many shapes. In 1991, W. M. Visscher et al. [4] proposed a simple set of basis functions written by simple powers of Cartesian coordinates.

$$\varphi_n = x^p y^q z^r \tag{3.13}$$

Now, the kinetic energy density, E_{nimj} and the potential energy density, Γ_{nimj} are redefined with the new basis function as follows

$$E_{nimj} = \delta_{ij} \int_V \rho\varphi_n\varphi_m \, dV, \tag{3.14}$$

$$\Gamma_{nimj} = C_{ijkl} \int_V \frac{\partial\varphi_n}{\partial x_k}\frac{\partial\varphi_m}{\partial x_l} \, dV. \tag{3.15}$$

The solutions for the free vibration problem can be obtained by considering the requirement that the variation of Lagrangian with respect to $\vec{a}$ is zero. This yields the following matrix eigenvalue equation by simplifying the problem.

$$\Gamma\vec{a} = \omega^2 E\vec{a} \tag{3.16}$$

The components of the vector $\vec{a}$ are the expansion coefficients defined in the expansion of displacement field u_i in the Eq. 3.12. In general, the matrix *E* is not diagonal, but it becomes symmetric and positive definite upon the choice of orthonormal basis. By the definition Γ is symmetric always and it leads to a quick and easy solutions for the eigenvalues and eigenvectors. Here, the eigenvalues correspond to the square of the angular frequencies of normal modes. The forward calculation involves solving the above eigenvalue equation 3.16 to find a set of $\vec{a}$ components which minimize the Lagrangian and then computing the eigenvalues (calculated resonance frequencies) using initially provided elastic tensor elements c_{ijkl}.

3.2.3 Estimation of Elastic Constants

The key concept of RUS technique involves with the "inverse" problem which determines the elastic tensor of a solid body using a set of experimentally obtained normal mode frequencies. However, the above eigenvalue equation cannot be inverted mathematically to perform the inverse problem. In RUS, solving for the inverse problem is achieved by performing forward calculation to obtain normal mode frequencies from initially guessed elastic constants and then proceeding through an iterative minimization algorithm which compares the calculated frequencies to experimentally measured resonance frequencies. The parameters, elastic constants are adjusted during each iteration to minimize the error function (*F*), which is defined as the sum of the squares of the deference between the calculated, $f_i^{(calc)}$ and measured, $f_i^{(meas)}$ frequencies.

$$F = \frac{1}{2}\sum_{i=1}^{M} w_i\left[f_i^{(calc)} - f_i^{(meas)}\right]^2 \tag{3.17}$$

Levenberg-Marquardt algorithm is used to minimize the above error function, by using the assumption of a parabolic error surface near the minimum. The adjusted parameters at the error minima are considered as the fitted elastic constants. The structures of the input data and the output results of the computational fitting algorithm is shown in Figure 3.4. In this nonlinear fitting routine, a care must be taken to avoid converging the solution to a local minimum rather than the global minimum in the error space. Larger deviations of the guessed elastic constants with their actual values, missing normal mode frequencies, fewer number of normal mode frequencies, imperfection of the sample geometry and the misalignment of crystal axis with the body axis lead to a local minimum.

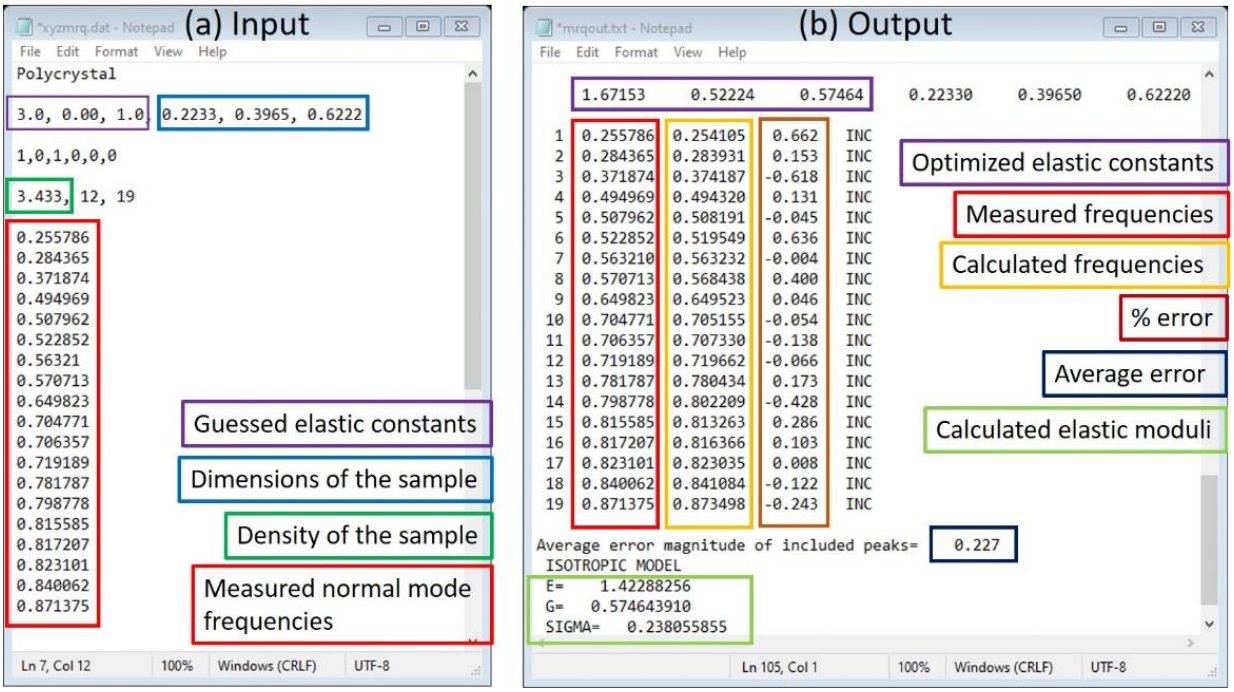

Figure 3.4. The data structures of (a) input parameters and (b) output results of the nonlinear fitting algorithm of the elastic constants optimization.

3.3 High Temperature RUS Setup

RUS instrumentation for measurement at high temperatures is another challenging task because of the limitation of materials' abilities to withstand high temperature conditions. For an example, plastic, Pb based solders, and rubber materials cannot be utilized in designing the high temperature RUS setup. A typical direct contact transducer system made with gold-plated lithium niobate ($LiNbO_3$) piezoelectric crystals is shown in Figure 3.5(a). Here, thermo-coaxial cables, made with metal conductors separated by a mineral insulator, are used to connect the transducers. The rigidity of the coaxial cables provides an additional structural support to the transducer system and it will provide enough weight to prevent the loose contact between the sample and transducers. Since Pb based solders start to melt at ~ 450 K, silver based conductive epoxy is used as bonding agent to connect the transducers with the coaxial cables. The epoxy exhibits good electrical conductivity as well as the mechanical stability at high temperatures ~1000 K. For high temperature measurements, the transducer cage is placed inside a properly sealed quartz tube which runs through a tube furnace (Carbolite Model MTF12/38/250), as in Figure 3.5(b). An n-type thermocouple with the resolution of 0.01 K is used to measure the temperature near the sample. This system is facilitated with an inert gas flow (typically Argon) through the tube to reduce the oxygen level and hence to prevent any oxidations at higher temperatures. The oxygen level inside the tube is monitored by the oxygen analyzer. The experimental setup is shown in Figure 3.5(c).

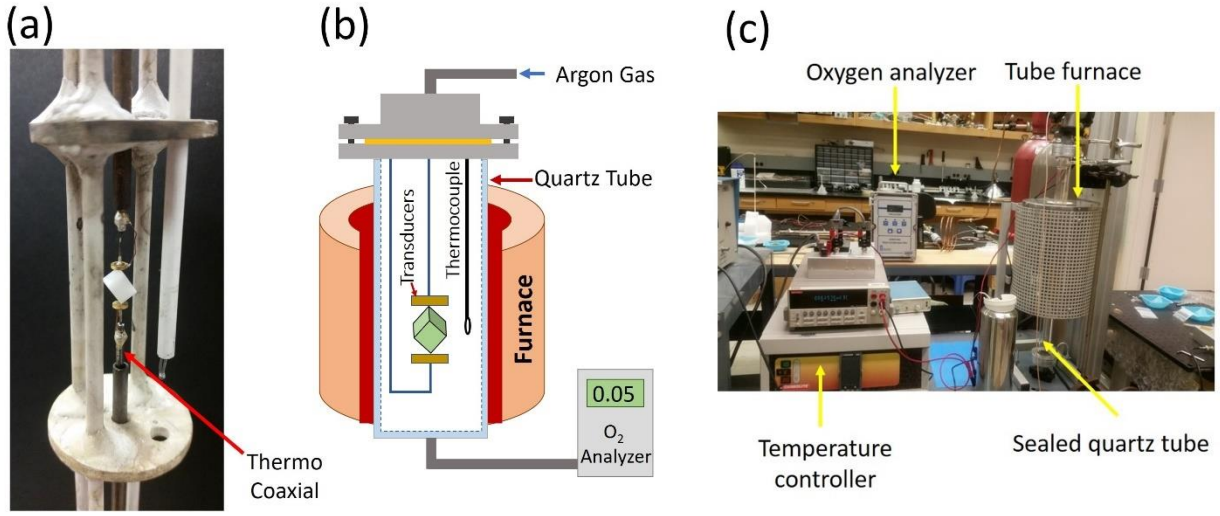

Figure 3.5. (a) Direct contact transducer system, (b) schematic of the high temperature RUS kit and (c) the instrument arrangement in the RUS lab.

The use of direct contact transducer system is limited up to ~800 K due to the upper operating temperature limitations of piezo crystals and adhesive epoxy. $LiNbO_3$ transducers lose their piezoelectricity after 800 K, and hence they cannot be used at the temperatures greater than 800K. To overcome this circumstance, a buffer rod transducer system (Figure 3.6) has been introduced. Here, thin and long cylindrical rods made out with ceramic alumina or fused quartz, whose acoustic attenuation is low, are used as acoustic waveguides. As shown in Figure 3.6(a), two buffer rods are used, and the transducers are mounted at the one end of each rod. The sample directly contacts with the buffer rods. The lower buffer rod propagates the acoustic signal generated by the driving transducer and drives the sample. The upper buffer rod detects the sample response and propagates that vibration to the receiver transducer. In this way, the transducers are kept away from the extremely hot region while the sample is at extremely high temperatures greater than 800 K. This system can be used to make the measurements up to 1200 K. The length

of the buffer rods has been optimized with respect to transmission loss and heat gradient inside the cell.

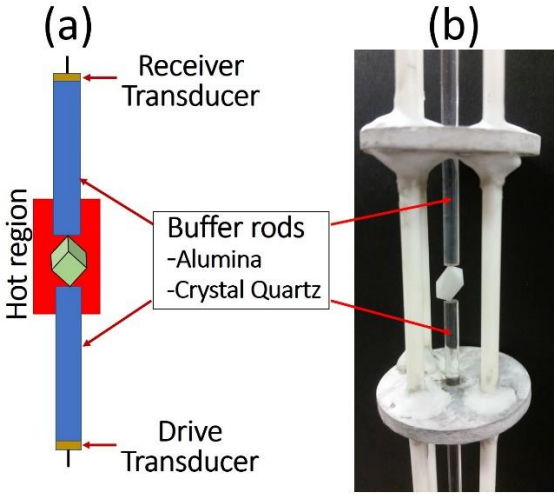

Figure 3.6. (a) Schematic and (b) a picture of buffer rod transducer system used in high temperature RUS measurements.

3.4 High- and Low-Pressure RUS Setup

For the RUS measurements at high pressure conditions, a stainless-steel tube is used instead of a quartz tube, as shown in the high-temperature setup (Figure 3.7). The upper end of the tube is designed to fill the gas from the tanks, while the lower end is connected to a vacuum pump for gas removal process. At its maximum operation, the vacuum pump (Cooltech 15400) reduces the pressure inside the cell to 0.1 torr. Both gas filling and removal are controlled by needle valves. A digital pressure gauge with the resolution of 0.1 torr and an analogue pressure gauge with the resolution of 50 psi are used to measure the hydrostatic pressure in vacuum- and high-pressure levels respectively.

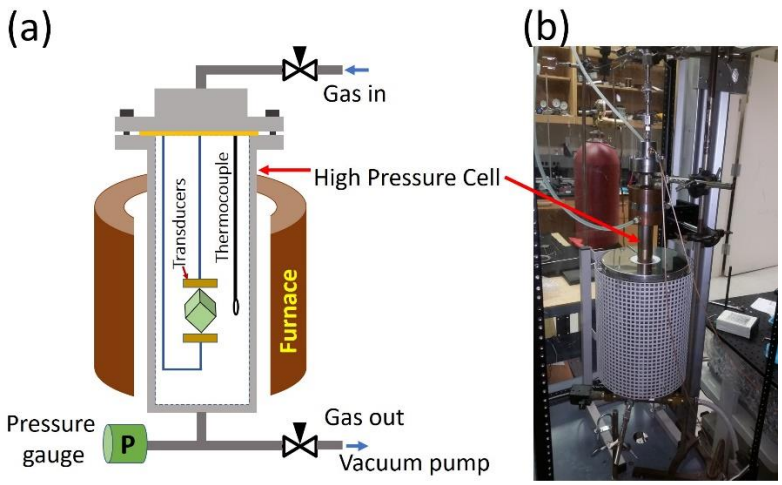

Figure 3.7. (a) Schematic of the cell arrangement for the RUS measurements at high- and low-pressures, and (b) the experimental setup.

3.5 Sample Preparation

The material samples received for the RUS measurements are always in different shapes according to the application that they have been used for. Therefore, sample preparation to a specific geometrical shape, such as spheres, cylinders and cubes, with precise measurement of its dimensions, is an important task as the RUS computational techniques have been developed to compute the elastic constants of the standard geometries. Parallelepipeds are the most used geometry due to the convenience and simplicity in the computational process. The imperfection of the sample geometry leads to inaccurate estimate of the elastic constants.

The sample preparation procedure is shown in the following flow chart in Figure 3.8. A low speed diamond saw is used to cut the rectangular parallelepiped samples from the bulk sample and a water based lapping machine is used to polish the sample surfaces. At each cutting and polishing process, the sample is mounted to appropriate devices designed for each machine and covered with wax to prevent any damages to the edges and corners of the sample. An optical

microscope is used to monitor the geometrical angles and the surface quality of the parallelepipeds. Prepared samples are then cleaned to remove any surface residue from materials exposed during sample preparation and dried well to evaporate any solvent that might absorb into the specimen. An acetone and ethanol based ultrasonic cleaning technique: 20-minute cleaning with acetone and then another 20-minute cleaning with ethanol, is followed. A micrometer and high precision mass scale are used to measure sample dimensions and mass. Care must be taken in handling and mounting the samples in the RUS transducer system to avoid any damages and contaminations.

For single crystalline materials with lower symmetries, the alignments of crystallographic directions with the sample body axes need to be determined during preparation of test specimens. X-ray diffraction (XRD) measurements can be used to determine crystallographic directions. Any offset with crystallography directions to the sample alignment, measured by Euler angles, should be included in the computational routine.

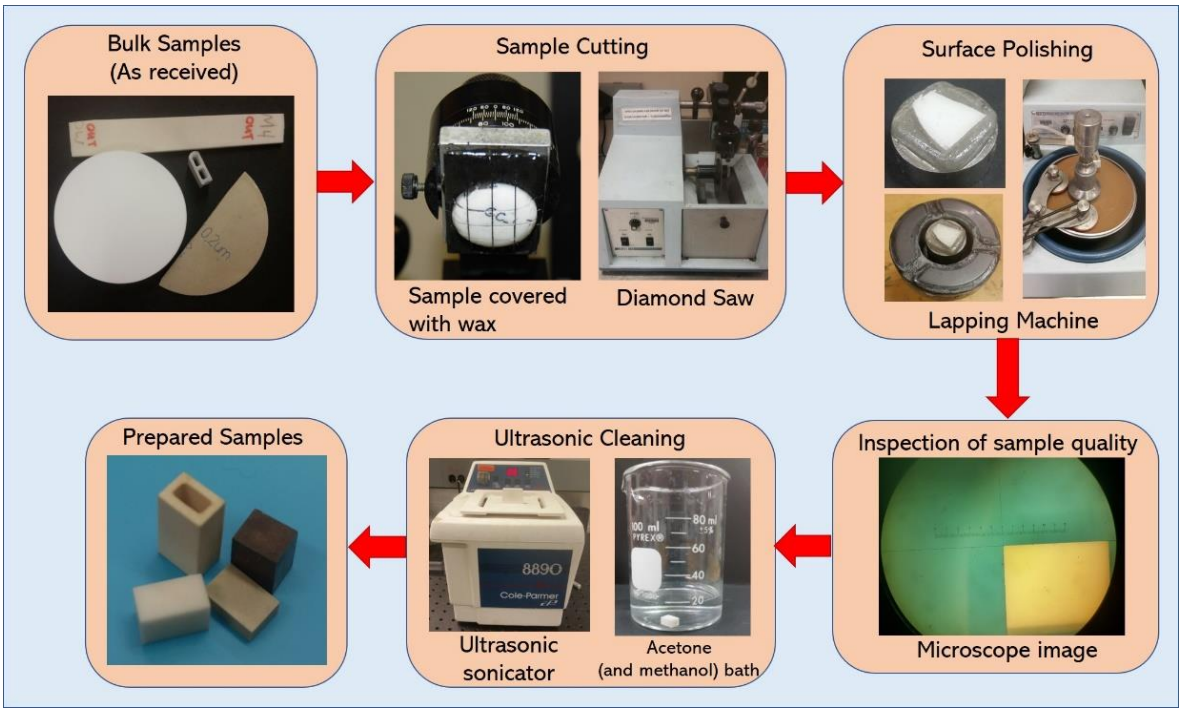

Figure 3.8. Sample preparation procedure.

CHAPTER 4

A PRELIMINARY STUDY ON THE TEMPERATURE AND PRESSURE DEPENDENT ELASTICITY OF POROUS CERAMICS DESIGNED FOR SOLID OXIDE FUEL CELLS

4.1 Introduction

Solid oxide fuel cell systems are usually made as a stack of individual cells (Figure 4.1). An interconnecting material, which allows gas exchange and mechanical stability, is used to separate those individual cells. LG Fuel Cells Systems, Inc. uses a rectangular tube structured porous ceramic material as an interconnecting phase. Since fuel cells are operated at high temperature environments, it is important to study the temperature dependent mechanical properties of the materials used. This experiment was designed and performed to study the elasticity of porous ceramics at different temperature and hydrostatic pressure conditions.

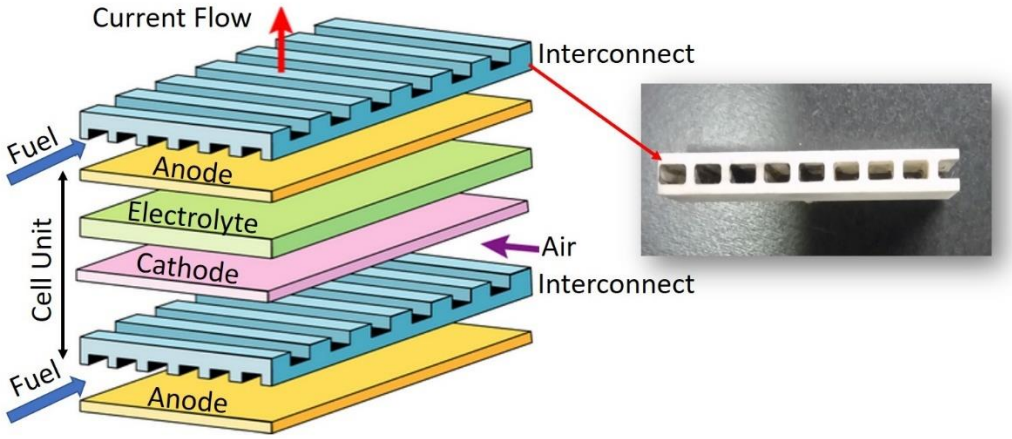

Figure 4.1. Schematic of a hydrogen fuel cell and the interconnecting structure made with porous ceramics.

4.2 Sample Preparation

The as-received sample was a rectangular-tube-structured porous ceramic sample with wall thickness ~ 1 mm (Figure 4.1). A thin sample was prepared by separating a wall of the bulk sample as shown in Figure 4.2(a). The thickness of the sample was around 0.8 mm. An experimental setup was designed to measure resonance spectra at elevated temperatures under partial vacuum conditions (Section 3.4). The resonance spectra were obtained with lower signal-to-noise ratio, which caused difficulties when identifying exact sample resonance peaks. Reduction in signals is attributed to high damping and small sample size. Therefore, rectangular tubular parallelepipeds (Figure 4.2(b)) were sectioned from the bulk sample as described in the sample preparation Section 3.5. The dimensions and the masses of the samples are tabulated in Table 4.1. The resonance spectra measured from the tube sample exhibited higher signal-to-noise ratio when compared to that of the thin sample. Therefore, tube samples were used for the preliminary RUS measurements at different pressure and temperature conditions.

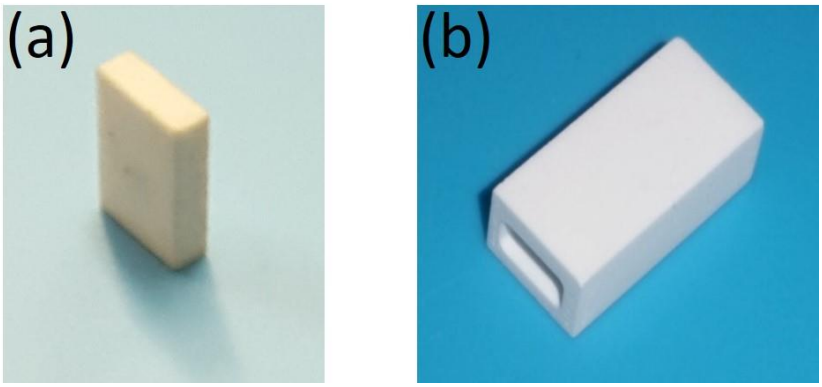

Figure 4.2. (a) Thin sample and (b) Tube sample prepared from the bulk material.

Table 4.1. The dimensions and mass data of tube samples.

Measurement	Sample A	Sample B
Height (cm)	0.9910	0.9932
Outer length (cm)	0.4851	0.5080
Outer width (cm)	0.3561	0.3570
Mass (g)	0.3067	0.3260

4.3 Experimental Procedure

Although the tube samples offered a reasonable resonance spectrum, we observed further signal-to-noise ratio reduction mechanisms, especially the damping due to the moisture and any liquid trapped inside the pores during the sample preparation process, which reduced the number of resonance peaks visible in the resonance spectrum. The tube sample-A was mounted in the transducer system which sat inside the high-pressure cell as described in Section 3.4. To eliminate the moisture and residual liquid phases, the pressure inside the cell was reduced to 23 Torr (~0.03 atm) and the temperature was raised until a significant spectrum was obtained. The drying process helps to vaporize any liquid phases trapped inside the pores. Resonance spectra were measured at each temperature increment and a growth of the signal strength of the resonance peaks was observed as shown in Figure 4.3. A reasonable resonance spectrum was obtained at 498 K (225˚C) and resonance spectra were measured at every 30 minutes intervals for a duration of 17 hours while the system was allowed to stabilize.

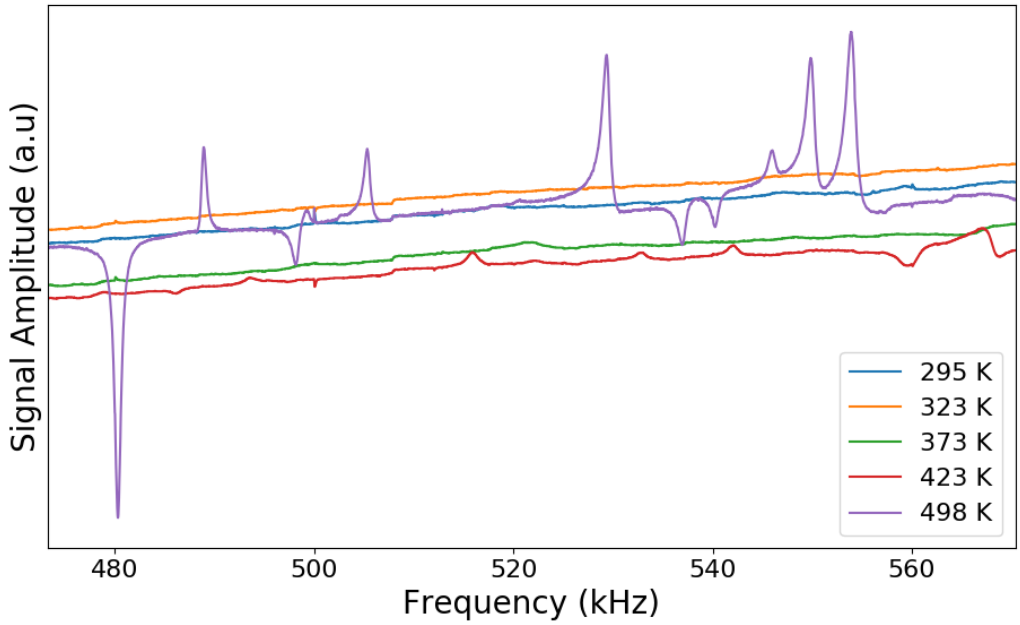

Figure 4.3. Growth of the quality of resonance spectrum with increasing temperature.

A similar procedure was repeated for sample-B until a significant spectrum was obtained. A significant spectrum was obtained at 511 K (238˚C) and the system was allowed to stabilize. Resonance spectra were collected at 20 minutes intervals for an additional 19 hours at 511 K. The system was then cooled to room temperature. Resonance spectra were measured at different temperature points while the sample was cooling. After that, the system was maintained under vacuum at room temperature for about 12 hours. Another temperature cycle was performed from 295 K to 507 K, and the resonance spectra were measured during the heating and cooling cycles. Finally, the resonance spectra were obtained by varying the pressure from 760 Torr (1 atm) to 23 Torr (0.03 atm) at room temperature. The analyses of the observed results are presented in the following section.

4.4 Results and Discussion

The measured resonance spectra have exhibited a peak growth with increasing temperature. This peak growth is possibly due to the reduction of damping by the purging of gas and liquid from the voids within the material structure. Although, the tube samples provided a reasonable resonance spectrum at high temperatures, the elastic constant fitting routine was challenging due to the geometry of the sample. However, the elasticity of the material can be studied by analyzing squares of the trends of normal mode frequencies (f^2) as they are proportional to the elastic constants. Therefore, in this study we discuss the elastic behavior of the test specimens by analyzing the normal mode frequencies. Figure 4.4 shows the variation of the resonance frequencies over time, measured from sample-A and sample-B at 498 K and 511 K respectively.

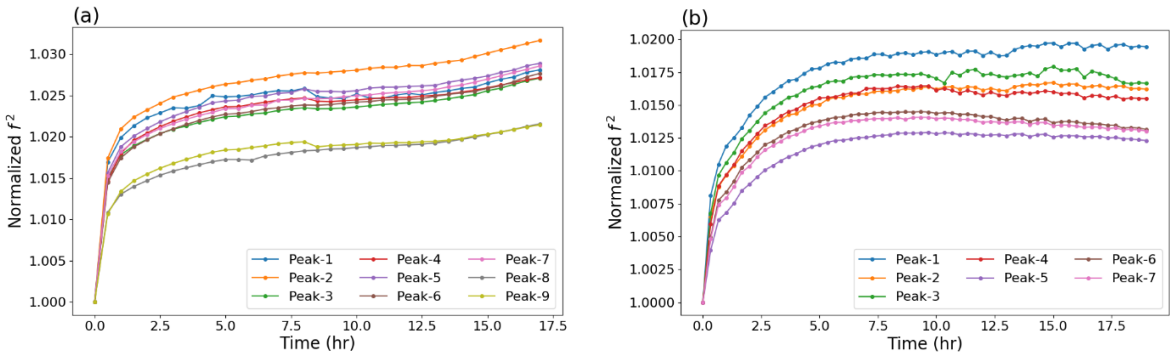

Figure 4.4. Time variations of squared resonance frequencies measured from (a) sample-A at 498 K and (b) Sample-B at 511 K, in the partial vacuum of 23 Torr. (the squares of the resonance frequencies have been normalized by the measurements at t=0).

According to Figure 4.4, both sample-A and sample-B have experienced an overall material stiffening over time, which is quantified by increase of resonance frequencies. There is a sharp stiffening in the first few hours (0-2 hours) that slows afterwards. Since, the samples were at vacuum and high temperature conditions, our attention was drawn to two different possible mechanisms of stiffening governed by hydrostatic pressure and temperature. Here we used the

following two-time constant exponential equation (Eq. 4.1) to fit the squared frequencies with time, in order to get a broader understanding of the dynamics of the material stiffening and their mechanisms. Figure 4.5 shows the quality of the fitting, and the fitted time constants, τ_1 and τ_2 for selected seven normal mode frequencies of Sample-A and Sample-B are tabulated in Table 4.2.

$$f_{(t)}^2 = f_0^2 + A_1\left(1 - e^{-\frac{t}{\tau_1}}\right) + A_2\left(1 - e^{-\frac{t}{\tau_2}}\right) \tag{4.1}$$

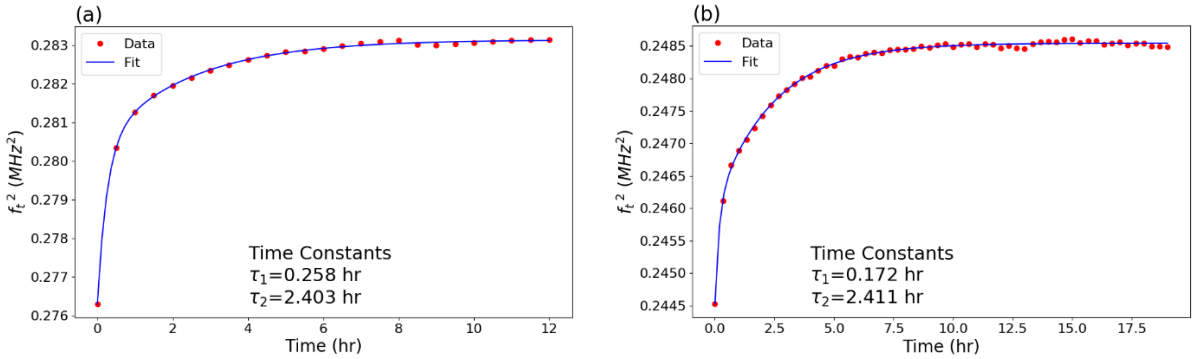

Figure 4.5. Curve fits to the frequency squared data of (a) Sample-A and (b) Sample-B.

Table 4.2. The time constants obtained from the exponential fit.

	Tube Sample A – at 498 K		**Tube Sample B – at 511 K**	
	τ_1 (hr)	τ_2 (hr)	τ_1 (hr)	τ_2 (hr)
Peak 1	0.277	3.690	0.186	2.525
Peak 2	0.255	3.323	0.176	2.411
Peak 3	0.258	2.403	0.181	1.984
Peak 4	0.241	2.944	0.166	1.776
Peak 5	0.263	3.318	0.173	2.028
Peak 6	0.257	3.674	0.153	1.566
Peak 7	0.279	4.191	0.136	0.621
Average	**0.261**	**3.363**	**0.167**	**1.844**

The curve fits provide two significantly different time constants τ_1 and τ_2, such that $\tau_2 = \sim 10\tau_1$ for both samples. This time constant data reveals that the overall stiffening is composed of a rapid stiffening with lower time constants (0.261 hr, 0.167 hr) and a slow stiffening with larger

time constants (3.363 hr, 1.844 hr). The rapid stiffening is possibly due to the purging of gas and liquid phases from the voids within the material structure as they are exposed to partial vacuum condition. As the sample is exposed to a moderately high temperature for longer time, it is possible to observe a partial annealing or microcrack healing processes which reduced the porosity, and hence increased the stiffness of the material. Since the microcrack healing is a slow process, we can conclude that the slower stiffening with larger time constant was due to the microcrack healing process. The material stiffness with increasing temperature and reducing hydrostatic pressure will be discussed in the following sections.

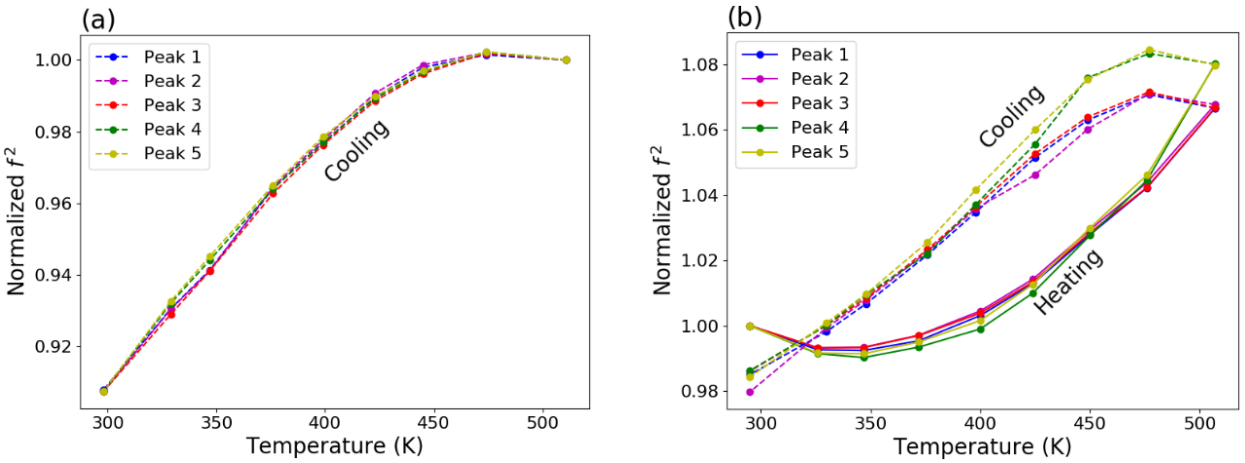

Figure 4.6. Frequency trends at the thermal cycles. (a) cooling process from 511 K to 295 K. (b) thermal cycle from 295 K to 507 K.

This porous material exhibits stiffening with increasing temperature. Stiffening during heating cycle and softening during cooling cycle was observed during multiple heating-cooling cycles. As the temperature increases, the microcrack healing will take place such that it will make the material stiffer. The observed microcrack healing is reversible and the healed microcracks are grown during the cooling process and make the material soft. This microcrack healing and growing has been reported in other experimental studies as well [74]. This observation confirms that the

slower stiffening observed above is due to the microcrack healing process at moderately high temperatures.

Figure 4.7 shows the hydrostatic pressure dependence of the normal mode frequencies and acoustic attenuation. The frequency trends exhibit a material stiffening with reducing hydrostatic pressure. This confirms that the rapid stiffening at 23 Torr (0.03 atm) with smaller time constant is possibly due to the gas removal process. However, this experiment should be developed with finer pressure variations so that we can acquire more data points. Chapter 5 will discuss the development of the experimental setup and the measurements.

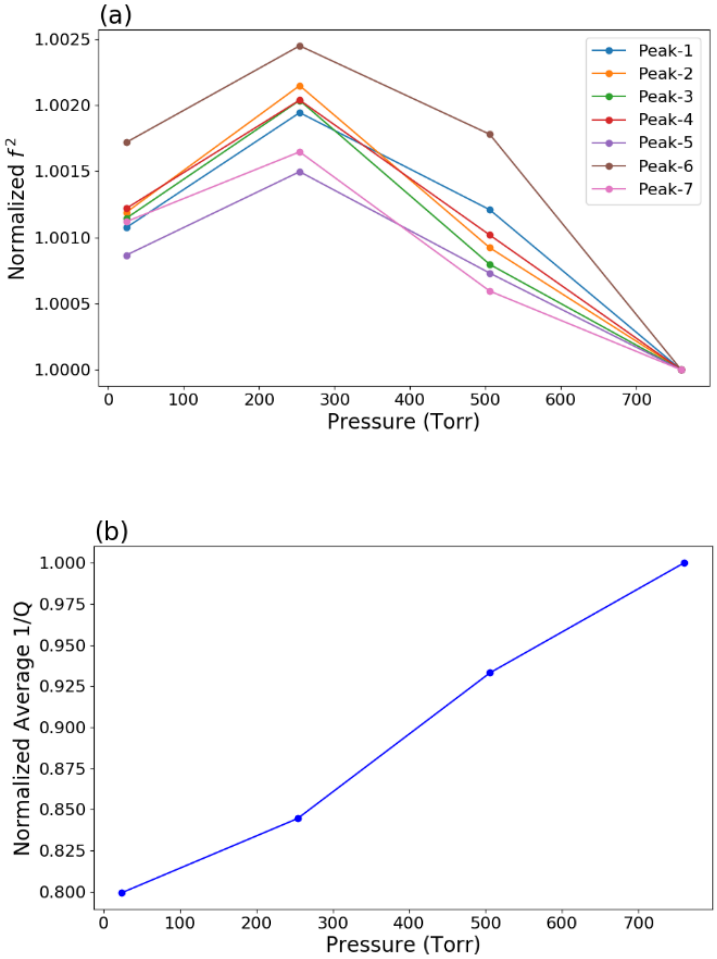

Figure 4.7. Pressure dependence of (a) resonance frequencies and (b) average 1/Q exhibited by sample-B at room temperature.

CHAPTER 5

HYDROSTATIC PRESSURE DEPENDENT ELASTICITY OF POROUS CERAMICS

The preliminary study discussed in Chapter 4 drew our attention to the observation of porous material stiffness at reduced hydrostatic pressure as it is the opposite of the typical fully dense solid materials. Therefore, this dissertation was primarily designed for a deep understanding of the influence of the pore saturated gas media and their physical properties on the elasticity of porous ceramic materials. This chapter will discuss the experimental findings of the hydrostatic pressure dependence of the elasticity of porous ceramics saturated with different gas media.

5.1 Materials

Commercially available porous alumina (Al_2O_3) (AdValue Technology), yttria partially stabilized porous zirconia (ZrO_2) /Y-TZP (IPS e.max ZirCAD; Ivoclar Vivadent North America, Amherst, NY, USA), and porous titania (TiO_2), whose membrane is a mixture of zirconia and titania (Sterlitech Corporation) were used in this study. High purity, precise porosities and pore sizes, and the material rigidity were considered when selecting these materials. The fully dense zirconia samples were prepared at Biomedical Materials Science Laboratory, University of Mississippi Medical Center (UMMC) from yttria partially stabilized zirconia/Y-TZP. Porous zirconia specimens were sintered to full density according to the following heating schedule in a furnace (Sintramat, Ivoclar Vivadent) at ambient pressure: room temperature to 1100 ºC for 1 h 12 min, 1100 to 1350 ºC for 1 h 11 min, 1350 to 1500 ºC for 30 min, held at 1500 ºC for 30 min,

and 1500 ºC to room temperature for 4 h 29 min. A type of fully dense ceramics used in LG solid oxide fuel cells was also used to compare the experimental results with porous ceramics. Rectangular parallelepiped shaped samples were cut from the bulk samples using a low speed diamond saw and they were polished by a water based lapping machine. The sample specifications are listed in Table 5.1. The porosity values of test samples were provided by the manufacturers and they were verified by the volumetric calculations.

Table 5.1. Material specifications.

Specification	**Porous Ceramics**			**Dense ceramics**	
	Al_2O_3	ZrO_2	TiO_2	ZrO_2	LG
Width (mm)	2.452	2.911	1.928	2.880	3.477
Length (mm)	3.890	3.213	3.585	3.814	3.822
Height (mm)	5.785	4.951	5.450	5.571	6.314
Density (gcm^{-3})	2.193	3.125	3.221	5.997	4.397
Porosity (%)	~ 40	~ 48	N/S	-	-

*N/S = not specified by the manufacturer.

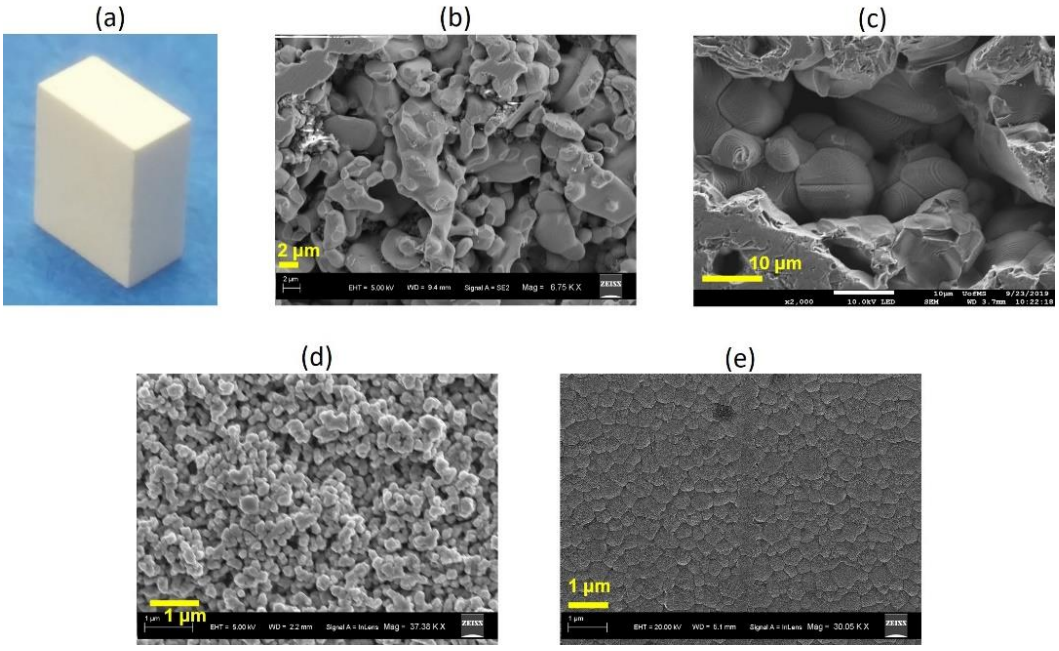

Figure 5.1. (a) Porous alumina test specimen and the SEM images of (b) porous alumina, (c) porous titania, (d) porous zirconia and (e) sintered zirconia.

5.2 RUS Setup

A direct contact transducer system made of two gold-coated lithium niobite ($LiNbO_3$) transducers was used to measure the resonance spectra. The sample-transducer system was placed inside a sealed high-pressure cell which is designed to fit inside a tube furnace (Carbolite Model MTF12/38/250) (Figure 5.2). The upper end of the tube is designed to fill the gas and the lower end is connected to a vacuum pump for gas removal process. At its maximum operation, the vacuum pump reduces the pressure inside the cell to 0.1 Torr. Both gas filling and removal are controlled by needle valves. A digital pressure gauge with the resolution of 0.1 Torr and a type N thermocouple with the resolution of 0.01 K were used to measure the hydrostatic pressure and the temperature inside the cell respectively.

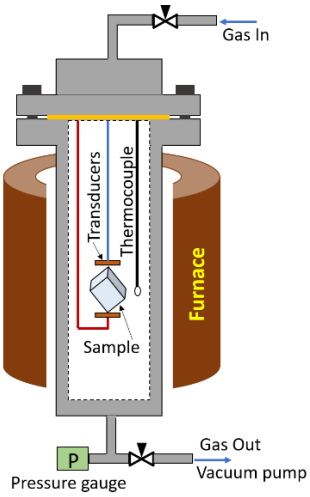

Figure 5.2. Experimental setup designed to perform the experiments in high- and low-pressure conditions.

5.3 Methodology of Data Analysis

Figure 5.3 shows a typical resonance spectrum (quadrature signal amplitude vs frequency) of porous alumina test specimen. The phase information of the quadrature signal results in

Lorentzian shaped resonance peaks with arbitrary phase. The inset shows a Lorentzian curve fitting for the resonance peak at 544 kHz which has an average quality factor of 628. The statistical fitting error of the center frequencies are ranged from 1.6 Hz – 8.7 Hz (average of 4.8 Hz, 9.7 ppm), implying the high precision of the RUS data acquisition.

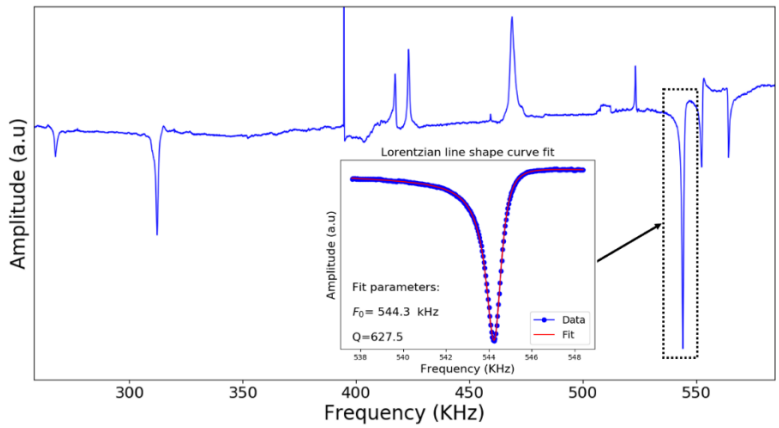

Figure 5.3. Resonance spectrum (quadrature signal vs frequency) of porous alumina test specimen. The Lorentzian curve fitting for peak at 544 kHz is shown in the inset.

Although we have discussed the 7×7 elastic tensor proposed by Biot's theory of poroelasticity, as a preliminary computation this study still uses the conventional 6×6 elastic tensor by assuming that porous ceramics behave as isotropic polycrystals. Then we recall the measured elastic constants as effective elastic constants and the derived elastic moduli are known as the *effective* elastic moduli. As discussed in Chapter 2, isotropic polycrystalline solids exhibit only two independent elastic constants, $C_{11}$and C_{44} in their elastic stiffness tensor. The acquired normal mode frequencies and geometrical data of the test specimens were used to compute the elastic constants using Levenberg-Marquardt nonlinear fitting algorithm. The average error magnitude of measured and calculated resonance frequencies at the optimization iterations was 0.5%, indicating a reasonable fit for the elastic constants. Shear modulus, *G* and Young's modulus,

E were calculated using the measured elastic constants (Eqs. 2.36 and 2.37). In some experimental studies, especially in high pressure conditions, the test specimens exhibited acoustic damping which results in fewer number of detectable resonance peaks in the spectrum. Therefore, the change in elasticity has been qualitatively studied by analyzing the change in resonance frequencies instead of calculating elastic constants. the experimental procedures, results and discussions of several studies are described in the following Section 5.4.

5.4 Experimental Procedures, Results and Discussions

5.4.1 Elasticity of Porous Alumina and Zirconia at Low-Pressure Regions

Alumina sample was placed inside the test cell filled with lab air at ambient pressure 760 Torr (1 atm) and temperature 295 K. Vacuum pump was used to remove the gas inside the cell, and hence to reduce the hydrostatic pressure. A needle valve was used to control the gas vent and the pressure inside the cell. Resonance spectra were acquired at several pressure points during the pressure cycles from 760 – 0.1 Torr. The above procedure was followed with the porous zirconia sample.

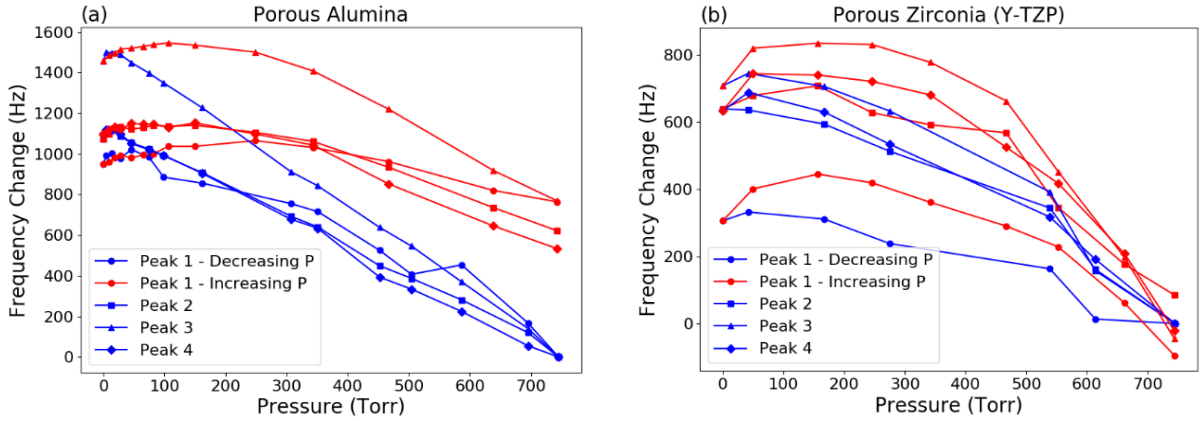

Figure 5.4. Frequency change of normal modes during the pressure cycles (a) porous alumina (b) porous zirconia. Blue / red symbols indicate decreasing / increasing pressure respectively.

According to the resonance frequency trends shown in Figure 5.4, both porous alumina and zirconia samples follow an overall material stiffening during the gas removal process. To confirm the validation of the above result, multiple tests were performed with the alumina sample, and the resultant normal mode frequencies were used to compute the polycrystalline elastic constant $C_{11}$and C_{44}. Pressure dependent Young's and shear moduli are shown in Figure 5.5.

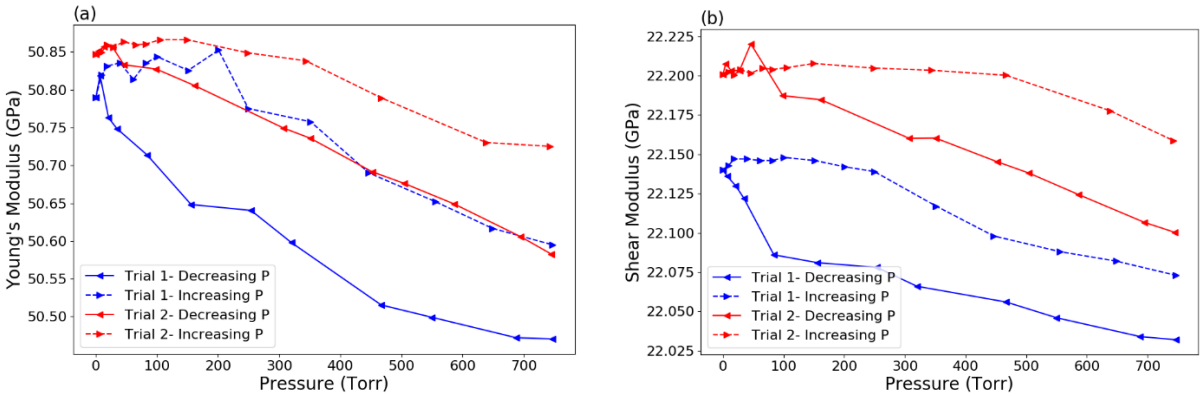

Figure 5.5. Variation of elastic moduli: (a) Young's modulus and (b) Shear modulus, of the porous alumina during the pressure cycles.

Multiple RUS measurements and the corresponding elastic moduli trends have concluded the validation of the porous material stiffening during the gas removal process. The thermodynamic temperature drop due to the pressure decrease from 760 Torr to 0.1 Torr was measured as 0.6 K and ~0.008 % increase of shear modulus is estimated due to this temperature reduction, while a ~0.5 % increase of shear modulus was observed in the experimental results. This implies that the observed material stiffening is dominated by the micromechanical structural process induced by gas removal.

5.4.2. Comparison of Pressure Dependent Elasticity of Porous and Dense Zirconia

This experiment was conducted to compare the pressure dependent resonance frequency trend of fully dense zirconia with that of porous zirconia. The resonance spectra of both porous and fully dense zirconia were measured during multiple trials of pressure cycles from 760 – 0.1 Torr. The average of selected normal mode frequencies at each trial of each specimen are shown in Figure 5.6. The frequency trends provide a clear comparison between the porous and fully dense specimens. Here, as expected, the fully dense specimen shows a slight stiffening with increased pressure with no hysteresis, whereas the porous specimen follows a rapid softening in the same pressure range confirming the previous results in Section 5.4.1

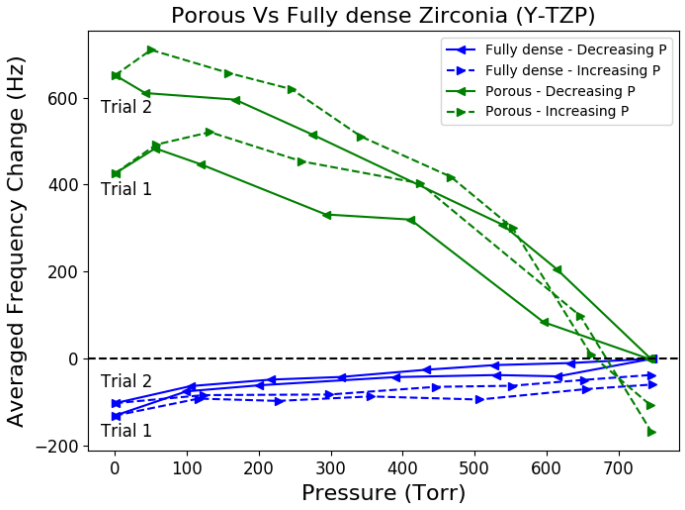

Figure 5.6. Averaged frequency change over the selected normal modes of porous and fully dense zirconia at multiple trials of pressure cycles.

5.4.3 Elasticity of Porous Alumina and Dense Zirconia at High-Pressure Region

Although the above experiments were designed to study the low-pressure dependent elastic behavior of porous materials, the operated pressure range was narrow (760 – 0.1 Torr). We observed slight changes (~0.5%) of materials elasticity over the limited pressure range. The

consistency of the experimental results observed above motivated to conduct experiments in a higher and broader pressure regime. In this experiment both porous alumina and dense zirconia samples were used to study the high-pressure dependent elasticity. Initially, a porous alumina sample was placed inside the cell at room temperature and ambient pressure. Then the pressure was decreased to 0.02 psi (1 Torr). Argon gas was supplied to the cell to increase the pressure and the resonance spectra were measured at several pressure points from 0.02 - 800 psi. The upper pressure point was limited to 800 psi as the signal amplitude and the quality of the resonance peaks have been reduced likely due energy loss through acoustic radiation near the resonance. The energy dissipation was reversible, and an amplitude rise was observed during the decreasing pressure cycle. The reversibility of the change of signal amplitude is shown in Figure 5.7 and the energy dissipation mechanisms will be discussed along with the quality factor data acquired from resonance spectra. The same procedure was followed with the dense zirconia test specimen and measurements were taken up to 500 psi.

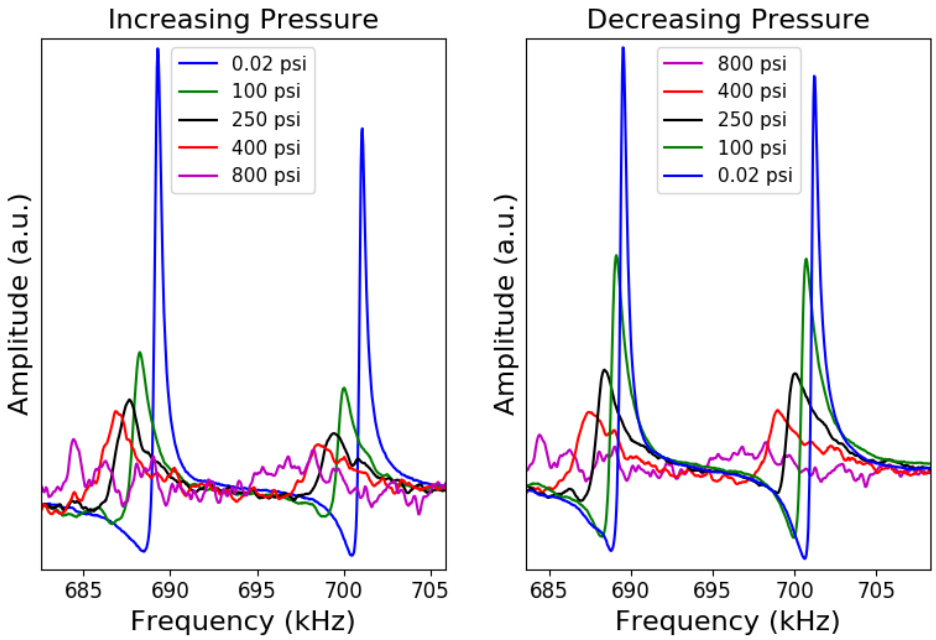

Figure 5.7. The signal amplitude changes and their reversibility during the pressure cycles.

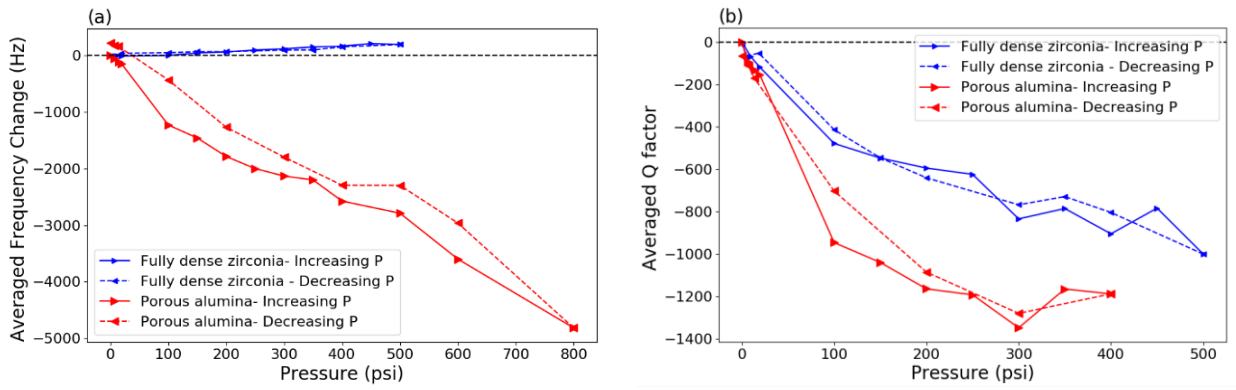

Figure 5.8. The pressure dependence of (a) averaged frequency change and (b) averaged Q factor change of selected normal modes of porous alumina and dense zirconia during the high-pressure cycles. (changes were calculated from the values at 0.02 psi).

The observed frequency trends of porous alumina and dense zirconia emphasize the same trends observed in low pressure region. Porous alumina has shown a rapid softening with increasing pressure, while dense zirconia is following a slight stiffening. Taken as a whole, these results provide strong evidence that porous materials become stiffer with decreasing hydrostatic pressure over broad pressure ranges.

The quality factor (Q) is a measure of the inverse of the energy dissipation of an elastic solid near the resonance and defined as the ratio of the total energy to the energy lost per cycle. For a given resonance peak in the resonance spectra, quality factor can be determined as: $Q = f_0/\Delta f$, where f_0 is the center frequency of the resonance and Δf is the full width at half maximum (FWHM). According to the measured Q factor data of both porous and dense specimens, Q factors of selected resonance peaks decrease with increasing hydrostatic pressure and the trend is reversible with the pressure cycles (Figure 5.8(b)). This reduction of the quality factor is a measure of the elastic energy dissipation of both porous and full dense solids. At resonance, a solid body vibrates with the maximum amplitude and its surfaces will create vibrations on the gas medium by transferring the vibrational energy into the gas medium (acoustic radiation). The energy

transmission at the solid - gas interface is enhanced with the increase of gas pressure since it will make the gas denser, and hence reduce the impedance mismatch between the media. This energy dissipation mechanism reduces the detectable vibrational amplitude of the resonance peaks as shown in Figure 5.7. With compared to fully dense zirconia, porous alumina sample shows a rapid decrease of Q factor with the increased pressure. This observation is possibly due to the additional energy dissipation takes place at the solid-pore interfaces.

Computing elastic constants of porous alumina at higher pressures was difficult due to lack of measurable normal mode frequencies. However, reasonable number of resonance frequencies were able to detect up to 300 psi pressure point, and hence the pressure dependent elastic constants were determined in the 0.02 – 300 psi pressure region. Figure 5.9 illustrates the variation of elastic constants and the Young's modulus with the increased hydrostatic pressure. C_{11} and Young's modulus which correspond to the extensional modes have shown a rapid decrease with the increasing pressure while the shear mode C_{44} has followed a slow decrease. This suggests that the applied hydrostatic pressure provides a larger impact on the extensional vibrational modes than the shear modes indicating that the extensional elastic constants are changed significantly with the change of hydrostatic pressure. According to the Biot's theory, the stress tensor has modified by adding the hydrostatic stress term, $\sigma_f = -\phi p$ as described in equations 2.11 and 2.12, and the effective stress components are given by $\sigma'_{ii} = \sigma_{ii} - \phi p$ for $i = 1, 2, 3$. The hydrostatic stress acts only on the extensional stresses σ_{xx}, σ_{yy} and σ_{zz}, and the shear stress components are not altered by the hydrostatic stress. According to the constitutive relations derived in Section 2.2.1, for an isotropic polycrystal class the extensional elastic constant, *P* and the shear elastic constant, *N* are expressed by the equations 2.30 and 2.32 as follows.

$$P = 2G + 2G\left(\frac{\nu}{1-2\nu}\right) + BK_u\frac{(\alpha-\phi)^2}{\alpha} \tag{2.30}$$

$$N = 2G \tag{2.32}$$

The equations clearly demonstrate that the extensional elastic constant involves with both solid and fluid elastic moduli while the shear elastic constant contains only the solid elastic moduli. This implies that the extensional modes are directly coupled with the fluid phase, and hence they are affected significantly by the hydrostatic pressure as illustrated by the experimental results discussed above.

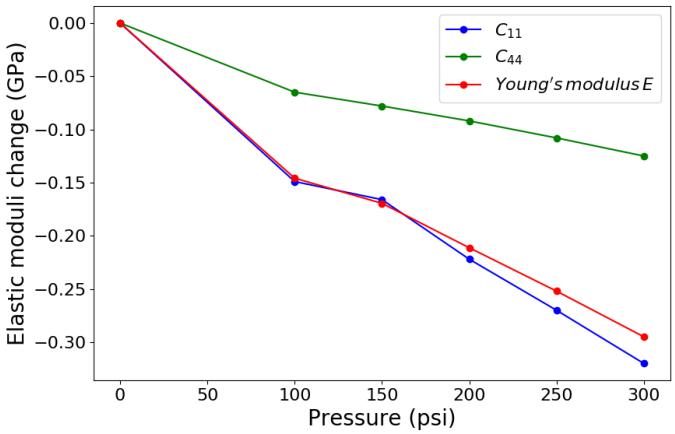

Figure 5.9. Pressure dependent elastic constants and Young's modulus of porous alumina pressurized by argon gas.

5.4.4 The Effect of the Saturated Gas Medium

After observing the above behavior of the elasticity with hydrostatic pressure saturated by argon gas, attention was drawn to repeat the experiment with different gas types to study the effects of the fluid properties on the materials elasticity. Both fully dense and porous ceramics samples were used in this study, and helium, nitrogen and argon gas were used for the saturation. The

frequency changes with hydrostatic pressure of each materials with different gas media are illustrated in Figure 5.10. As shown in Figure 5.10(a) and (b), both fully dense ceramics exhibit an increase of material stiffness with increasing pressure. The stiffening rate is nearly constant for each gas saturation. This implies that the fully dense material stiffening is caused due to the increase of the curvature of the interatomic potential energy curve by reducing the lattice constants with increasing hydrostatic pressure and it will not be affected by the type of the saturated gas.

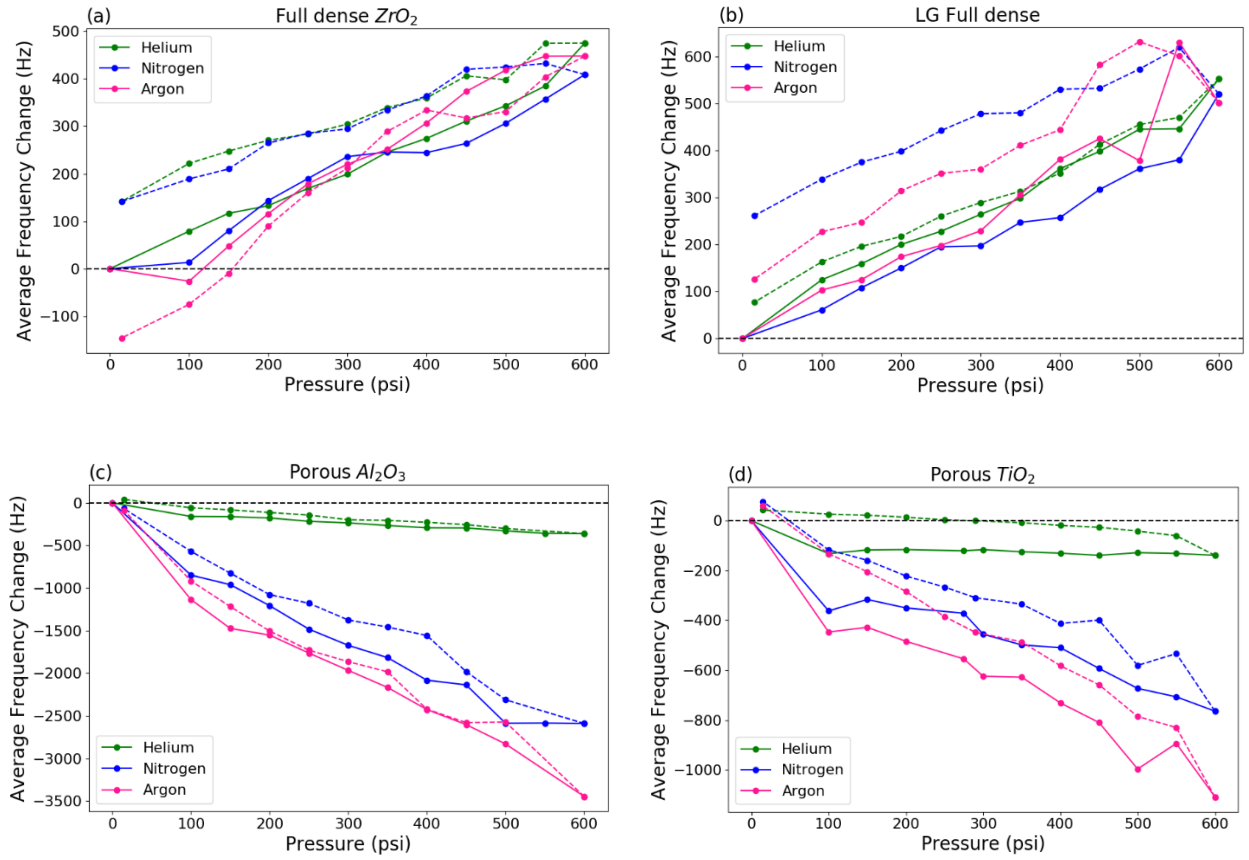

Figure 5.10. Pressure dependent frequency change of (a) fully dense zirconia (b) fully dense LG ceramics (c) porous alumina and (d) porous titania with the helium, nitrogen and argon gas saturation.

However, porous ceramics have shown a clear variation in the rate of change of resonance frequencies with the hydrostatic pressure at different gas saturation (Figures 5.10(c) and (d)). Helium gas saturation follows a slight variation of the resonance frequencies while nitrogen and

argon lead to a significant variation. This implies that the saturated gas type is one of the factors which determines the rate of porous materials' elasticity change with the hydrostatic pressure. Density, molecular weight and viscosity are the main physical properties of the gas medium which can directly affect to this variation. In order to study the relation between the atomic wight and the rate of the frequency variation, the frequency changes data of porous alumina at both increasing and decreasing pressure cycles were fitted to a linear function and the slopes, $\Delta f/\Delta p$ were determined for each gas type (Figures 5.11(a) and (b)).

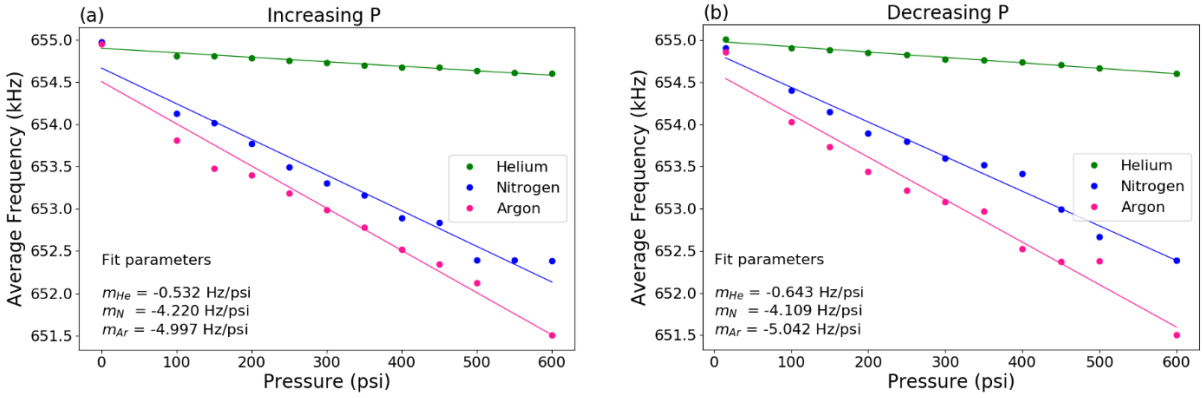

Figure 5.11. Linear fits for the frequency variations of porous alumina at (a) increasing and (b) decreasing hydrostatic pressure cycles.

The magnitudes of measured slopes were then analyzed with the molecular weight of the gases. The variation of the slope with the molecular weight (*M*), which is not linear, is shown in Figure 5.12(a). In a previous study, Isaak et al. have reported that the pressure derivative of the shear modulus measured form fused silica is proportional to the square root of the atomic weight such that, $\left|\frac{\partial G}{\partial p}\right| \propto \sqrt{M}$ [75]. Since resonance frequency, f is proportional to the square root of the elastic modulus ($f \propto \sqrt{G}$), Isaak's finding suggests that the pressure derivative of the resonance frequency is directly proportional to the *M* to the power of one forth such that, $\left|\frac{\Delta f}{\Delta p}\right| \propto M^{1/4}$. The

linear relationship between the measured slopes, $\left|\frac{\Delta f}{\Delta p}\right|$ with $M^{1/4}$ has been verified by our measurements as shown in Figure 5.12(b), confirming the validation of the Isaak's findings.

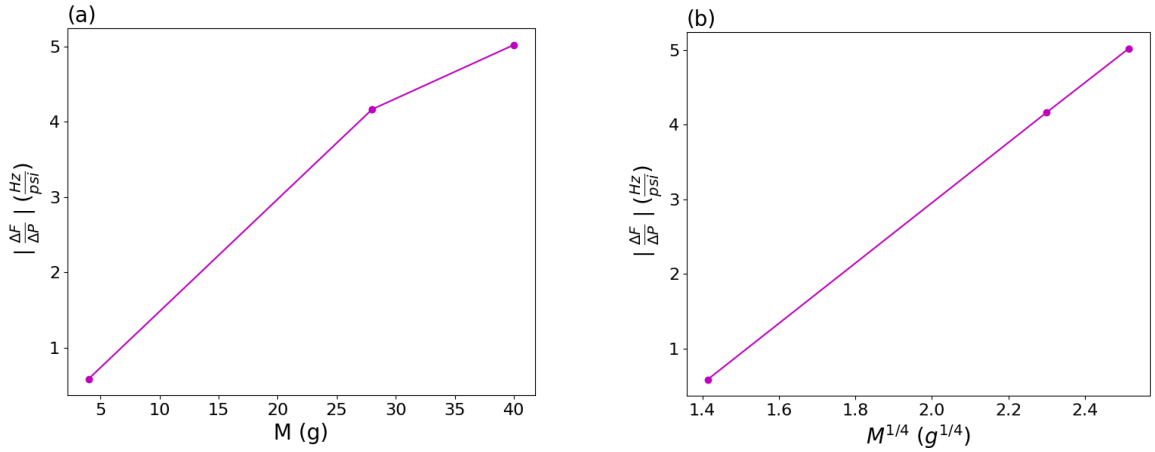

Figure 5.12. The plots of (a) $\left|\frac{\Delta f}{\Delta p}\right|$ $Vs\ M$ and (b) $\left|\frac{\Delta f}{\Delta p}\right|$ $Vs\ M^{1/4}$.

5.5 Conclusions

The main objective of this experimental study was to investigate the hydrostatic pressure dependnet elasticity of porous cermaics and its behaviour with the properties of saturated gas. A series of RUS measuremnts were conducted and the measured pressure dependent resonnace frequency trends and calculated elastic moduli have confirmed the reversible porous material softning (stiffening) with increased (decreased) hydrostatic pressure over the range of 0.02 – 800 psi. A clear distinct trend of pressure dependent elasticity exhibited by the the fully dense ceramics reveals that the elasticity change of the porous material is possibly due to the pore structure and micromachanical effects such as microcrack growth and healing induced by applied hydrostatic pressure. This experimental results validates the Biot's theory of poroelasticity wich describes the pressure dependency of the elasticity of porous materials. The effect of saturated gas type on the

rate of change of elasticity with the pressure was examined and the behaviour of the pressure derivaties with the molecular weight was descussed.

CHAPTER 6

MECHANICAL AND STRUCTURAL STABILITY OF POROUS ALUMINA AT HIGH TEMPERATURES

6.1 Introduction

The following experiments were designed and performed to study the stability of the elasticity (mechanical equilibrium) of the porous material at moderately high temperatures and different pressure points. Initially, the alumina sample was under the argon gas saturation at 760 Torr and 295 K. Temperature inside the cell was increased to 423 K and pressure raised to 840 Torr at the steady temperature of 423 K. After the steady state of temperature and pressure reached, pressure was reduced to 0.1 Torr, and resonance spectra were measured at every 15 minutes for 70 hours. After 70 hours, pressure was raised to 420 Torr by filling argon gas, and resonance spectra were measured. The same procedure was followed to 840 Torr pressure point. Another time evolution experiment was performed by measuring resonance spectra at 840 Torr, 540 Torr and 260 Torr pressure points through the decreasing pressure process at 423 K. The temperature was maintained at 423 +/- 1 K throughout the whole experiment. Argon gas was used in this experiment to prevent from any oxidation processes which will take place at high temperatures.

6.2 Results and Discussion

The time evolution of elastic moduli during both increasing and decreasing pressure cycles are represented in following Figures 6.1 and 6.2.

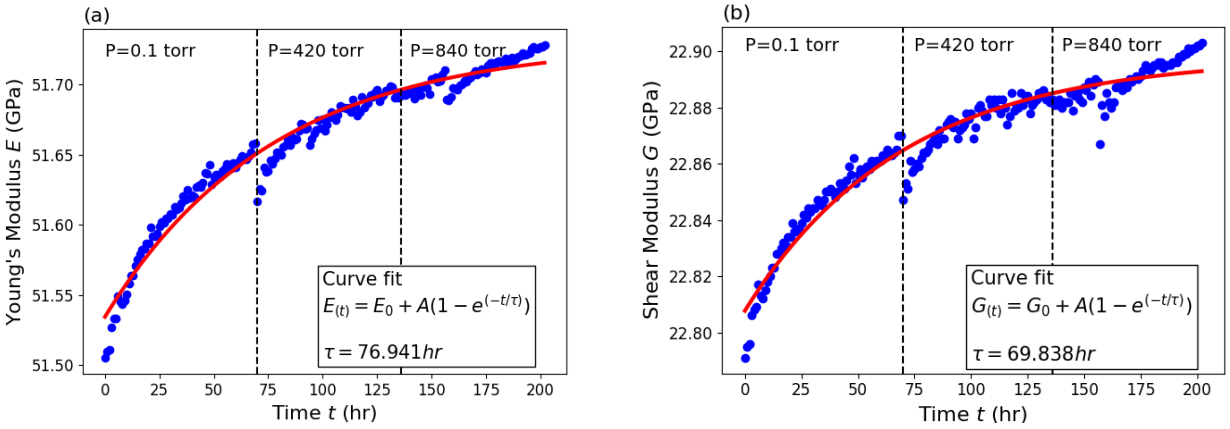

Figure 6.1. Time evolution of (a) Young's modulus and (b) shear modulus during the increasing pressure process at 423 K.

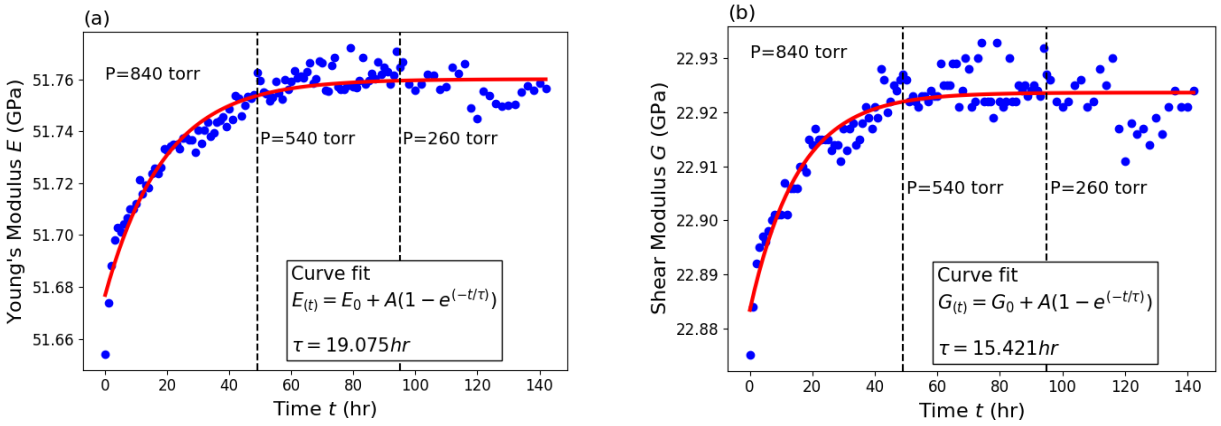

Figure 6.2. Time evolution of (a) Young's modulus and (b) shear modulus during the decreasing pressure process at 423 K.

The elastic moduli exhibit an overall exponential growth with time during both increasing and decreasing pressure cycles. Although the changes of elastic moduli are very small (< 0.5 %), they show a best fit with the exponential growth function, indicating the precision and sensitivity of RUS measurements. The sudden drop / rise of elastic moduli at changing pressure events are

comparable to the material softening / stiffening behavior observed in the experiments described in Chapter 5. Despite that, the material has followed an overall stiffening process during both pressure cycles at 423 K. This implies that the stiffening was mainly dominated by the temperature increment rather than the gas removal. The temperature dependent material stiffening process is possibly explained by the porosity reduction at the partial sintering processes such as neck growth, grain boundary growth and microcrack healing [74,76]. A direct conclusion to the above stiffening nature has been limited due to the practical limitation of porosity measurement or any other structural change measurement at the experiment environment. However, RUS is well equipped to probe the elasticity change more precisely. Therefore, mathematical models of porosity dependent elasticity can be used to explore the porosity changes based on the elastic moduli obtained from the RUS measurements.

Two mathematical models: model-1 (Eq. 6.1) [77] and model-2 (Eq. 6.2) [78] , of porosity, ϕ dependent Young's modulus, E were considered to compute the porosity change.

$$E = E_0 e^{(-b_E \phi)} \tag{6.1}$$

$$E = E_0 (1 - \phi)^n \tag{6.2}$$

Where E_0 is the Young's modulus of fully dense material (at zero porosity) and b_E, n are the empirical parameters which are to be determined by experimental studies. Ren et al. [50] have reported $b_E = 3.4 \pm 0.1$ for alumina based on their experimental studies of porosity dependent elasticity and Munro [47] has used several experimentally reported data to derive the value of n to be 3.06 for alumina. Here we have estimated the porosity change with the time at 0.1 Torr and 423 K by using the Young's modulus data in to the above two models.

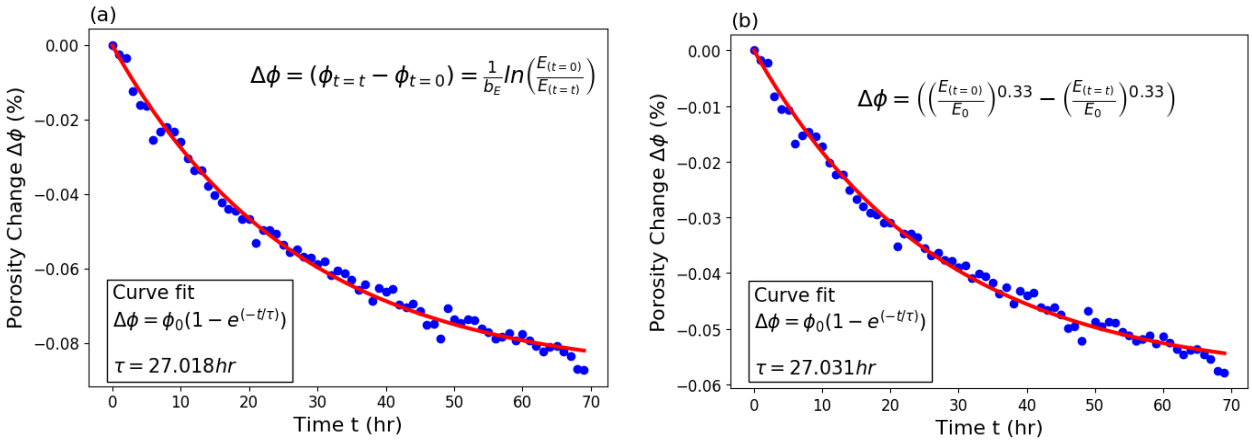

Figure 6.3. Estimated variation of porosity with time at 0.1 torr and 423 K, based on (a) model-1 and (b) model-2.

The estimations from both models represent a porosity reduction of the material over time. The reduction is well fitted to the exponential decay function with time constant τ = 27 hr. This time constant refers to the rate of the partial sintering process where the surface free energy got minimized. Despite the fact that our experimental temperature of 423 K is much lower than the sintering temperature of alumina (> 1500 K), there is a possibility to observe some partial sintering effects at slower rates. Here, model-1 has estimated 0.09 % reduction of porosity, while it is 0.06 % from the model-2. This deviation is possibly due to the choice of empirical parameters and initial conditions of Young's modulus at 150 ℃. This estimation of porosity reduction strongly suggests the partial sintering process of the material, and hence the overall material stiffening with the time.

6.3 Conclusions

Overall material stiffening with the time was observed at 423 K during both increasing and decreasing pressure cycles from 840 – 0.1 Torr. Although the magnitude of stiffening is low (<

0.5 %), it follows a well fitted exponential growth with the time. This material stiffening at elevated temperature is possibly due to the partial sintering process followed by a porosity reduction. The porosity reduction was estimated by applying the measured Youngs' modulus data in to two well-known models of porosity dependent Young's modulus. This study demonstrates the capability of RUS in measuring more sensitively changes of elasticity with higher precision.

CHAPTER 7

TEMPERATURE DEPENDENT ELASTICITY OF SINGLE CRYSTALLINE TIN SELENIDE

7.1 Introduction

In recent years, single crystalline tin selenide (SnSe) has attracted enormous attention due to its record high thermoelectric (TE) figure-of-merit or ZT ~2.6 at T > 900 K arising from its significantly low thermal conductivity κ. Pristine SnSe exhibits a low thermal conductivity despite its simple layered crystal structure, orthorhombic *Pnma* phase that undergoes a displacive phase transition (Tc ~ 810 K) to the *Cmcm* phase with increasing temperature (Figure 7.1). Recent experimental and theoretical works on SnSe have revealed that this intrinsically low thermal conductivity is driven by strong lattice anharmonicity of its crystal structure, which is tied to a lattice instability arising from the structural phase transition. The elastic energy density corresponding to the potential energy, U is a quadratic function of the elastic strains ε_{kl}, and hence probing temperature-dependent elastic moduli is important to fully understand the phonon anharmonicity of materials. Furthermore, although the TE properties of SnSe have been widely investigated, the implementation of a TE device requires materials with high mechanical strength that can withstand thermal cycling at high temperatures. These findings motivate the current researchers to explore the elastic properties of SnSe at higher temperatures (300-1000 K), for a deeper understanding of the contribution due to phonon anharmonicity on its thermal transport and mechanical properties.

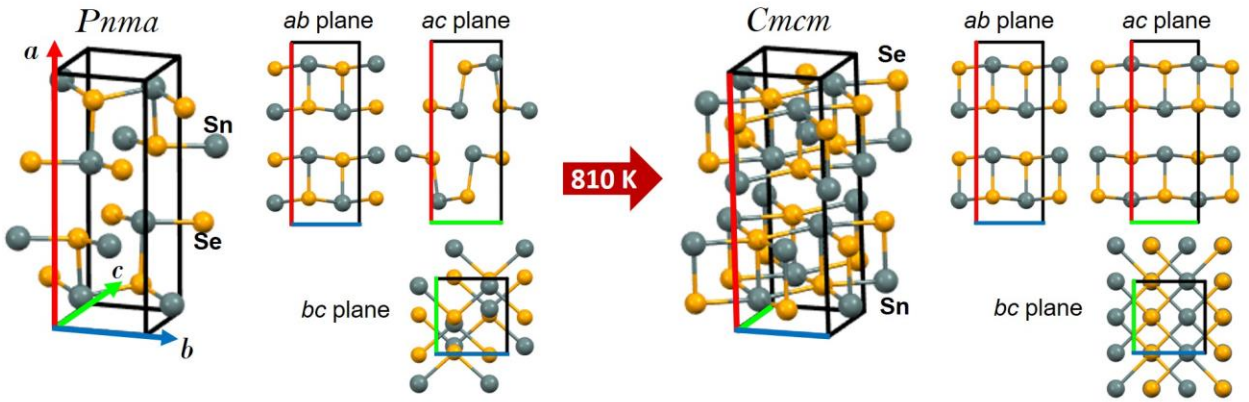

Figure 7.1. Crystal structures of the *Pnma* and *Cmcm* phases of SnSe below and above the phase transition at 810 K. The *Pnma* and *Cmcm* phases of the different crystallographic planes are also shown on the left and right sides of the arrow indicating the phase transition. Here, *a*, *b*, and *c* are the primary crystallographic directions of SnSe in the *Pnma* and *Cmcm* phases.

In contrast to an isotropic polycrystal which has only two elastic constants, the orthorhombic crystal structure of SnSe owns nine independent anisotropic elastic constants in its elastic stiffness tensor C_{ij} that has been estimated using *ab initio* density functional theory (DFT). However, it is well known in the RUS community that an experimental investigation of the nine independent elastic constants is challenging, especially in high temperatures. This chapter discusses the use novel resonant ultrasound spectroscopic (RUS) measurements to measure the temperature dependence of the complete elastic tensor of single crystalline SnSe, and to detect the phase transition by the mean of elastic parameters. This study provides a broad description of the use of elastic tensor to compute anisotropic elastic and thermal properties of low symmetric crystalline materials.

7.2 Materials and Methods

7.2.1 Sample Preparation

High quality single crystalline SnSe samples (packing density > 99% of the theoretical density) were synthesized by the Bridgman method at the Institute of Physics, Academia Sinica in Taiwan, and the details of the procedure are described elsewhere [69]. Typical dimensions of SnSe crystals used in this study were 2.024 x 3.531 x 4.775 mm^3 (± 0.001 mm) and their average density was 6.031 g cm^{-3} (~100% of the theoretical density).

7.2.2 RUS Measurements and Computation

Resonance spectra of the sample at elevated temperatures from 295 K – 773 K were measured using a direct contact transducer system made with $LiNbO_3$ piezoelectric transducers, (Figure 7.2(a)) placed inside a sealed glass tube which is housed in a tube furnace. The resonance frequencies acquired from measured RUS spectra, geometrical data and theoretically reported elastic constants from DFT [71] were used to optimally determine the nine elastic constants of the crystal. The fitting routine is inherently non-linear and uses a classic Levenberg-Marquardt algorithm. In any non-linear optimization problem, care must be taken that the algorithm settles on the global, rather than the local, minimum. The change of a natural frequency with respect to a change in each of the elastic constants ($\partial f_k / \partial C_{ij}$) varies significantly. Thus, the nine elastic constants were set into groups of three to vary (or "float") in each fitting routine. The most significant (largest derivatives) elastic constants C_{44},C_{55},C_{66} were varied first, followed with varying the next group of C_{11},C_{22},C_{33}, until the final group of C_{12},C_{13},C_{23} was varied. In this way, we "guide" the fitting algorithm to prevent weakly coupled elastic constants from varying

dramatically. The elastic constants from DFT were used as initial parameters in the fitting routine, however in order to guard against the local minimum problem, these initial parameters were randomly varied such that their standard deviations were within ±5% for 10 different fitting routines.

For an anisotropic crystal, the elastic moduli are different along each crystal axis. The Voigt-Reuss-Hill (VRH) approximation is often used to convert the anisotropic single crystalline elastic constants into isotropic polycrystalline elastic moduli, bulk modulus (*B*) and shear modulus (*G*) as discussed in Section 2.4. Furthermore, the VRH derived polycrystalline elastic moduli were used to compute the wave velocities, shear anisotropic factors, Grüneisen parameter and Debye temperature.

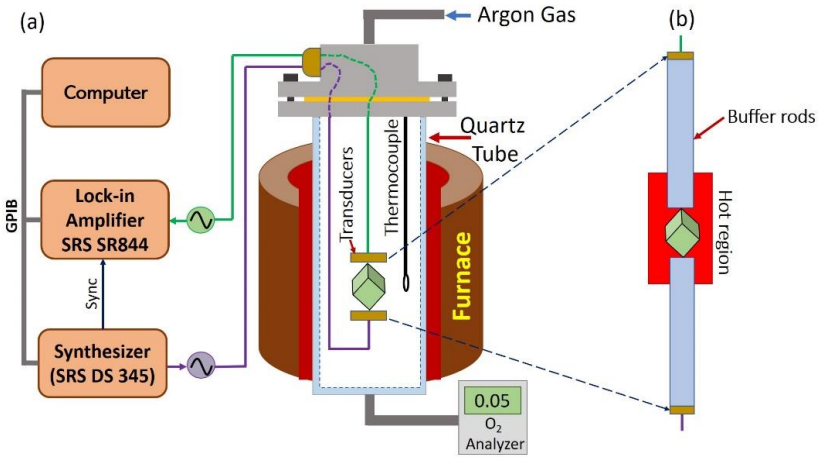

Figure 7.2**.** (a) RUS experimental setup with direct contact transducer system with $LiNbO_3$ piezoelectric transducers for measurements up to ~800 K and (b) buffer rod transducer system for measurements up to 1200 K.

Due to the limitation of maximum operating temperature of the direct contact transducer system, typically ~800 K for $LiNbO_3$, a buffer rod transducer system (Figure 7.2(b)) was used to measure resonance spectra up to 953 K in order to detect the change in elastic constants across T_c. Due to the acoustical losses through the long buffer rods, all resonance peaks were not observed

in measured spectra. Therefore, instead of computing elastic constants, trends in the temperature dependent resonance frequencies were used as indicators for T_c. It should be mentioned that all high temperature data were collected under flowing argon gas (low oxygen environment) to prevent the samples from oxidation.

7.3 Results and Discussions

7.3.1 Room Temperature Elastic Constants and Derived Elastic Properties

Resonance spectrum measured at room temperature (295 K) (quadrature signal amplitude *vs.* frequency) for SnSe is shown in Figure 7.3. Note phase information is included in this signal which results in Lorentzian peaks with arbitrary phase. The insert shows an example of a Lorentzian fit for the 321.8 kHz peak which exhibits an average quality factor of 400. Extending similar fits to other peaks in the resonance spectrum, the nine elastic constants (C_{ij}) were determined and they are listed in Table 7.1.

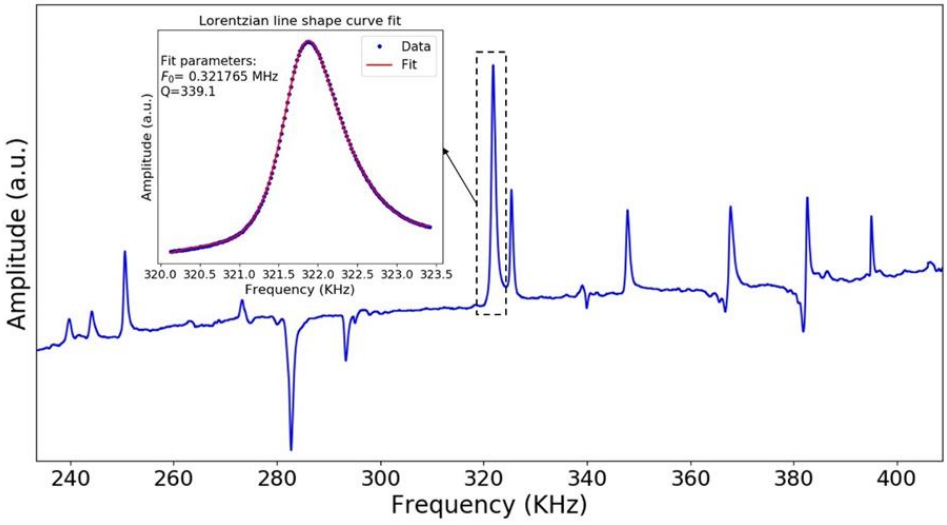

Figure 7.3. RUS resonance spectrum (quadrature signal amplitude *vs.* frequency) of SnSe sample at room temperature between 230 kHz and 410 kHz. The insert shows the Lorentzian line shape curve fit of a selected peak at 321.8 kHz.

Table 7.1. The elastic constants (C_{ij}) obtained from RUS measurements compared with DFT values [71], and their statistical deviations.

Elastic Constants	RUS Results		DFT Results (GPa)	% Difference (RUS & DFT)
	Mean (GPa)	% St. Dev.		
C_{11}	41.8	1	41.1	2
C_{22}	59.7	3	65.7	10
C_{33}	32.4	5	29.6	9
C_{44}	13.2	19	12.0	10
C_{55}	24.5	27	29.6	19
C_{66}	20.5	9	14.7	33
C_{12}	3.15	35	7.33	80
C_{13}	10.7	11	12.1	12
C_{23}	26.8	4	26.9	0
$C_{11} + C_{22} - 2C_{12}$	95.1	3	92.1	3
$C_{11} + C_{33} - 2C_{13}$	52.8	6	46.5	13
$C_{22} + C_{33} - 2C_{23}$	38.6	2	41.5	7

The experimentally obtained elastic constants (C_{ij}) are found to be in good agreement (within ~33%) with the theoretical values reported from DFT except for C_{12}. With the limitations and constraints of DFT, it is not feasible to calculate C_{12}, C_{13}, C_{23} directly from a single distortion. Instead, they can be extrapolated from other elastic constants. It is therefore more reasonable to compare the superposition of elastic constants rather than individual ones. The elastic constants obtained using the superposition method are in better agreement (within ~13%) with the calculated values. Thus, it may be safe to conclude that the elastic constants obtained from RUS measurements agree well with the computed values. Standard sources of uncertainty in RUS are imperfections in geometry, and, errors in alignment of crystal axes and sample body axes. The uncertainty in the extensional (longitudinal) moduli (C_{11}, C_{22}, C_{33}) derived from our RUS measurements were found to be ~0.5-1.0% and that in the shear moduli (C_{44}, C_{55}, C_{66}) were found to be ~0.02-0.5%. The estimation of these uncertainties are discussed elsewhere [17]. The

uncertainties in the off-diagonal elements (C_{12}, C_{13}, C_{23}) are more difficult to determine as they are weakly coupled to the natural frequencies.

A complete description of the elastic anisotropy of SnSe can be viewed by graphical surface representation of the directional dependent Young's modulus (Eq. 2.43) and bulk modulus (Eq. 2.44) as shown in Figure 7.4. The subplots represent the elastic anisotropy in the *ab*, *ac* and *bc* crystallographic planes of SnSe as a measure of the anisotropy in the bulk and Young's moduli. A quantitative measure of elastic anisotropy is given by the calculated axial bulk moduli, axial anisotropy factors and shear anisotropic factors listed in Table 7.2.

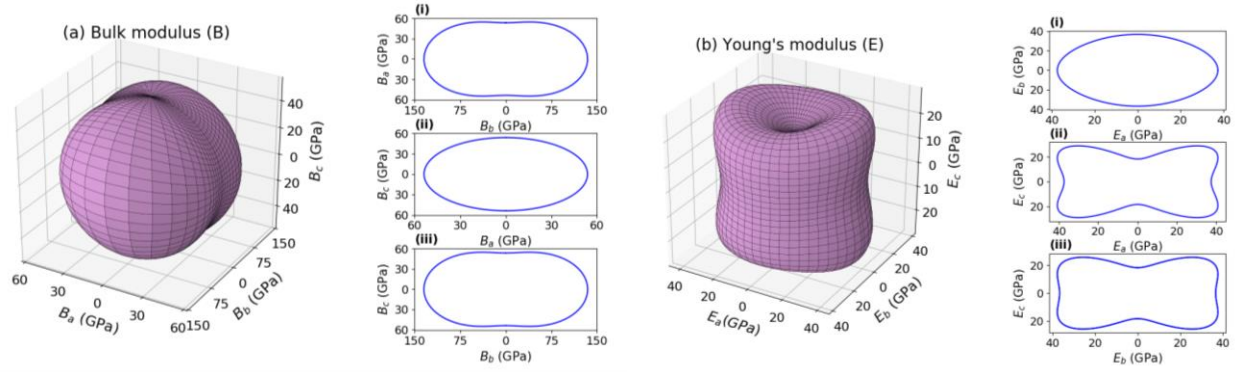

Figure 7.4. (a) The orientation dependent bulk modulus (B) and (b) Young's modulus (E) of single crystalline SnSe across (i) *ab*, (ii) *ac*, and (iii) *bc* crystallographic planes.

Table 7.2. Axial bulk moduli and elastic anisotropy factors calculated using the elastic constants from RUS and DFT.

Method	**Axial Bulk Modulus (GPa)**			**Axial Anisotropy**		**Shear Anisotropy Factor**		
	B_a	B_b	B_c	A_a	A_c	A_1	A_2	A_3
RUS	53.7	135	53.8	0.40	0.40	1.00	2.55	0.86
DFT	59.8	270	42.4	0.22	0.16	1.03	2.85	0.64

Based on the axial bulk moduli values in Table 7.2, specifically from the higher value of B_b compared to B_a and B_c we can conclude that the compressibility along the *b*- axis is much less than that of along the *a*- and *c*- directions, which are of similar magnitudes. In recent studies of Liu et al. [73], the highest strain stiffness was reported to be along the *b*- direction and the lowest strain stiffness along the *c*- direction, which confirms our highest value of B_b obtained from RUS measurements and subsequent DFT [71]. In addition, the lower compressibility of SnSe along its *b*- axis was reported in a previous study by Loa et al. [79]. under high pressure conditions. Not surprisingly, SnSe was reported to be most compressible along its *c*- direction under low pressure conditions, in agreement with the lowest B_c value ~42.4 GPa [71]. This pressure dependent compressibility behavior along the *c*- direction is similar to the reported negative thermal expansion behavior of SnSe or the decrease of its lattice parameter along the *c*- axis, with increasing temperature [68,80]. The observed discrepancy in the values of elastic anisotropy factors between the RUS measurements and DFT [71] are attributed to the difference in their C_{12} values.

For an anisotropic low symmetric crystal, Voight-Ruess-Hill (VRH) approximation is used to convert the anisotropic elastic constants to the macroscopic elastic moduli which represent the average (effective) elasticity of the crystalline material. the calculated elastic properties using VRH is tabulated in Table 7.3. The calculated values are then compared with the values deduced from DFT and pulse-echo techniques [71,72].

Table 7.3. Elastic properties of the orthorhombic SnSe derived from the Voigt-Reuss-Hill approximations, compared with the values obtained from DFT and Pulse-echo techniques.

Elastic Parameter	**Method**			
	RUS	DFT	% Diff:	Pulse-echo
Bulk Modulus $\boldsymbol{B}$	23.2	24.1	4	-
Shear modulus $\boldsymbol{G}$ (GPa)	16.0	15.2	5	9.6
Young's modulus $\boldsymbol{E}$ (GPa)	39.0	37.6	4	27.7
Poisson's ratio $\boldsymbol{\nu}$	0.22	0.24	9	0.44
B/G ratio	1.45	1.59	9	-
Longitudinal velocity $\boldsymbol{v_l}$ (m/s)	2717	2711	0.2	2730
Shear velocity $\boldsymbol{v_s}$ (m/s)	1629	1587	3	1250
Average velocity $\boldsymbol{v_m}$ (m/s)	1803	1759	2	1420
Debye Temperature $\Theta_{\boldsymbol{D}}$ (K)	178	174	2	142

The calculated elastic properties of SnSe using the measured elastic constants are in reasonable agreement with the DFT values to within 9%. The deviations in the elastic constants deduced from the RUS and the pulse-echo method, are attributed to differences in the experimental conditions such as the temperature and the density of the crystal. The data reported by pulse-echo technique are derived from the velocity measurements along *b*- axis, whereas the elastic constants of the anisotropic single crystalline SnSe were obtained from the RUS measurements are not specified by any particular direction. The ratio *B*/*G* for a polycrystalline phase is a measure of its fracture/toughness, where a high (low) *B*/*G* value is associated with ductility (brittleness). In general, if *B*/*G* > 1.75 the material is ductile, otherwise it is brittle (*B*/*G* <1.75) [81]. From the *B*/*G* values listed in Table 7.3, it can be inferred that the SnSe crystals used in this study are brittle. Furthermore, the Debye temperature, θ_D an important thermodynamic parameter (defined according to the Debye model as the maximum temperature acquired from a single mode of vibration) can be estimated from the average elastic wave velocity v_m obtained from our shear and bulk moduli using the relation $\theta_D = \frac{h}{k_B}\left[\frac{3qN\rho}{4\pi M}\right]^{1/3} v_m$ [11], which is in good agreement with the

value of θ_D obtained from DFT [71]. The comparatively low θ_D is a clear reflection of the low κ in SnSe.

7.3.2 Temperature Dependent Elasticity of SnSe

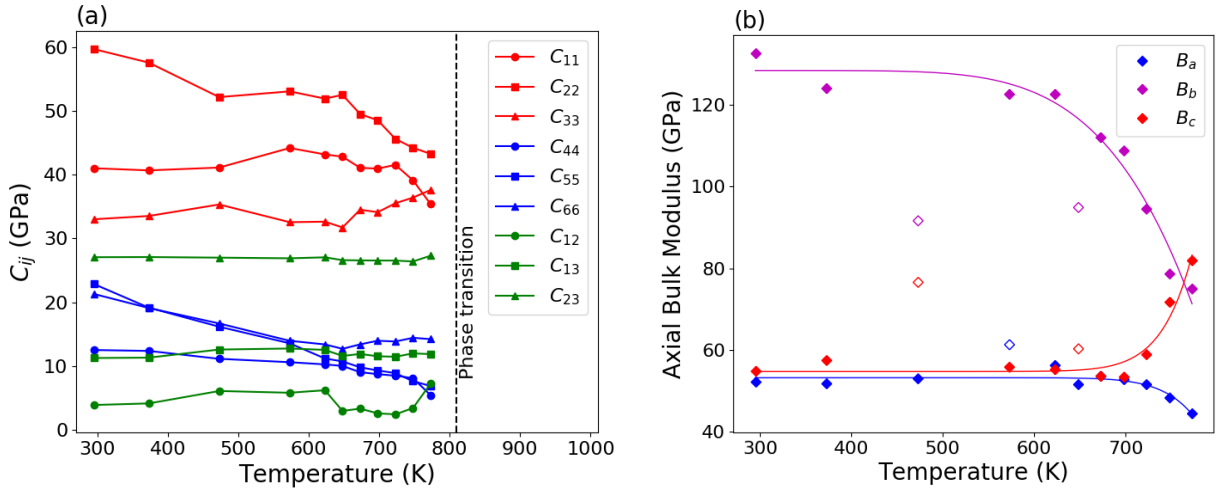

Figure 7.5. Temperature dependent (a) elastic constants and (b) axial bulk moduli in the temperature region of 295 – 797 K. Axial bulk moduli data were fitted with the empirical Varshni function [82] to elicit their temperature dependence. The outlier data points are shown by unfilled circles.

The variations of measured elastic constants with increasing temperature from 295 K to 797 K are illustrated in Figure 7.5(a). All the elastic constants except C_{33} show overall reduction with the increasing temperature, especially near the phase transition point. The elastic constants C_{44}, C_{55}, C_{66}, which represent the shear modes, exhibit a dramatic reduction down to ~30-55 % of their room temperature values. In Figure 7.5(b), the outlier axial bulk moduli (B_a, B_b, B_c) data are possibly due to the higher uncertainty in measuring weakly coupled off-diagonal elastic constants, e.g., C_{12}. The other off-diagonal elastic constants C_{23} and C_{13} exhibit a slight reduction by ~3% with increasing temperature. The extensional mode constants C_{11} and C_{22} except C_{33} have been reduced by 7-20 % of their room temperature values, indicating the softening of extensional modes

along *a*- and *b*- crystallographic directions. When compared to the variations of other elastic constants, C_{33} exhibits ~4% raise near the phase transition temperature, indicating the stiffening of the extensional mode along the *c*-direction. The observed deviation C_{33} from the other elastic constants is reflected by the calculated temperature-dependent axial bulk modulus data B_a, B_b, B_c along *a*-, *b*-, and *c*-direction respectively (Figure 7.5(b)) [83].

It is clear that the calculated bulk modulus along the *c*- direction, B_c increases near T_c, while B_a and B_b decrease with temperature. This variation of the axial bulk moduli illustrates the softening of the extensional modes along the *a*- and *b*- directions and stiffening along the *c*-direction as the temperature increases towards T_c. The above observations can be related to the change of the crystal structure and lattice constants between the room temperature *Pnma* phase to the high temperature *Cmcm* phase. At T_c, the weak Sn-Se bond along the *c*-direction in the *Pnma* phase (Figure 7.1) becomes stronger due to a reduction of the lattice constant from 4.439 Å to 4.293 Å. The bond reinforcement, which is observed as an increase of both C_{33} and B_c with increasing temperature, is indicative of a negative thermal expansion [68,73,80]. The decrease in both B_a and B_b are possibly due to the bond weakening governed by the thermal expansion and repulsive forces between Sn atoms, which are aligned in the *Cmcm* phase [69].

Figure 7.6(a) shows the change of the shear anisotropic factors A_1, A_2 and A_3 with increasing temperature. The anisotropic factor A_2, which corresponds to the *ac* plane reaches to 1 from 2.3 at 797 K, indicating an increasing elastic isotropy in the *ac* plane up to T_c. The observed change in isotropy is possibly due to the more symmetric bond arrangement in the *ac* plane of the *Cmcm* phase compared to that of *Pnma* phase. VRH calculated elastic moduli decrease with increasing temperature showing an overall material softening with increasing temperature before the phase transition point (Figure 7.6(b)).

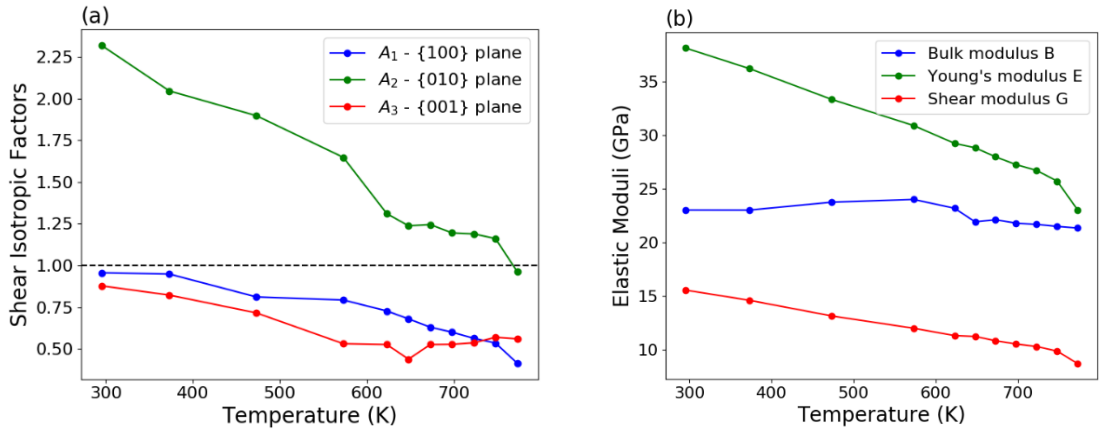

Figure 7.6. Temperature-dependent (a) shear anisotropic factors, (b) bulk modulus, Young's modulus and shear modulus. Dotted line in (a) indicates the shear isotropy factor =1.

It is well known that the average elastic moduli derived from the Voight Ruess Hill approximation, can be used to calculate the mean isotropic sound velocities in a sample as this method does not provide any information about the anisotropy of the wave velocities through single crystalline SnSe. Therefore, we use Christoffel equations for plane waves to calculate the longitudinal (v_l) and transverse (v_t) sound velocities using the measured temperature dependent elastic constants along the three major crystallographic directions [10]. The mean sound velocities (v_m) along each axis were calculated using the relation $\left[\frac{1}{v_m^3} = \frac{1}{3}\left(\frac{1}{v_l^3} + \frac{2}{v_t^3}\right)\right]$ (Figure 7.7(a)), and we estimate the phonon mean free path $\ell_{transport}$ (Figure 7.7(b)) using our previously reported temperature-dependent thermal transport measurements including heat capacity and thermal conductivity [69]. Based on the kinetic theory of gases $\ell_{transport} = 3\kappa_L/C_p v_m$, where κ_L is the lattice thermal conductivity and C_p is the measured specific heat per unit volume, and v_m is the mean velocity of sound through the SnSe crystal [7]. Figure 7.7(b) shows the $\ell_{transport}$ as a function of temperature, where the value of $\ell_{transport}$ along the a-direction is the lowest compared

to those along the *b*- and *c*-directions, consistent with the lowest κ_L along the *a*-direction [69]. Previously, we also reported temperature dependent Raman study of single crystalline SnSe. Bulk SnSe in the *Pnma* phase is known to exhibit twelve signature Raman-active optical phonon modes [70,84,85], among which four B_{2g} modes are difficult to detect due to their weak Raman tensors. Furthermore, two B_{1g} modes (~57 cm^{-1} and ~133 cm^{-1}) are only observable under the $c(ab)\bar{c}$ polarization configuration. Of the remaining six Raman-active phonons, the two lowest frequency phonons namely, A_g^0 ~33 cm^{-1} and B_{3g} ~37 cm^{-1} are difficult to resolve, owing to the increasing spectral background below 40 cm^{-1} at high temperatures. We focused on the four Raman-active phonons [86,87] between 70-150 cm^{-1} (Figure 7.7(c)), and using their measured linewidths, we calculate phonon lifetimes (τ_{Raman}) for each Raman mode [70]. The eigen vectors for individual Raman modes are shown in Figure 7.7(c), wherein the arrows point to the direction of vibration.

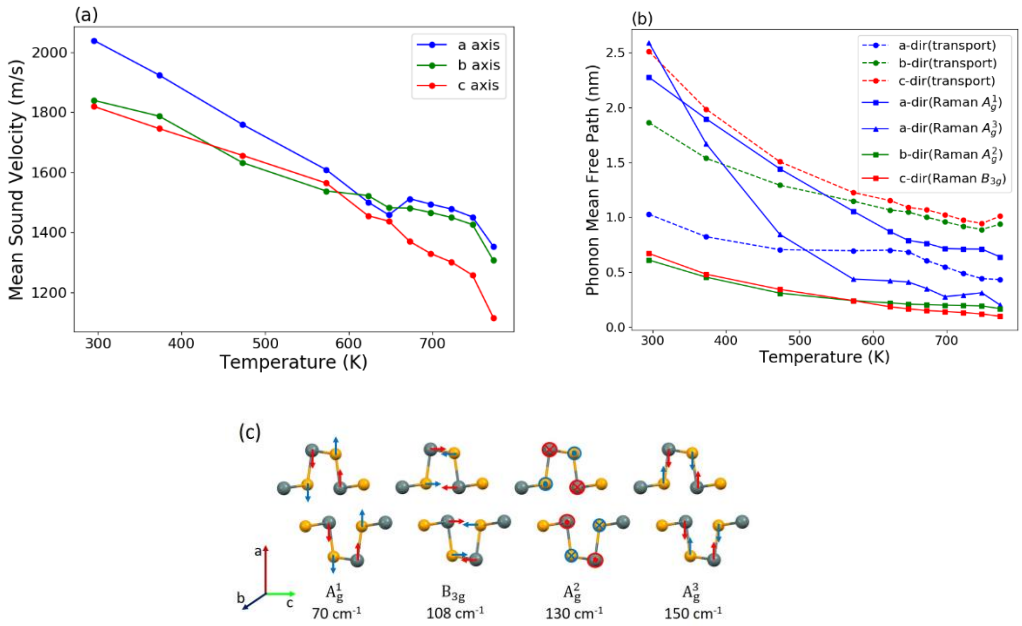

Figure 7.7. (a) the temperature dependence of the mean sound velocity along each *a*-, *b*- and *c*-crystallographic axis, (b) axial phonon mean free path calculated from thermal transport measurements and Raman studies and (c) schematics of the Raman modes.

Next, we calculated the phonon mean free path from Raman spectroscopic measurement in the temperature range (300-800K) where $\ell_{Raman} = v_m \times \tau_{Raman}$, was found to be the lowest for the B_{3g} and A_g^2 modes vibrating along the *b*- and *c*-directions respectively, indicating high phonon scattering along these directions. Depending on the direction in which the atoms vibrate for a given eigen mode (e.g., along *a* direction for A_g^1), the corresponding value of v_m along *a* direction was used to calculate ℓ_{Raman}. In the temperature range examined in this study, we find that $\ell_{transport} > \ell_{Raman}$ along the *b*- and *c*-directions, which is not the case along the *a*-direction. This discrepancy is attributed to the fact that the linewidths used in our calculations correspond to a specific Raman mode in which the motion of the atoms are directional, and phonon mean free path derived from thermal transport stems from a contribution from all phonon modes.

The Grüneisen parameter, γ provides a quantitative link between the thermal and mechanical parameters of solids [88]. When considering the thermodynamics and crystal structural change of SnSe, the Grüneisen parameter is often used to estimate the strength of the lattice anharmonicity as it is a direct measure of the relationship between the phonon frequency and crystal volume change [63,72]. Since the lattice thermal conductivity, κ_L is reduced by strong lattice anharmonicity, the Grüneisen parameter, γ is inversely proportional to κ_L according to the relation $\kappa_L \propto \gamma^{-2}$. In this study we used the relation $\gamma = \frac{9}{2}\left(\frac{v_l^2 - 4v_t^2/3}{v_l^2 + 2v_t^2}\right)$ to calculate the axial Grüneisen parameters γ_a, γ_b, γ_c along the-*a*-, *b*- and *c*- axes using the above measured axial wave velocities and their temperature dependence shown in Figure 7.8(a) [89]. The increase of all three Grüneisen parameters with increasing temperature suggests increasing lattice anharmonicity of SnSe up to T_c.

Furthermore, the temperature dependence of linear thermal expansion coefficients, α_i (TEC) along the major crystallographic directions were calculated using the relation, $\alpha_i = \frac{C_v}{V_0}\sum_k S_{ik}\gamma_k$ with $i,k = 1,2,3$, where we assume that $C_v \sim C_p$ except at T_c is the temperature dependent heat capacity and V_0 is the unit cell volume [73,90]. The linear and volumetric TECs are shown in Figure 7.8(b), where volumetric TEC, α_V can be obtained by $\alpha_V = \alpha_a + \alpha_b + \alpha_c$. The TECs along *a*- and *b*- directions are positive and increased with increasing temperature while the TEC along *c*- is negative in that temperature range, confirming the negative thermal expansion (NTE) along the *c*- direction. The calculated TEC and Grüneisen parameter along *c*- direction has confirmed the fact that the negative thermal expansion can be achieved even with positive Grüneisen parameters, which has been reported in previous theoretical studies [73,90]. Here the negativity of α_c is determined by the negative values of elastic compliance constants, S_{13} and S_{23}, indicating the crucial impact of the elasticity on the material's thermal expansion.

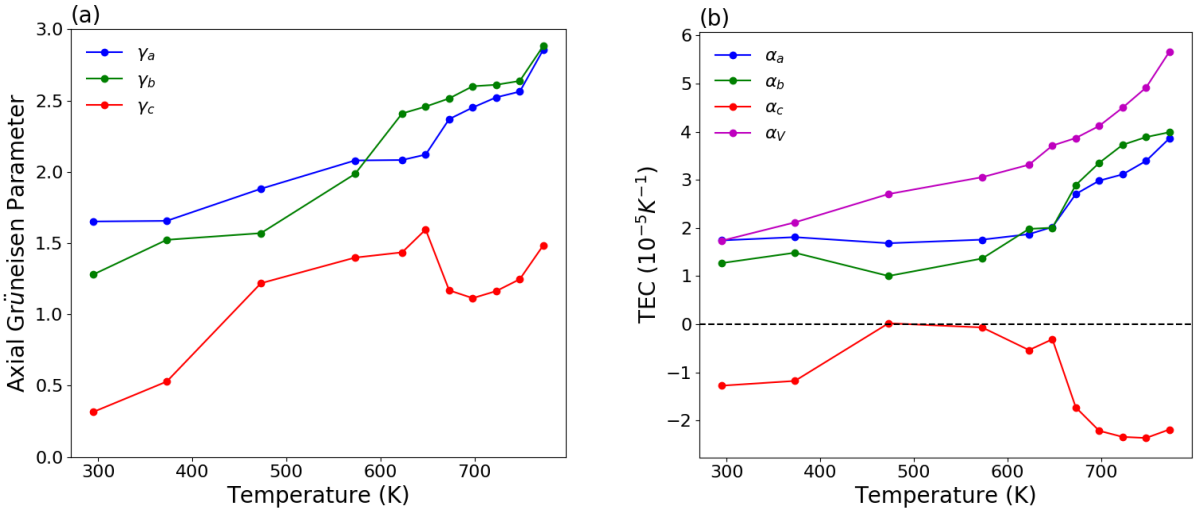

Figure 7.8. Temperature dependencies of the axial Grüneisen parameters $\gamma_a, \gamma_b, \gamma_c$ and (b) thermal expansion coefficients.

Figure 7.9 shows the normalized squares of mode frequencies, f^2 as a function of temperature. Although it is not feasible to compute the elastic constants with fewer number of resonance frequencies, the elasticity of material can be estimated by analyzing f^2 as they are proportional to the elastic constants [19,91]. The data in Figure 7 suggests a material softening up to 793 K, a rapid stiffening in 793 – 813 K region, and a slow softening after 813 K. The discontinuity of f^2 in the 793 – 813 K temperature range suggests a change of elasticity, which corresponds to the well-known structural phase transition of SnSe from disordered *Pnma* to ordered *Cmcm* phase.

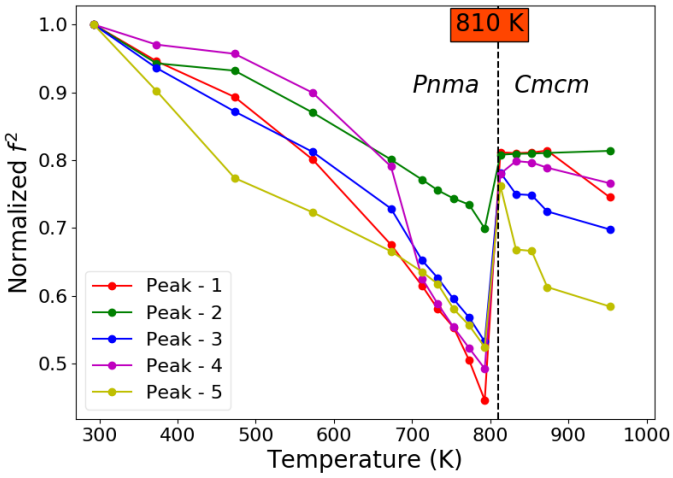

Figure 7.9. Variation of the normalized squares of selected natural frequencies of the sample (listed as Peak 1-5) as a function of temperature. (The mode numbers of peak 1-5 are estimated by matching the individual resonance peaks with the calculated resonance spectrum and they lie between the mode 3 and mode 70 in the frequency range of 215 – 685 kHz at room temperature).

7. 4 Conclusions

The nine independent elastic moduli of SnSe was measured using resonant ultrasound spectroscopy in the temperature range ~300-800 K. A complete description of computing anisotropic elastic moduli and polycrystalline elastic properties of low symmetric orthorhombic

crystal structure was presented using the room temperature elastic constants. The measured elastic moduli show a good agreement with theoretically reported values. The observed increase of the axial bulk modulus along c axis, B_c and the movement of shear anisotropic factor of ac plane, A_2 towards 1 with the increasing temperature, qualitatively demonstrated the bond reinforcement along the *c*- direction during the phase transition from the *Pnma* to *Cmcm* phases. using the measured elastic moduli, the temperature dependent velocity of sound and Grüneisen parameter were deduced along the major crystallographic directions. In addition, the phonon mean free paths as a function of temperature were derived from the temperature dependent thermal transport and Raman spectroscopy using the deduced velocity of sound that provided insight into the thermal transport mechanism and phonon anharmonicity of SnSe. Finally, the occurrence of the displacive phase transition of SnSe was detected at T_c ~803 +/- 10 K by the mean of the discontinuity of the temperature-dependent resonance frequency trend.

CHAPTER 8

CONCLUSIONS

The main goal of this dissertation was to explore the theory of poroelasticity by using the experimental studies of hydrostatic pressure and temperature dependent elasticity of selected porous ceramic materials. Lack of experimental studies to support the theory of poroelasticity and its behavior at different physical conditions was the key motivation to conduct this experimental work. Porous ceramics used in the solid oxide fuel cells, commercially available porous alumina, zircona, titania, and sintered fully dense zirconia were used in this study.

LG porous ceramics exhibited a high degree of vibrational damping due to the energy loss mechanisms introduced by the liquids trapped in pores during the sample preparation procedure. A heat-vacuum treatment was used to eliminate the trapped fluid phases and it caused to a significant enhancement of the signal strength of the resonance peaks in the resonance spectrum. This observation implies that acoustic attenuation can be achieved by the presence of fluid phases inside the pores. Acoustic metamaterials which are studied as sound insulation materials, use this phenomenon to enhance their sound insulation quality. The observed overall material stiffness over time at the equilibrium of high temperature (~ 500 K) and low hydrostatic pressure (~ 23 Torr) has been analyzed as a two-step process induced by gas removal and microcrack healing. The fitted time constants provide a quantitative measure of the rates of the stiffening mechanisms. The material stiffening due to gas removal was a quick process with lower time constant whereas microcrack healing process has taken longer time to make the material stiffer. The thermal cycling

study has shown a hysteretic behavior of material stiffening with heating and softening with cooling. As the temperature of the material rises, the microcracks in the material can be healed together reducing the porosity while the microcrack growth is occurred at cooling process leading to an increase of the porosity. The change in porosity determines the elasticity change of the porous materials. The hydrostatic pressure dependent elasticity data exhibited a material stiffening with reducing pressure confirming the above observation of quick material stiffening with lower time constant.

As described in Chapter 5, a series of experiments were conducted to investigate the hydrostatic pressure dependent elasticity of selected porous ceramic materials: alumina, zircona and titania. Pressure dependent normal mode frequencies and corresponding elastic moduli obtained at both low- and high- hydrostatic pressure regimes have confirmed that the porous ceramics exhibited a reversible material softening behavior with increasing hydrostatic pressure. The results were confirmed with the comparison of frequency trends of fully dense ceramics: zirconia and LG, who showed a slight stiffening with increasing pressure, as expected for typical solid materials. The comparison of the pressure dependent elasticity of porous and fully dense ceramics suggests that the porous material softening (stiffening) with increased (reduced) hydrostatic pressure is possibly due to the pore structure saturated with fluid and the reversible micromechanical movement of the structure (microcrack healing and growing) induced by applied pressure change. The computed elastic constant C_{11} and Young's modulus which correspond to the extensional modes have shown a rapid decrease with the increasing pressure while the shear mode C_{44} has followed a slow decrease. This suggests that the applied hydrostatic pressure provides a large impact on the extensional vibrational modes than the shear modes indicating that the extensional elastic constants are changed significantly with the change of hydrostatic pressure.

This observation has been explained by the Biot's theory of poroelasticity. The rate of material softening (/stiffening) with pressure (slope of frequency Vs pressure plot) was then analyzed with the saturation gas types. An increase of the softening slopes was observed with the gas saturation in the order of helium, nitrogen and argon such that helium saturation led to a slow softening while argon saturation exhibited a rapid softening. The softening rates were analyzed with the molecular weights of the gases and it was confirmed a linear relationship between slope and molecular weight to the power of one fourth such that $\left|\frac{\Delta f}{\Delta p}\right| \propto M^{1/4}$.

The experimental finding of partial sintering process exhibited by porous alumina at moderately high temperatures was discussed in Chapter 6. The rate of sintering process is mainly determined by the temperature and the exposed time to the temperature. In this study a slight change of porosity reduction (~0.08 %) was observed after 70 hours of exposer to 423 K. This suggests that the sintering process occurs even at the temperatures less than the standard sintering temperatures, but it requires a long exposer time.

This dissertation has successfully achieved its main goal of experimental studies on hydrostatic pressure and temperature dependent elasticity of porous ceramics. These experimental findings will lead to future research works in poroelasticity. Possible future studies are listed below.

1. Modify the RUS computation to determine the 7×7 elastic tensor to evaluate the poroelastic constants proposed in Biot's theory. In this way future research can be conducted to study the dependency of those poroelastic constants on hydrostatic pressure, temperature and porosity.

2. Repeat the experiments with a series of porous materials of varying porosity to investigate the porosity dependence of the elasticity variation with hydrostatic pressure.

3. Use the pressure dependent acoustic attenuation results to model and fabricate acoustic metamaterials which can be used as sound and vibration insulating materials.

The secondary goal of this dissertation was to explore the temperature dependent elastic properties of thermoelectric SnSe. Experimental determination of the elastic tensor for a low symmetric crystal was achieved successfully by RUS measurements. The measured nine elastic constants show a good agreement with the values obtained from the theoretical studies. A complete description of computing anisotropic elastic moduli and polycrystalline elastic properties of low symmetric orthorhombic crystal structure was presented using the room temperature elastic constants. The elastic constants measured in the temperature range of 295 – 797 K were then used to study the crystal structural change associated with the phase transition. In addition, the phonon mean free paths as a function of temperature were derived from the temperature dependent thermal transport and Raman spectroscopy using the deduced velocity of sound that provided insight into the thermal transport mechanism and phonon anharmonicity of SnSe.

References

[1] T. D. Ngo, A. Kashani, G. Imbalzano, K. T. Q. Nguyen, and D. Hui, Compos. Part B Eng. **143**, 172 (2018).

[2] H. Dommati, S. S. Ray, J.-C. Wang, and S.-S. Chen, RSC Adv. **9**, 16869 (2019).

[3] J. Jeevanandam, A. Barhoum, Y. S. Chan, A. Dufresne, and M. K. Danquah, Beilstein J. Nanotechnol. **9**, 1050 (2018).

[4] A. E. H. Love, xviii (1927).

[5] I. S. Sokolnikoff, B. University., and G. School., *Mathematical Theory of Elasticity*, (Providence, R.I, 1941).

[6] S. Timoshenko and J. N. Goodier, (1969).

[7] C. Kittel, xi (1996).

[8] W. Rehwald, Adv. Phys. **22**, 721 (1973).

[9] P. Ravindran, L. Fast, P. A. Korzhavyi, B. Johansson, J. Wills, and O. Eriksson, J. Appl. Phys. **84**, 4891 (1998).

[10] H. Ledbetter and A. Migliori, J. Appl. Phys. **100**, 63515 (2006).

[11] O. L. Anderson, J. Phys. Chem. Solids **24**, 909 (1963).

[12] W. Zhang, C. Chai, Y. Song, Q. Fan, and Y. Yang, Mater. **11**, 740 (2018).

[13] M. F. Markham, Br. J. Appl. Phys. **8**, S56 (1957).

[14] Y. B. Saddeek, Mater. Chem. Phys. **91**, 146 (2005).

[15] A. Migliori, J. L. Sarrao, W. M. Visscher, T. M. Bell, M. Lei, Z. Fisk, and R. G. Leisure, Phys. B Condens. Matter **183**, 1 (1993).

[16] J. Maynard, Phys. Today **49**, 26 (1996).

[17] A. Migliori and J. L. Sarrao, xii (1997).

[18] A. Migliori and J. D. Maynard, Rev. Sci. Instrum. **76**, 121301 (2005).

[19] H. H. Demarest, J. Acoust. Soc. Am. **49**, 768 (1971).

[20] W. M. Visscher, W. M. Visscher, A. Migliori, A. Mialiori, T. M. Bell, T. M. Bell, R. A. Reinert, and R. A. Reinert, J. Acoust. Soc. Am. **90**, 2154 (1991).

[21] G. Li and J. R. Gladden, Int. J. Spectrosc. **2010**, 1 (2010).

[22] M. E. Davis, Nature **417**, 813 (2002).

[23] J. Y. Ying, C. P. Mehnert, and M. S. Wong, Angew. Chemie Int. Ed. **38**, 56 (2004).

[24] J. Lee, S. Yoon, T. Hyeon, S. M. Oh, and K. Bum Kim, Chem. Commun. 2177 (1999).

[25] Z. Živcová, E. Gregorová, W. Pabst, D. S. Smith, A. Michot, and C. Poulier, J. Eur. Ceram. Soc. **29**, 347 (2009).

[26] J. Liu, Y. Li, Y. Li, S. Li, and S. Sang, Ceram. Int. **42**, 8221 (2016).

[27] T. Kuwahara, K. Yoshida, K. Hanamoto, K. Sato, T. Kuroki, T. Yamamoto, and M. Okubo, IEEE Trans. Ind. Appl. **48**, 1649 (2012).

[28] R. Naslain, A. Guette, F. Rebillat, R. Pailler, F. Langlais, and X. Bourrat, J. Solid State Chem. **177**, 449 (2004).

[29] P. Göransson and KTH, Philos. Trans. R. Soc. A Math. Phys. Eng. Sci. **364**, 89 (2006).

[30] M. K. Kuczmarski and J. C. Johnston, **2011-216995.;216995.;**, (2011).

[31] M. A. Lewińska, V. G. Kouznetsova, J. A. W. van Dommelen, and M. G. D. Geers, Eur. J. Mech. - A/Solids **77**, 103805 (2019).

[32] M. A. Lewińska, J. A. W. van Dommelen, V. G. Kouznetsova, and M. G. D. Geers, J. Mech. Phys. Solids **124**, 189 (2019).

[33] W. Lu, D. Yuan, D. Zhao, C. I. Schilling, O. Plietzsch, T. Muller, S. Bräse, J. Guenther, J. Blümel, R. Krishna, Z. Li, and H.-C. Zhou, Chem. Mater. **22**, 5964 (2010).

[34] E. Traversa, Sensors Actuators B. Chem. **23**, 135 (1995).

[35] E. Dickey, O. Varghese, K. Ong, D. Gong, M. Paulose, and C. Grimes, Sensors **2**, 91 (2002).

[36] A. Heinzel and B. C. H. Steele, Nat. **414**, 345 (2001).

[37] J. J. Haslam, A. Pham, B. W. Chung, J. F. DiCarlo, R. S. Glass, and L. Lawrence Livermore National Lab. CA (US), J. Am. Ceram. Soc. **88**, 513 (n.d.).

[38] M. A. Biot, J. Appl. Phys. **26**, 182 (1955).

[39] M. A. Biot, J. Appl. Mech. **78**, 91 (1956).

[40] M. A. Biot, J. Appl. Mech. **24**, 594 (1957).

[41] M. A. Biot, J. Appl. Phys. **33**, 1482 (1962).

[42] H. Wang, (2000).

[43] C. Tao and X. Liu, J. Acoust. Soc. Am. **129**, 934 (2011).

[44] A. P. Roberts and E. J. Garboczi, J. Am. Ceram. Soc. **83**, 3041 (2000).

[45] K. Miled, K. Sab, and R. Le Roy, Mech. Res. Commun. **38**, 131 (2011).

[46] G. Y. Gor, D. W. Siderius, V. K. Shen, and N. Bernstein, J. Chem. Phys. **145**, 164505 (2016).

[47] R. G. Munro, J. Res. Natl. Inst. Stand. Technol. **109**, 497 (2004).

[48] X. Zhang, W. Li, H. Kou, J. Shao, Y. Deng, and J. Ma, Mater. Res. Express **5**, 15204 (2018).

[49] P. Auerkari, *Mechanical and Physical Properties of Engineering Alumina Ceramics* (1996).

[50] F. Ren, E. D. Case, A. Morrison, M. Tafesse, and M. J. Baumann, Philos. Mag. **89**, 1163 (2009).

[51] W. Pabst, E. Gregorová, and M. Černý, J. Eur. Ceram. Soc. **33**, 3085 (2013).

[52] L. Pimienta, J. Sarout, L. Esteban, C. David, and M. B. Clennell, J. Geophys. Res. Solid Earth **122**, 8952 (2017).

[53] D. H. Chung and G. Simmons, J. Appl. Phys. **39**, 5316 (1968).

[54] X. Fan, E. D. Case, F. Ren, Y. Shu, and M. J. Baumann, J. Mech. Behav. Biomed. Mater. **8**, 21 (2012).

[55] J. E. Ni, F. Ren, E. D. Case, and E. J. Timm, Mater. Chem. Phys. **118**, 459 (2009).

[56] G. S. Nolas, J. Sharp, and H. J. Goldsmid, **45.**, (2001).

[57] C. Wood, Reports Prog. Phys. **51**, 459 (1988).

[58] D. M. Rowe, (1995).

[59] G. J. Snyder and E. S. Toberer, Nat. Mater. **7**, 105 (2008).

[60] A. J. Minnich, M. S. Dresselhaus, Z. F. Ren, and G. Chen, Energy Environ. Sci. **2**, 466 (2009).

[61] B. Poudel, Q. Hao, Y. Ma, Y. Lan, A. Minnich, B. Yu, X. Yan, D. Wang, A. Muto, D. Vashaee, X. Chen, J. Liu, M. S. Dresselhaus, G. Chen, and Z. Ren, Sci. **320**, 634 (2008).

[62] X. W. Wang, H. Lee, Y. C. Lan, G. H. Zhu, G. Joshi, D. Z. Wang, J. Yang, A. J. Muto, M. Y. Tang, J. Klatsky, S. Song, M. S. Dresselhaus, G. Chen, and Z. F. Ren, Appl. Phys. Lett. **93**, 193121 (2008).

[63] L.-D. Zhao, S.-H. Lo, Y. Zhang, H. Sun, G. Tan, C. Uher, C. Wolverton, V. P. Dravid, and M. G. Kanatzidis, Nature **508**, 373 (2014).

[64] C. W. Li, J. Hong, A. F. May, D. Bansal, S. Chi, T. Hong, G. Ehlers, and O. Delaire, Nat. Phys. **11**, 1063 (2015).

[65] J. P. Heremans, Nat. Phys. **11**, 990 (2015).

[66] A. Okazaki and I. Ueda, J. Phys. Soc. Japan **11**, 470 (1956).

[67] M. Sist, J. Zhang, and B. Brummerstedt Iversen, Acta Crystallogr. Sect. B **72**, 310 (2016).

[68] T. Chattopadhyay, J. Pannetier, and H. G. Von Schnering, J. Phys. Chem. Solids **47**, 879 (1986).

[69] P.-C. Wei, S. Bhattacharya, Y.-F. Liu, F. Liu, J. He, Y.-H. Tung, C.-C. Yang, C.-R. Hsing,

D.-L. Nguyen, C.-M. Wei, M.-Y. Chou, Y.-C. Lai, T.-L. Hung, S.-Y. Guan, C.-S. Chang, H.-J. Wu, C.-H. Lee, W.-H. Li, R. P. Hermann, Y.-Y. Chen, and A. M. Rao, ACS Omega **4**, 5442 (2019).

[70] F. Liu, P. Parajuli, R. Rao, P. C. Wei, A. Karunarathne, S. Bhattacharya, R. Podila, J. He, B. Maruyama, G. Priyadarshan, J. R. Gladden, Y. Y. Chen, and A. M. Rao, Phys. Rev. B **98**, 224309 (2018).

[71] G. Li, U. Aydemir, M. Wood, W. A. Goddard, P. Zhai, Q. Zhang, and G. J. Snyder, Chem. Mater. **29**, 2382 (2017).

[72] Y. Xiao, C. Chang, Y. Pei, D. Wu, K. Peng, X. Zhou, S. Gong, J. He, Y. Zhang, Z. Zeng, and L.-D. Zhao, Phys. Rev. B **94**, 125203 (2016).

[73] G. Liu, J. Zhou, and H. Wang, Phys. Chem. Chem. Phys. **19**, 15187 (2017).

[74] A. Shyam, E. Lara-Curzio, A. Pandey, T. R. Watkins, and K. L. More, J. Am. Ceram. Soc. **95**, 1682 (2012).

[75] D. G. Isaak, J. D. Carnes, O. L. Anderson, and H. Oda, J. Acoust. Soc. Am. **104**, 2200 (1998).

[76] Y. Hirata, A. Hara, and I. A. Aksay, Ceram. Int. **35**, 2667 (2009).

[77] R. W. Rice, *Porosity of Ceramics: Properties and Applications* (Taylor & Francis, 1998).

[78] A. S. Wagh, R. B. Poeppel, and J. P. Singh, J. Mater. Sci. **26**, 3862 (1991).

[79] I. Loa, R. J. Husband, R. A. Downie, S. R. Popuri, and J.-W. G. Bos, (2014).

[80] D. Bansal, J. Hong, C. W. Li, A. F. May, W. Porter, M. Y. Hu, D. L. Abernathy, and O. Delaire, Phys. Rev. B **94**, (2016).

[81] S. F. Pugh, Philos. Mag. **45**, 823− 843 (1954).

[82] Y. P. Varshni, Phys. Rev. B **2**, 3952 (1970).

[83] A. Karunarathne, J. R. Gladden, G. Priyadarshan, P.-C. Wei, T.-L. Hung, P. Parajuli, S. Bhattacharya, Y.-Y. Chen, and A. M. Rao, ACS Appl. Energy Mater. (2018).

[84] H. R. Chandrasekhar, R. G. Humphreys, U. Zwick, and M. Cardona, Phys. Rev. B **15**, 2177 (1977).

[85] J. M. Skelton, L. A. Burton, S. C. Parker, A. Walsh, C.-E. Kim, A. Soon, J. Buckeridge, A. A. Sokol, C. R. A. Catlow, A. Togo, and I. Tanaka, Phys. Rev. Lett. **117**, 75502 (2016).

[86] J. Hong and O. Delaire, 1 (2016).

[87] X. Xu, Q. Song, H. Wang, P. Li, K. Zhang, Y. Wang, K. Yuan, Z. Yang, Y. Ye, and L. Dai, ACS Appl. Mater. Interfaces **9**, 12601 (2017).

[88] F. D. Stacey and J. H. Hodgkinson, Phys. Earth Planet. Inter. **286**, 42 (2019).

[89] D. Wang and G. Wang, Phys. Lett. A **381**, 801 (2017).

[90] E. T. Ritz and N. A. Benedek, Phys. Rev. Lett. **121**, 255901 (2018).

[91] S. Bhattacharya, D. C. Marinescu, J. R. Morris, I. A. Sergienko, B. Sales, D. Mandrus, and V. Keppens, Phys. Rev. B **86**, 24402 (2012).

Appendix

PYTHON PROGRAM FOR LORENTZIAN LINE SHAPE CURVE FITTING

This python script was created to analyze the center frequency and the quality factor of each resonance peaks by using the Lorentzian line shape curve fitting. The Lorentzian function is given by,

$$y = \frac{A\left(\frac{f}{f_0 \cos(\phi)} + \left(1 - \left(\frac{f}{f_0}\right)^2\right) Q \sin(\phi)\right)}{\left(\frac{f}{f_0}\right)^2 + \left(1 - \left(\frac{f}{f_0}\right)^2\right)^2 Q^2} + y_0$$

Where, the background function y_0 is defined as,

$$y_0 = a_0 + a_1(f - f_0) + a_2(f - f_0)^2 + a_3(f - f_0)^3$$

Where, the fit parameters are defined as follows,

f_0 = Center or resonance frequency

Q = Quality factor

ϕ = Phase shift

a_i = Coefficients of polynomial background function

RUS instruments are designed to record the material response for the corresponding driving frequencies. These material responses are measured as in-phase and quadrature voltage amplitudes and they are saved in a data file. The first step of this program is to import the data file and plot the quadrature signal with the driving frequency. The next step is to select a resonance peak to perform the curve fitting. This program use mouse click operations to select the resonance peak. User is asked to make the first right click on the left edge of the peak to acquire f_{min} and the second

right click on the right edge of the peak to acquire f_{max}. Here only right click options are used to avoid the misguidance with the zoom-in and zoom-out options as python plots use left clicks for the zoom process. Selected peak is then plotted by slicing the original data from f_{min} to f_{max}. After that, the program asks user to mark the center position of the resonance peak by using a left click and then press enter to perform the curve fitting. In this process program acquires the marked center frequency and use it to calculate the initial conditions for the fit parameter

The initial conditions of fit parameters will be determined as follows.

f_{0i} = Center frequency marked by the left click operation

$A_i = y_{max} - y_{min}$

$Q_i = 5 \times \left(\frac{f_{0i}}{f_{max} - f_{min}}\right)$

$\phi = 0.1$

When user press ‘enter’ key, the program performs the curve fitting and plot the fitted data with the original data. The flowchart of the fitting routine is shown in Figure A.1. At the same time, program creates a text file named as ‘fit data.txt’, inside the same directory and append the fit parameters of center frequency (in MHz) and Q factor. This text file will be updated at each fitting process. In some reason user may select peaks randomly which leads to update the ‘fit data.txt’ text file with disordered frequency list. In RUS, the order of the normal modes is very important to fit the elastic constants. Therefore, this program then sorts the frequency data saved in ‘fit data.txt’ text and save inside a newly created text file called ‘sorted data.txt’.

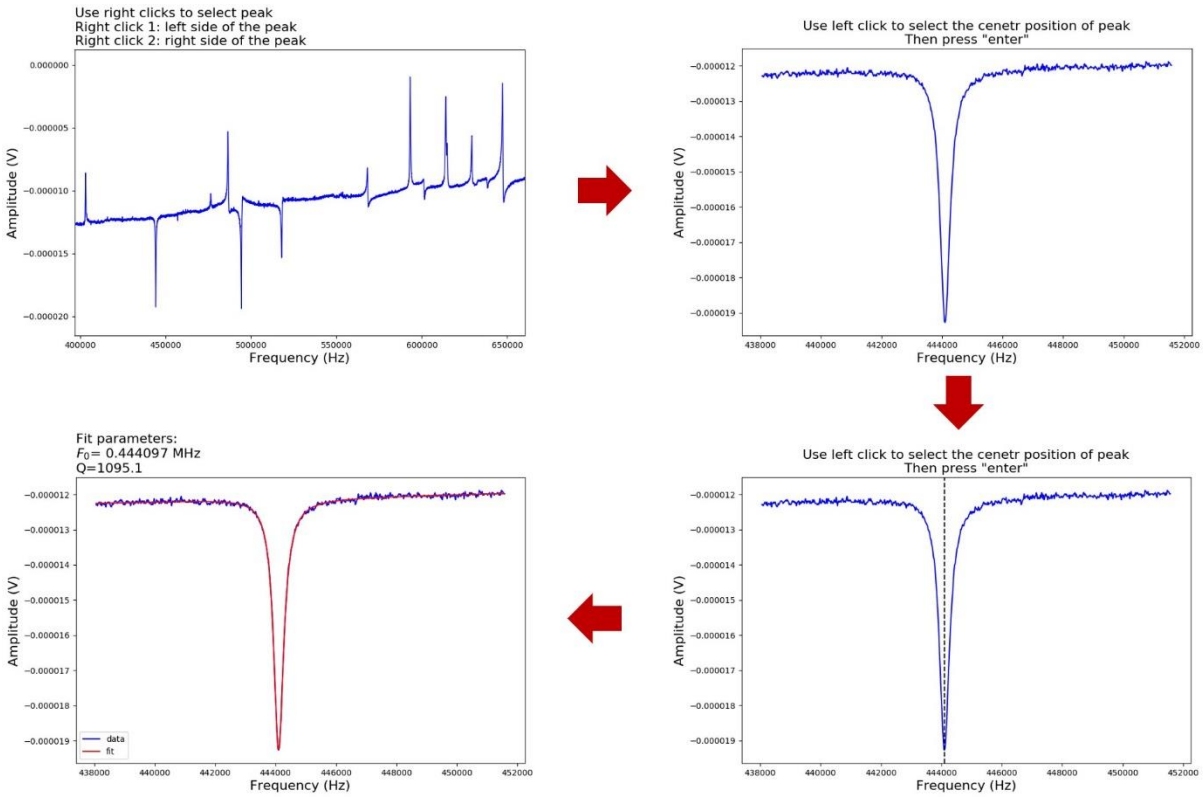

Figure A.1. The flowchart of the Lorentzian line shape curve fitting

Python script starts from here.

```
Lorentzian line shape curve fitting
##########################################################################################
import numpy as np
import matplotlib.pyplot as pl
from scipy.optimize import curve_fit
import os

## Change the directory where the input data file stored
os.chdir('file name')

## Load the data file
data=np.loadtxt('snse.dat')    ## put the name of the file
x=data[:,0]      ## Driving frequency list
y=data[:,2]      ## Quadrature signal amplitude
pl.close('all')
pl.plot(x,y,'b',linewidth=1)
pl.title('Lorentzian line shape curve fitting',fontsize=15)
pl.title('Use right clicks to select peak'
'\nRight click 1: left side of the peak\n'
```

```
'Right click 2: right side of the peak',loc='left')
pl.xlabel('frequency (Hz)',fontsize=12)
pl.ylabel('Amplitude (V)',fontsize=12)
pl.show()
figManager = pl.get_current_fig_manager()
figManager.window.showMaximized()

def lorentzian(x,x0,A,Q,phi):
   ''' lorentzian line shape function'''
   y1=A*(x/x0*np.cos(phi)+(1.0-(x/x0)**2)*Q*np.sin (phi)) /((x/x0)**2+
   (1.0-(x/x0)**2)**2*Q**2)
   return y1

def background(x,x0,a0,a1,a2,a3):
   '''background function'''
   y2=a0+a1*(x-x0)+a2*(x-x0)**2+a3*(x-x0)**3
   return y2

def f(x,x0,A,Q,phi,a0,a1,a2,a3):
   '''fit function: lorentzian+background'''
   Y=lorentzian(x,x0,A,Q,phi)+background(x,x0,a0,a1,a2,a3)
   return Y

xlim=[]

## Peak selection
## use two right clicks to select the peak
def click(event):
   if event.button == 3:
      x1=event.xdata
      pl.axvline(x=x1,linestyle='--',color='k')
      pl.draw()
      xlim.append(x1)
      xmin=len(x[x<xlim[0]])
      xmax=len(x[x<xlim[1]])
      x1=x[xmin:xmax]
      y1=y[xmin:xmax]

      ## plot the selected peak
      pl.close('all')
      pl.plot(x1,y1,'b')
      pl.xlabel('frequency (Hz)',fontsize=12)
      pl.ylabel('Amplitude (V)',fontsize=12)
      pl.title('Use left click to select the cenetr position of peak\n'
```

```
'Then press "enter"')
pl.show()
figManager = pl.get_current_fig_manager()
figManager.window.showMaximized()

## use the left click to mark the center of the peak
def click1(event1):
    if event1.button ==1:
        x0,y0=event1.xdata,event1.ydata
        pl.axvline(x=x0,linestyle='--',color='k')
        pl.draw()

    ## to start the curve fitting process
    def keypress(event2):
        if event2.key == 'enter':
            ## Initial parameters
            par0=[x0,(max(y1)-min(y1)),(5*x0/(max(x1)-min(x1))),0.1,
            y1[0],-1e-7,1e-14,1e-16]

            ## Curve fitting
            fit=curve_fit(f,x1,y1,p0=par0)

            ## Fit parameters
            fx0=fit[0][0]
            fA=fit[0][1]
            fQ=fit[0][2]
            fphi=fit[0][3]
            fa0=fit[0][4]
            fa1=fit[0][5]
            fa2=fit[0][6]
            fa3=fit[0][7]

            pl.close('all')
            xfit=np.linspace(min(x1),max(x1),10000)
            yfit=f(xfit,fx0,fA,fQ,fphi,fa0,fa1,fa2,fa3)
            pl.plot(x1,y1,'b',label='data')
            pl.plot(xfit,yfit,'r',label='fit')
            pl.xlabel('frequency (Hz)',fontsize=12)
            pl.ylabel('Amplitude (V)',fontsize=12)
            pl.title('Lorentzian line shape curve fit',fontsize=16)
            pl.title('Fit parameters:\n'
            '$F_{0}$= %1.6f MHz\nQ=%3.1f'%(fx0/1e6,fQ), loc='left')
            pl.legend()
            pl.show()
```

```
            figManager = pl.get_current_fig_manager()
            figManager.window.showMaximized()

            ## save the data in a text file
            F=open('fitdata.txt','a+')
            F.write('%1.6f\t%3.1f\n'%(fx0/1e6,fQ))

            ## To sort the frequency data according to ascending order
            F = open('fitdata.txt', "r")
            lines = F.readlines()
            F.close()
            lines.sort()
            f1 = open('sorted data.txt' , "w")
            for line in lines:
               f1.write(line)
            f1.flush()
            f1.close()

        pl.connect('key_press_event',keypress)
   pl.connect('button_press_event',click1)
pl.connect('button_press_event',click)

##############################################################################
```

End of the script.

VITA

Ashoka Karunarathne was born in Kandy, Sri Lanka in 1990. Ashoka earned his Bachelor of Science degree in physics from University of Peradeniya, Sri Lanka in January 2015. Soon after completion of B.Sc. degree, he started his postgraduate education upon receiving a generous graduate assistantship from the University of Mississippi in August 2015. He served to the Department of Physics and Astronomy as a teaching assistant from August 2015 to December 2019 and there he was fortunate to gain tremendous teaching experience. In January 2016, he joined the material science research group at the National Center for Physical Acoustics (NCPA) as a research assistant under the supervision of Dr. Josh Gladden. Ashoka started his dissertation project based on Resonant Ultrasound Spectroscopic studies of elasticity of porous ceramics and thermoelectric SnSe. Ashoka has published several publications: 'Room Temperature Resonant Ultrasound Spectroscopy of Single Crystalline SnSe (*ACS Appl. Energy Mater.*)', 'Low Pressure Dependent Elasticity of Porous Ceramics (*J. Am. Ceram. Soc.*)' and 'Phonon Anharmonicity in Single-Crystalline SnSe (*Phys. Rev. B*)', proving the success of his dissertation work. Also he gave reserch presentations in several conferences: Acoustical Society of America (2017, 2019), The Minerals, Metals and Materials Society (2018), The Materials Science & Technology (2019). He was awarded the third place in the poster competition organiced by Mississippi INBRE Graduate Scholars Symposium (2018). During his time at the University of Mississippi, Ashoka was an active member of Physics Graduate Student Association (PGSA) and he took several leadership roles as the vice president (2017) and the journal club coordinator (2019).